HERA: PHYSICS, MACHINE AND EXPERIMENTS

by

G. Wolf

Deutsches Elektronen-Synchrotron DESY, Hamburg

HERA: PHYSICS, MACHINE AND EXPERIMENTS*

Günter Wolf

Deutsches Elektronen-Synchrotron, DESY,

Hamburg, Germany

ABSTRACT

With HERA ep collisions at a c.m. energy of 314 GeV and $Q^2_{max} = 10^5$ GeV^2 will become possible. The physics opportunities, the design and status of the machine and the planned detectors are discussed.

---

* Lectures given at the Advanced Study Institute on Techniques and Concepts of High Energy Physics, 1986, St. Croix, Virgin Islands

INTRODUCTION

DESY is presently constructing a new storage ring HERA that will provide collisions between 30 GeV electrons and 820 GeV protons[1]. Experimentation is scheduled to begin in 1990.

HERA offers exciting and unique physics opportunities. Electrons and quarks can be probed for substructure down to distances of a few 10^{-18} cm. A search for new mediators of the neutral and charged current is possible up to W' and Z' masses of 800 GeV. The large center of mass energy permits the detection of leptoquarks up to 180 GeV, of families of excited quarks and leptons up to 250 GeV, and squarks and sleptons can be produced with masses up to 180 GeV - provided they exist.

The following lectures present an introduction to the physics expected at HERA and describe briefly the machine and the planned experiments.

2.   HERA PHYSICS: GENERAL CONDITIONS

The large momentum transfers possible between electron and proton, $Q^2_{max} = 10^5$ GeV^2, make HERA first and foremost an electron quark collider. The relevant diagram is shown in Fig. 1. The incoming electron emits a

lepton ℓ and exchanges a current j with one of the quarks of the incoming proton. This leads to the emission of a quark q' called the current quark. Depending on whether a neutral current (γ, Z^0) or a charged current (W^-) is exchanged the final state lepton is either an electron or a neutrino (Fig. 2).

The scattering process is not confined to the known currents, quarks and leptons. New currents may contribute and new quarks and leptons with masses up to the kinematic limit of 314 GeV may be produced. Any particle with electromagnetic and/or weak charge which is within the kinematic limits can be produced.

Next to electron quark scattering, current-gluon fusion (see Fig.3) will play an important role at HERA. Photon-gluon fusion depicted in Fig.4 will presumably be the dominant process for the production of heavy quarks $Q = c,b,t...$.

We shall discuss a few reactions that are archetypical for the different types of processes. More detailed studies can be found in Refs. 2,3.

3. ELECTRON SCATTERING AND THE PROTON STRUCTURE FUNCTIONS.

3.1 Kinematics

The diagram that describes ep scattering in lowest order is shown in Fig. 1 (taking $j = \gamma$). The event topology is illustrated in Fig. 5. The final state partons (quarks, gluons) and the "spectator" remnants from the incident proton are assumed to develop into jets of hadrons. The lepton and the current jet emerge on opposite sides of the beam axis, balancing each other in transverse momentum. The debris of the proton is emitted in a very narrow cone (of order 10 mrad) around the proton beam direction.

Apart from the total center-of-mass energy squared,

$$s = (p_p + p_e)^2 = m_e^2 + m_p^2 + 2(E_e E_p + p_e p_p) \approx 4E_e E_p$$

E_e, E_p energies of incoming electron and proton
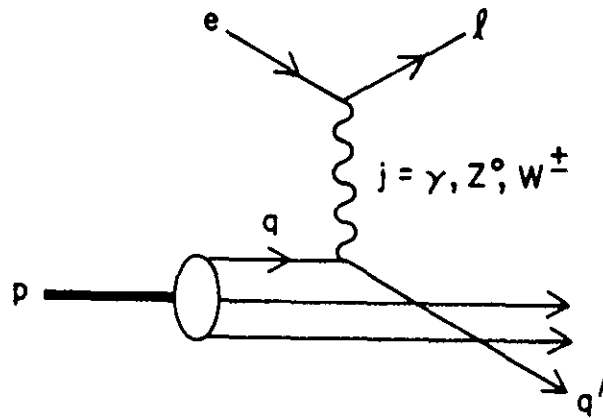
39795

Fig. 1 Lepton proton scattering.

a)   b)

Fig. 2 Diagrams for neutral (a) and charged current (b) scattering.

Fig. 3 Quark pair production by
current gluon fusion.
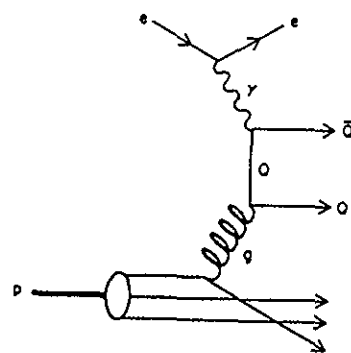
Fig. 4 Quark pair production by
photon gluon fusion.

BEFORE

e   p

AFTER
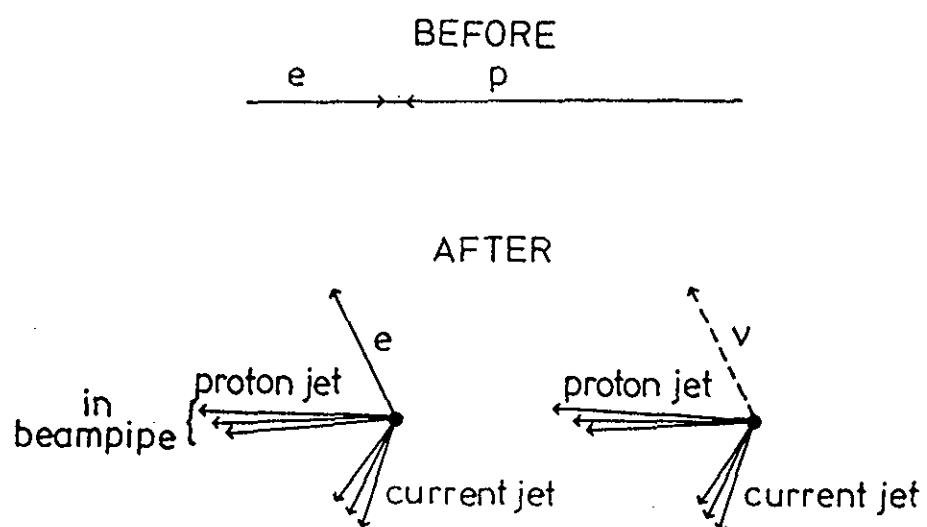
Fig. 5 Topology of deep inelastic ep scattering events.

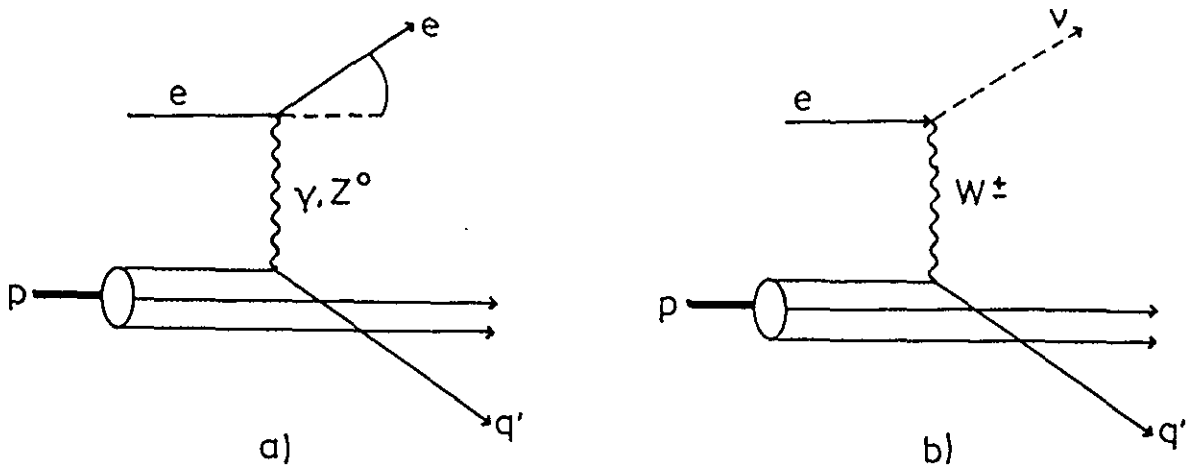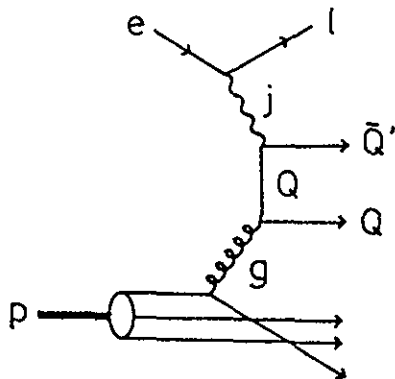there are two kinematic variables that describe the inclusive sacttering process:

$$q^2 = (p_e - p_e')^2 = -Q^2 \qquad \text{square of the four momentum transfer}$$

$$W^2 = (q + p_p)^2 \qquad \text{square of the total mass of the final hadronic system.}$$

or equivalently

$$x = \frac{Q^2}{2(q \cdot p_p)} = \frac{Q^2}{2m_p \nu} \qquad \text{the Bjorken scaling variable.}$$

$$y = \frac{(q \cdot p_p)}{(q \cdot p_e)} = \frac{\nu}{\nu_{max}}, \qquad \text{note that } Q^2 \simeq sxy.$$

In the rest system of the incoming proton ν measures the energy transferred by the current. The maximum value which ν can reach is

$$\nu_{max} = \frac{s - (m_e + m_p)^2}{2m_p} \approx \frac{s}{2m_p} = 2E_e E_p / m_p$$

For E_e = 30 GeV, E_p = 820 GeV: ν_{max} = 52 TeV. HERA therefore is equivalent to a fixed target experiment with an incident lepton beam of 52 TeV.

The variables Q^2, x, y can be determined either from the energy E_e' and scattering angle Θ_e of the outgoing electron, or from the energy E_j and production angle Θ_j of the current jet.

From the electron:

$$Q^2 = 2E_e E_e' (1 + \cos\Theta_e)$$

$$x = \frac{E_e' \cos^2 \Theta_e/2}{E_p (1 - (E_e'/E_e) \sin^2\Theta_e/2)}$$

$$y = 1 - E_e'/E_e \sin^2\Theta_e/2$$

From the current jet:

$$Q^2 = \frac{E_J^2 \sin^2\Theta_J}{1 - \frac{E_J}{2E_e}(1-\cos\Theta_J)}$$

$$y = \frac{E_J}{2E_e}(1-\cos\Theta_J) = \frac{E_J}{E_e}\sin^2\Theta_J/2$$

$$x = \frac{Q^2}{sy} = \frac{E_J \cos^2\Theta_J/2}{E_p(1 - \frac{E_J}{E_e}\sin^2\Theta_J/2)}$$

The angles are always measured with respect to the proton beam. In deriving the current jet results the mass of the jet has been neglected. As an illustration of the kinematics for 30 GeV electron colliding on 820 GeV protons, Figs. 6, 7 show in the x, Q^2 plane curves for fixed energy and angle of electron and current jet.

3.2   Qualitative Behaviour of the Scattering Cross Sections

It is instructive to make the following crude guess for the cross sections of neutral current (NC) and charged current (CC) scattering. Considering only γ and W exchange, respectively (Fig. 8a,b), they can be approximated by

$$\frac{d\sigma(\gamma p)}{dxdy} \approx \alpha^2 s \left(\frac{1}{Q^2}\right)^2 F(x,y) \qquad \text{NC}$$

$$\frac{d\sigma(Wp)}{dxdy} \approx \alpha^2 s \frac{1}{(Q^2+M_W^2)^2} F(x,y) \qquad \text{CC}$$

The W has been assumed to couple to leptons and quarks with the same coupling strength e as the γ and hence the appearence of the factor α^2 in both cases. The structure function $F(x,y)$ measures the momentum fraction x carried by the struck quark for a fixed value of y. The major difference between NC and CC cross sections stems from the different propagator contributions, Q^{-4} and $(Q^2 + M_W^2)^{-2}$, respectively, where $M_W = 82$ GeV is the W mass. Figure 8c compares the Q^2 dependence of
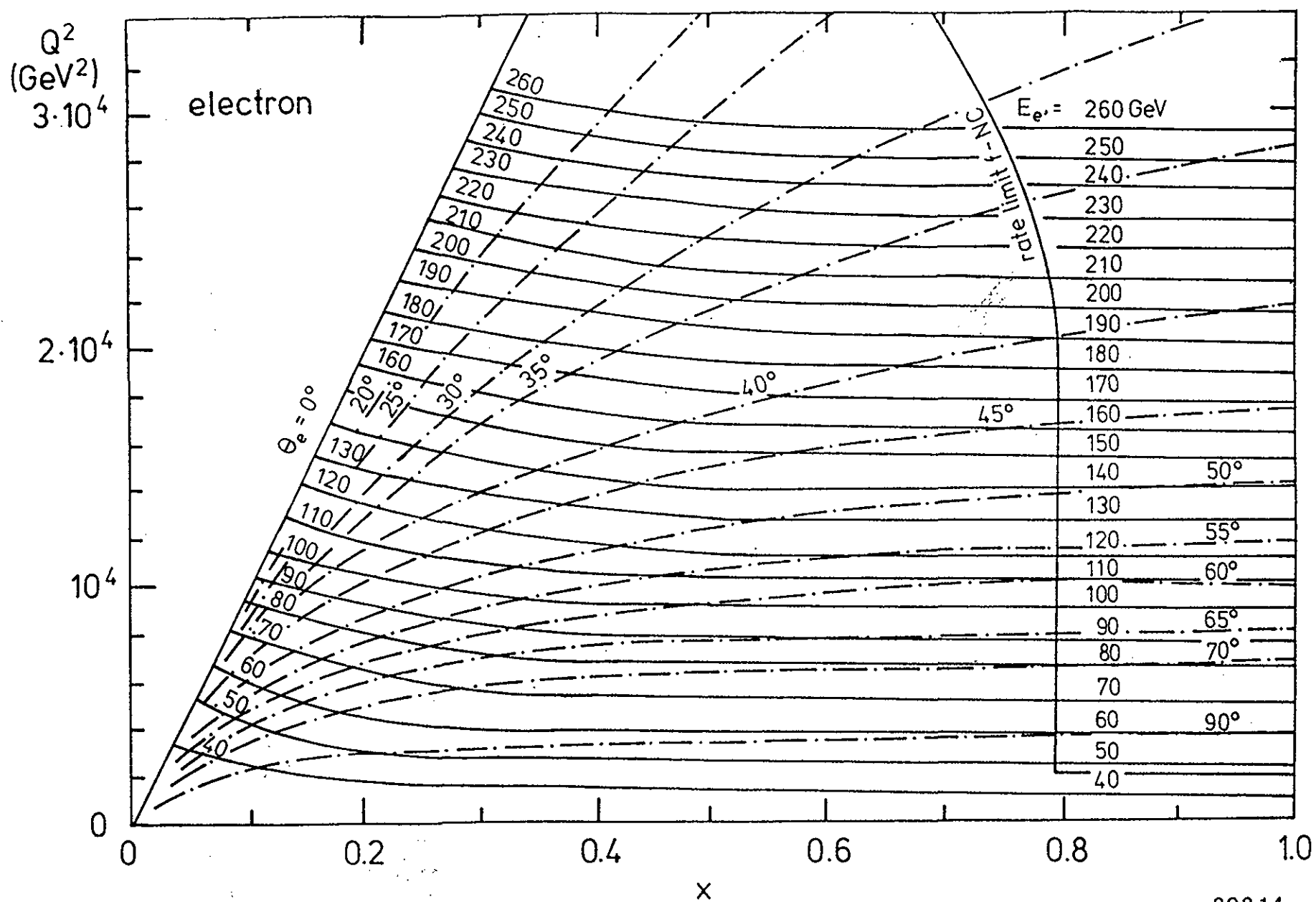
Fig. 6 30 GeV e + 820 GeV p: The x-Q^2 plane with lines of fixed electron scattering angle and energy.

39814
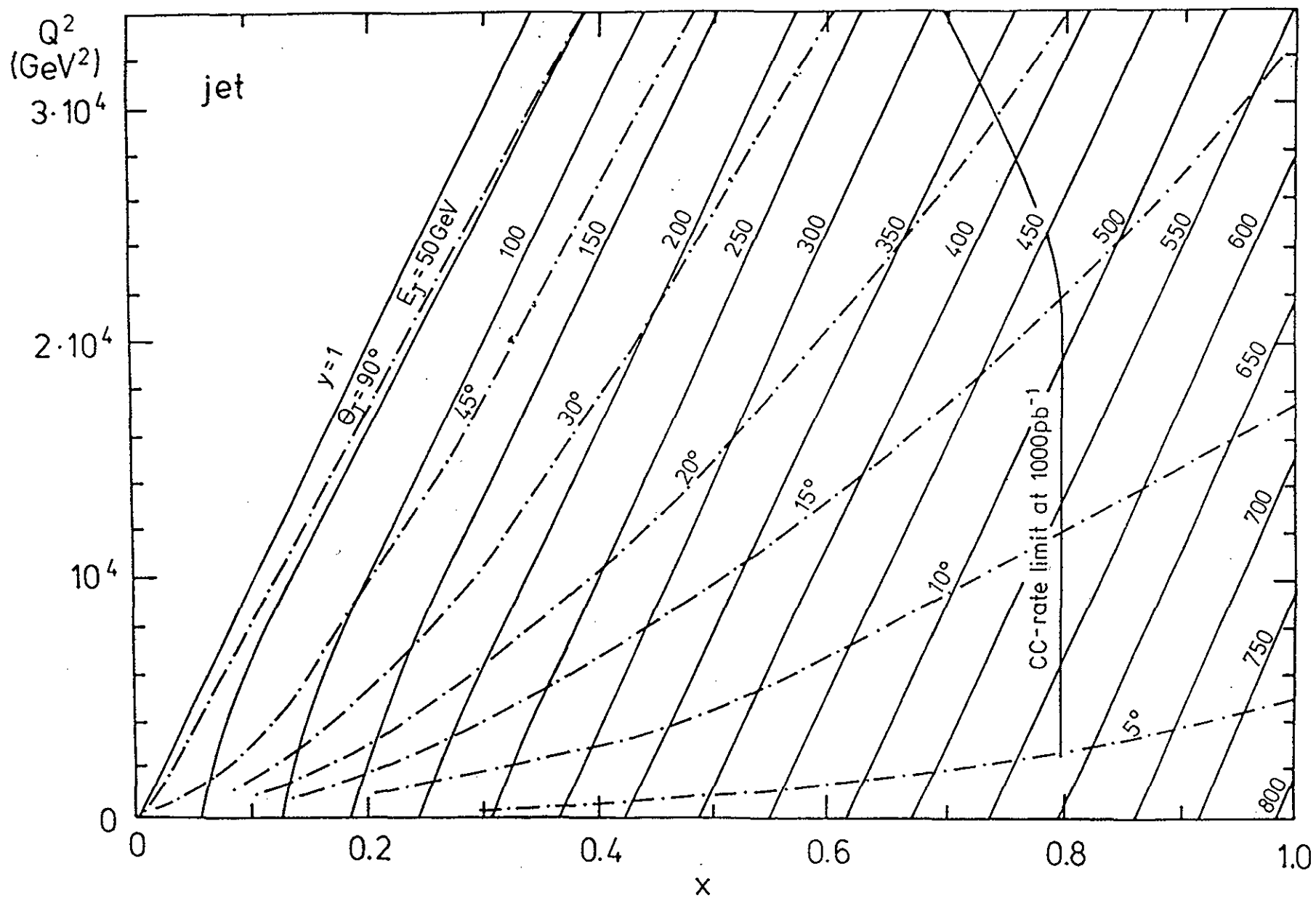
Fig. 7 30 GeV e + 820 GeV p: The x-Q^2 plane with lines of fixed current jet angle and energy.
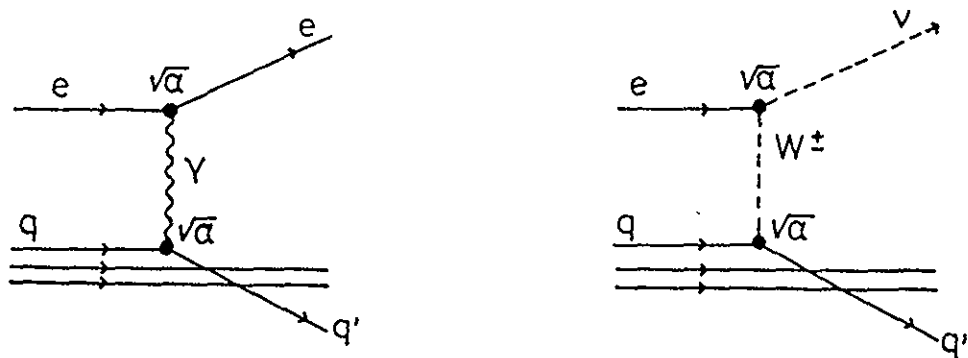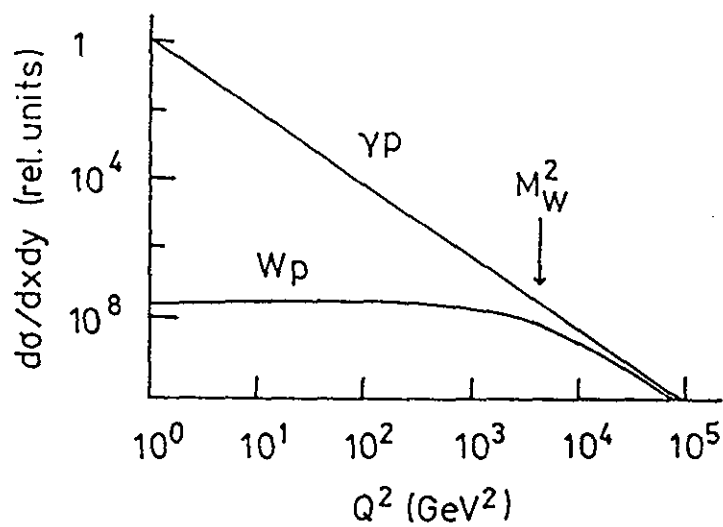
39813

Fig. 8a,b NC and CC scattering by γ and W exchange, respectively.

c) Qualitative behaviour of NC scattering by γ exchange
   and CC scattering by W exchange.

the two processes. Near $Q^2 = 0$ the NC cross section is $\sim 10^8$ times larger while for $Q^2 \gtrsim 10^4$ GeV^2 the weak contribution is of the same magnitude as the electromagnetic one.

We shall now present more precise expressions for the NC and CC cross sections.

3.3   Neutral Current Processes

The one photon exchange cross section can be written in terms of two dimensionless structure functions F_1, F_2 which are functions of ν, Q^2 or x,y:

$$\frac{d^2\sigma(\gamma)}{dxdy} = \frac{4\pi\,\alpha^2}{s\,x^2y^2} \left[(1 - y)F_2(x,Q^2) + xy^2\,F_1(x,Q^2) \right]$$

In the approximation that scattering on spin 1/2 partons dominates F_1 can be expressed in terms of F_2 using the Callan - Gross relation: $2xF_1 = F_2$.

This leads to

$$\frac{d^2\sigma(\gamma)}{dxdy} \approx \frac{4\pi\,\alpha^2}{s\,x^2y^2}\;(1 - y + \tfrac{y^2}{2})\,F_2(x,Q^2)$$

In the quark picture, ep scattering is described as incoherent eq scattering with x measuring the fractional momentum of the struck quark. The structure functions can then be expressed in terms of the quark distribution functions u(x), d(x),...* where u,d,... give the number of u,d,... quarks with fractional momentum between x and x + dx:

$$F_2(x) = 2xF_1(x) = x[q(x) + \bar{q}(x)]$$

where for the electromagnetic current

$$q(x) = \tfrac{4}{9}u(x) + \tfrac{1}{9}d(x) + \tfrac{1}{9}s(x) + \tfrac{4}{9}c(x)\;.$$

At Q^2 values above 10^4 GeV^2 the contribution from Z^o exchange becomes comparable to that from photon exchange. Formally, the cross section

---

* The quark distribution functions as well as the structure functions depend on x and Q^2. For ease of writing the Q^2 dependence is not shown.

can be written as before,

$$\frac{d^2\sigma(\gamma + Z^0)}{dxdy} = \frac{4\pi \alpha^2}{s \, x^2 y^2} \left[(1 - y)F_2(x,Q^2) + y^2 x F_1(x,Q^2) \right]$$

where now the structure functions F_1 and F_2 receive contributions from γ exchange, from Z^0 exchange and from the interference between the two processes. In terms of the quark distribution functions the cross section reads for left (right) handed electrons, allowing for left handed (L) and right handed (R) incoming electrons:[4]

$$\frac{d^2\sigma}{dxdy} = \frac{\pi\alpha^2}{sx^2 y^2} \sum_q \{ xq(x)(A_q + (1-y)^2 B_q) + x\bar{q}(x)(B_q + (1-y)^2 A_q) \}$$

with

$$A_q = \left(-Q_q + g_{Lq} g_{Le} \frac{Q^2}{Q^2 + M_Z^2} \right)^2 + \left(-Q_q + g_{Rq} g_{Re} \frac{Q^2}{Q^2 + M_Z^2} \right)^2$$

$$B_q = \left(-Q_q + g_{Rq} g_{Le} \frac{Q^2}{Q^2 + M_Z^2} \right)^2 + \left(-Q_q + g_{Lq} g_{Re} \frac{Q^2}{Q^2 + M_Z^2} \right)^2$$

and

$$g_{Li} = \frac{I_L^3 - Q_i \sin^2\Theta_W}{\sin \Theta_W \cos \Theta_W} \qquad g_{Ri} = \frac{-Q_i \sin^2\Theta_W}{\sin\Theta_W \cos\Theta_W}$$

where the Q_i, $i = q,e$ measure the charges of the incoming quark and lepton, I_L^3 is the weak isospin of the lepton ($I_{e-}^3 = -1/2$, $I_{e+}^3 = 1/2$), and Θ_W is the weak mixing angle, $\sin^2\Theta_W = 0.225 \pm 0.005 \pm 0.006$.[5]

The final expression of the cross section for left (L) or right (R) handed electron proton scattering reads[6]

$$\frac{d^2\sigma}{dxdy}\left(e^-\begin{Bmatrix} L \\ R \end{Bmatrix} + p \to e^- \begin{Bmatrix} L \\ R \end{Bmatrix} X\right) =$$

$$\frac{4\pi\alpha^2}{s(xy)^2}\left[Q_u^2\left(u(x) + \bar{u}(x)\right) + Q_d^2\left(d(x) + \bar{d}(x)\right)\right]x\left(1 - y + y^2/2\right)$$

$$+ \frac{\alpha}{xy}\frac{\sqrt{2}\,G_F\,M_Z^2}{sxy + M_Z^2}\begin{Bmatrix} 1 - 2\sin^2\vartheta_W \\ -2\sin^2\vartheta_W \end{Bmatrix}\cdot$$

$$\cdot\left\{\left[Q_u(1 - 4\,Q_u\sin^2\vartheta_W)\left(u(x) + \bar{u}(x)\right)\right.\right.$$

$$\left.\left. - Q_d(1 + 4\,Q_d\sin^2\vartheta_W)(d(x) + \bar{d}(x))\right]\cdot(1 - y + y^2/2)\right\} +$$

$$+ \frac{\alpha}{xy}\frac{\sqrt{2}\,G_F\,M_Z^2}{sxy + M_Z^2}\begin{Bmatrix} 1 - 2\sin^2\vartheta_W \\ 2\sin^2\vartheta_W \end{Bmatrix}\cdot$$

$$\cdot\left\{Q_u\left(u(x) - \bar{u}(x)\right) - Q_d(d(x) - \bar{d}(x))\right\}xy\left(1 - y/2\right) +$$

$$+ \frac{s}{4\pi}\frac{G_F^2\,M_Z^4}{(sxy + M_Z^2)^2}\begin{Bmatrix} (1 - 2\sin^2\vartheta_W)^2 \\ 4\sin^4\vartheta_W \end{Bmatrix}\cdot$$

$$\cdot\left\{\left[(1 - 4\,Q_u\sin^2\vartheta_W + 8\,Q_u^2\sin^4\vartheta_W)\left(u(x) + \bar{u}(x)\right) + \right.\right.$$

$$\left.\left. + (1 + 4\,Q_d\sin^2\vartheta_W + 8\,Q_d^2\sin^4\vartheta_W)\left(d(x) + \bar{d}(x)\right)\right]\cdot(1 - y + y^2/2)\right\} +$$

$$+ \frac{s}{4\pi}\frac{G_F^2\,M_Z^4}{(sxy + M_Z^2)^2}\begin{Bmatrix} (1 - 2\sin^2\vartheta_W)^2 \\ -4\sin^4\vartheta_W \end{Bmatrix}\cdot$$

$$\cdot\left\{\left[(1 - 4\,Q_u\sin^2\vartheta_W)\left(u(x) - \bar{u}(x)\right) + \right.\right.$$

$$\left.\left. + (1 + 4\,Q_d\sin^2\vartheta_W)(d(x) - \bar{d}(x))\right]xy\left(1 - y/2\right)\right\}$$

with $Q_u = 2/3$ and $Q_d = -1/3$.

Here use has been made of the prediction by the standard theory,

$$M_Z = \frac{\pi\alpha}{G_F/\sqrt{2}}\frac{1}{\sin\Theta_W\,\cos\Theta_W}$$

where G_F is the fermi coupling constant, $G_F = \dfrac{1.02 \cdot 10^{-5}}{M_p^2}$. To simplify the writing, only the $u, \bar{u}$ and $d, \bar{d}$ contributions are shown.

The expected event rates have been calculated in Ref. 7 using the structure functions of Ref. 8 for an integrated luminosity of 200 pb^{-1} expected after 2 years of data taking. The results are shown in Fig. 9. Note that events with $x < 0.01$ and $y < 0.01$ have been suppressed. There are $3 \cdot 10^6$ events with Q^2 values between 3 and 10^4 GeV^2. Roughly a thousand events have Q^2 values above 10^4 GeV^2 where Z^0 effects dominate. If we demand a minimum of a hundred events we see that neutral currents can be studied with sufficient statistics up to Q^2 values of $3 \cdot 10^4$ GeV^2. The small dark corner with $Q^2 < 200$ GeV^2, $y < 0.004$ marks the kinematical region that has so far been explored experimentally. HERA will extend the kinematic region by two orders of magnitude in either variable.

3.4 Charged Current Processes

Charged current reactions, $e^-p \rightarrow \nu X$, proceed through W^- exchange. The cross section for left handed electrons can be written in terms of three structure functions F_1, F_2 and F_3:

$$\frac{d^2\sigma}{dxdy}(e_L^- p \rightarrow \nu X) = \frac{G_F^2 s}{\pi} \frac{1}{(1 + Q^2/M_W^2)^2}$$

$$[(1 - y)F_2(x,Q^2) + y^2 xF_1(x,Q^2) + (y - \frac{y^2}{2}) xF_3(x,Q^2)]$$

The cross section for right handed electrons vanishes since the neutrino is left handed.

$$\frac{d^2\sigma}{dxdy}(e_R^- + p \rightarrow \nu + X) = 0$$

The quark-parton expression for the structure functions is:

$$F_2(x) = 2xF_1(x) = x[q(x) + \bar{q}(x)]$$
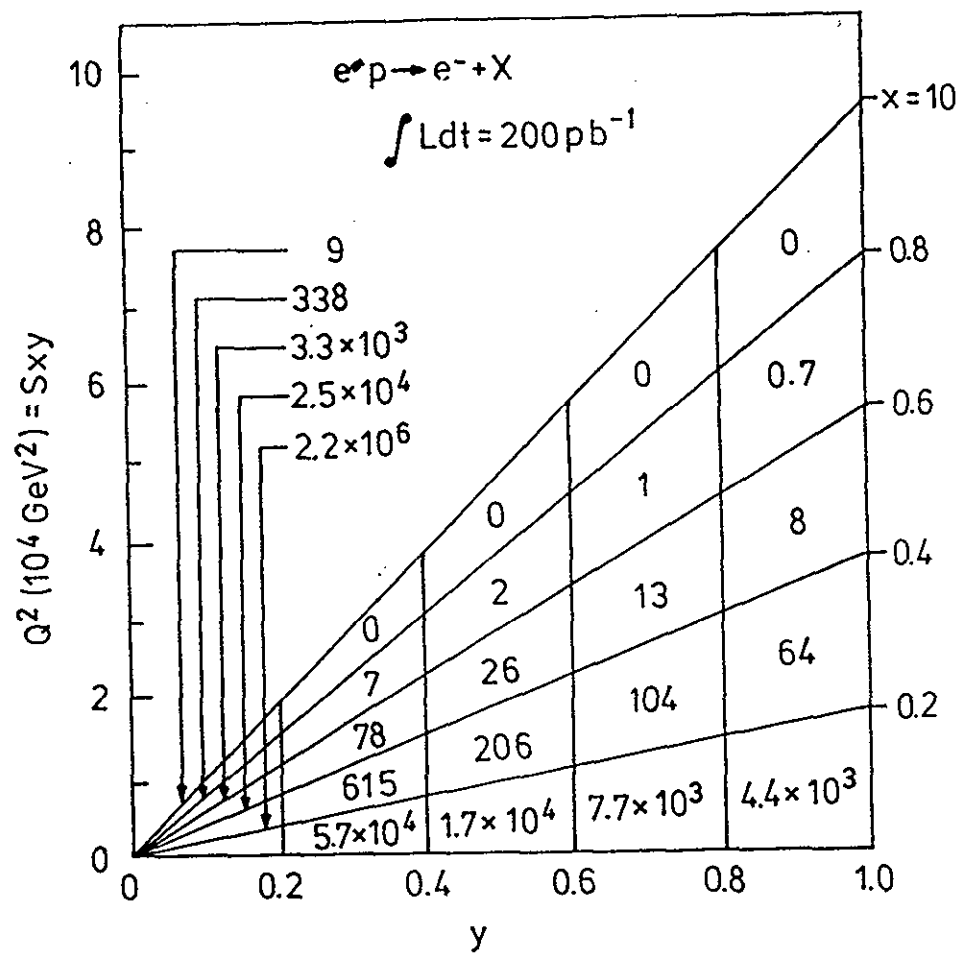
$$xF_3(x) = x[q(x) - \bar{q}(x)]$$

Fig. 9   Event rates for $e^- p \rightarrow e^- X$ with $x > 0.01$ and $y > 0.01$.
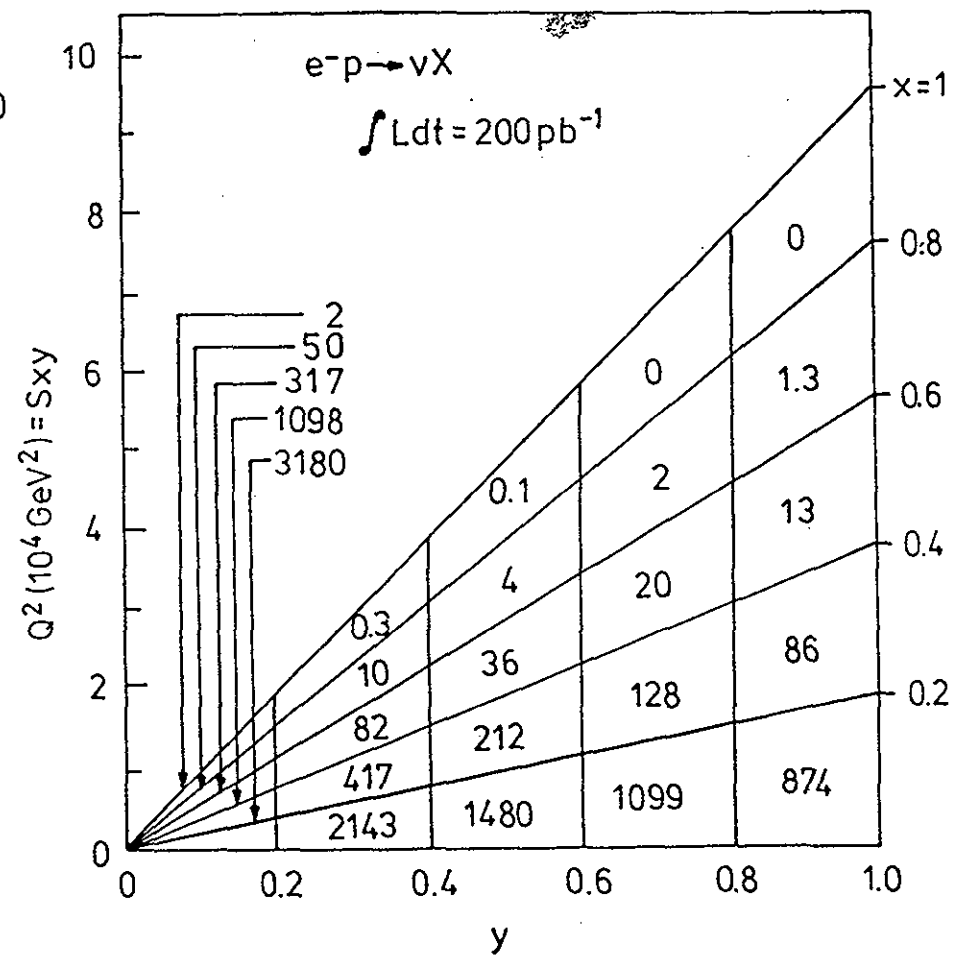

Fig. 10   Event rates for $e^- p \rightarrow \nu X$ with $x > 0.01$ and $y > 0.01$.

39806

where

$$q(x) = u(x) + c(x) + \ldots$$

$$\bar{q}(x) = \bar{d}(x) + \bar{s}(x) + \ldots$$

This leads to

$$\frac{d^2\sigma}{dxdy}(e_L^- p \to \nu + X) = \frac{G_F^2 s}{\pi} \frac{1}{(1 + Q^2/M_W^2)^2} x\{ u(x) + (1 - y)^2\bar{d}(x)\}$$

where the higher mass quarks have been omitted. The expected event rates are shown in Fig. 10. They have been calculated[7] for the same luminosity as above. Roughly 10 000 events are produced at $Q^2 < 10^4$ GeV^2 and 1000 events at $Q^2 > 10^4$ GeV^2. Figure 10 shows that charged currents can be studied with sufficient statistics up to ~$4 \cdot 10^4$ GeV^2.

A precise determination of the structure functions will open the way to address several fundamental questions.

3.5.1 Test of QCD

The large Q^2 range accessible at HERA will allow a stringent test of QCD which predicts logarithmically falling structure functions. Mass corrections and higher twist contributions which affect present experiments should be negligible at HERA. Gluon radiation as illustrated in Fig. 11 leads to scale breaking of the form

$$F(x) \to \frac{F(x)}{1 + c\ell n(Q^2/\Lambda^2)}$$

The available structure function data span the Q^2 range 0-300 GeV^2; at HERA it will increase to 40 000 GeV^2. This will enhance greatly the sensitivity to power terms (in Q^2) whose presence would be at variance with QCD.

The accuracy with which one can hope to measure the QCD scale parameter is around ±40 MeV for Λ_{QCD} = 200 MeV.
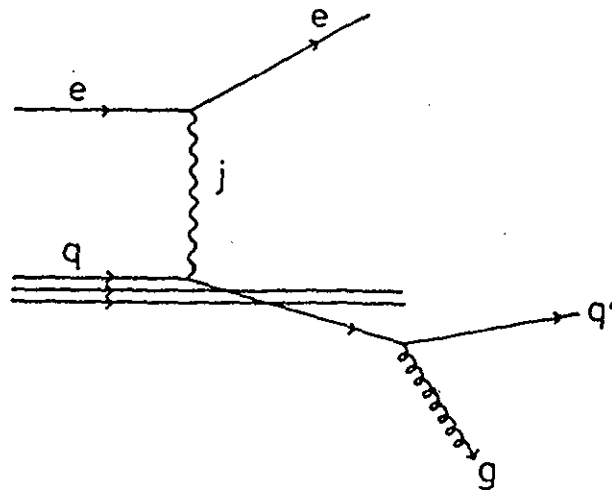
39796

Fig. 11 eq scattering with accompanying gluon bremsstrahlung.

a)   b)
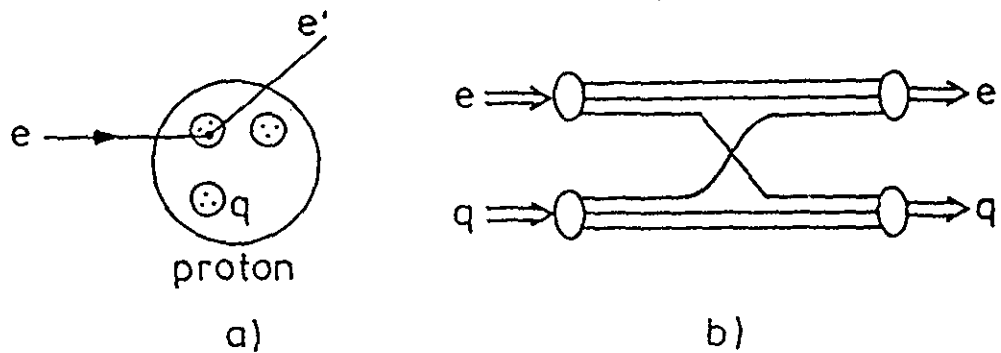
39810

Fig. 12 a) Electron scattering on composite quarks.

b) Composite electron and quark scattering by
   constituent interchange.

3.5.2 Structure of quarks and electrons

If quarks and/or electrons are extended objects the structure functions will show power law type deviations from their QCD predicted values. The sensitivity to possible structure of quarks and electrons has been estimated with the help of a model[9] which assumes quarks and electrons to be composites and to have common constituents (Fig. 12). The interchange of the constituents leads to a contact term of the form

$$\mathcal{L} \sim \frac{g^2}{\Lambda^2} \ \bar{e}_\alpha \gamma^\mu e_\alpha \bar{q}_\beta \gamma_\mu q_\beta$$

where α, β denote states of a definite helicity, $\alpha = L,R$; $\beta = L,R$. The mass parameter Λ sets the compositness scale; g measures the coupling strength. For the following $g^2/4\pi = 1$ will be assumed. Figure 13 shows the ratio of the structure functions F_2 obtained with the contributions from $\gamma + Z^0$ exchange and the contact interaction, and for γ exchange alone:

$$F_2(\gamma + Z^0 + C.I.)/F_2(\gamma)$$

The ratio is shown as a function of Q^2 and x for different Λ values. At Q^2 values above 10^4 GeV^2 a contact interaction with $\Lambda = 1$ TeV leads to large deviations - factors of 5 to 10 - from the standard results. Given two years of data taking HERA will be sensitive up to Λ values of ~7 TeV corresponding to distances of $3 \cdot 10^{-18}$ cm. The present lower limits on Λ are 2-4 TeV on e,μ from $e^+e^- \rightarrow \mu^+\mu^-$ and 300 GeV for quarks from the total cross section for e^+e^- annihilation into hadrons.[10] A theoretical analysis of some composite models has indicated that the energy of HERA would still be insufficient to see structure in the quarks and electrons.[11] It suggests a lower as well as an upper limit on Λ:

$$\lambda(20 - 30)\text{TeV} < \Lambda < 250 \text{ TeV}$$

- The lower limit is deduced from the limit on the decay $K^+ \rightarrow \pi^+\mu e$; λ is a number of order unity. The upper limit stems from cosmological considerations.
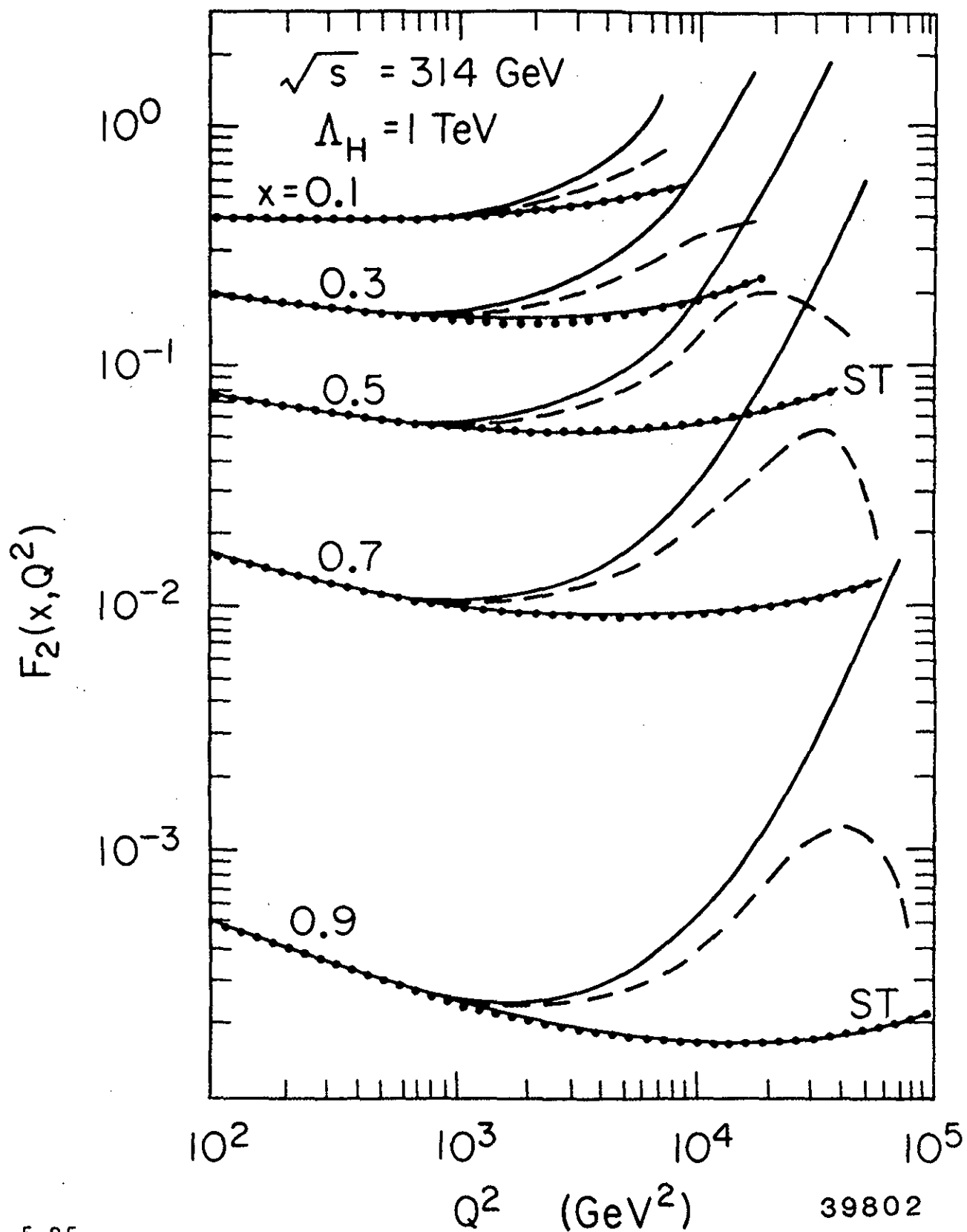
Fig. 13 The ratio $F_2(\gamma + Z^0 + C.I)/F_2(\gamma)$ for composite electron quark scattering.

5-85

39802

3.5.3 New currents

Altarelli et al.[3] have estimated the effect of a second W_2 on the rate of charged current events. The amplitude for the exchange of the standard $W(W_1)$ can be written as

$$A(Q^2) \sim \frac{g^2}{8(Q^2 + m_W^2)} \sim \frac{G_F/\sqrt{2}}{1 + Q^2/m_W^2} \, .$$

Under the assumption that the second W couples in the same way to leptons and quarks the amplitude can be written as

$$A_{1+2}(Q^2) \sim \frac{g_1^2}{8(Q^2 + m_1^2)} + \frac{g_2^2}{8(Q^2 + m_2^2)} \, .$$

The coupling constants g_1, g_2 have to be chosen such that the low Q^2 region remains unchanged, i.e.

$$A(0) \equiv \frac{G_F}{\sqrt{2}} = A_{1+2}(0) = \frac{g_1^2}{8m_1^2} + \frac{g_2^2}{8m_2^2} \equiv \frac{g_2^2}{8m_W^2} \, .$$

Taking $m_1 = m_W$ and defining $r = g_2^2/g^2$ the ratio of the cross sections for two W's over one W is given by

$$\frac{\sigma(W_1 + W_2)}{\sigma(W_1)} = \left[1 - r \, \frac{m_1^2}{m_2^2} + r \, \frac{m_1^2}{m_2^2} \, \frac{1 + Q^2/m_1^2}{1 + Q^2/m_2^2} \right]$$

The ratio is shown in Fig. 14 for different W_2 masses assuming $r = 1$. For m_2 around 200 GeV large deviations from the standard theory result will be observed. The deviations become smaller as m_2 increases. With two years of data taking one will be sensitive to W_2 masses up to ~800 GeV.

A similar result holds for neutral currents and additional Z^0's.

3.5.4 Right handed currents

One of the great mysteries of weak interactions is the asymmetry between left and right handedness; there are left handed neutrinos and
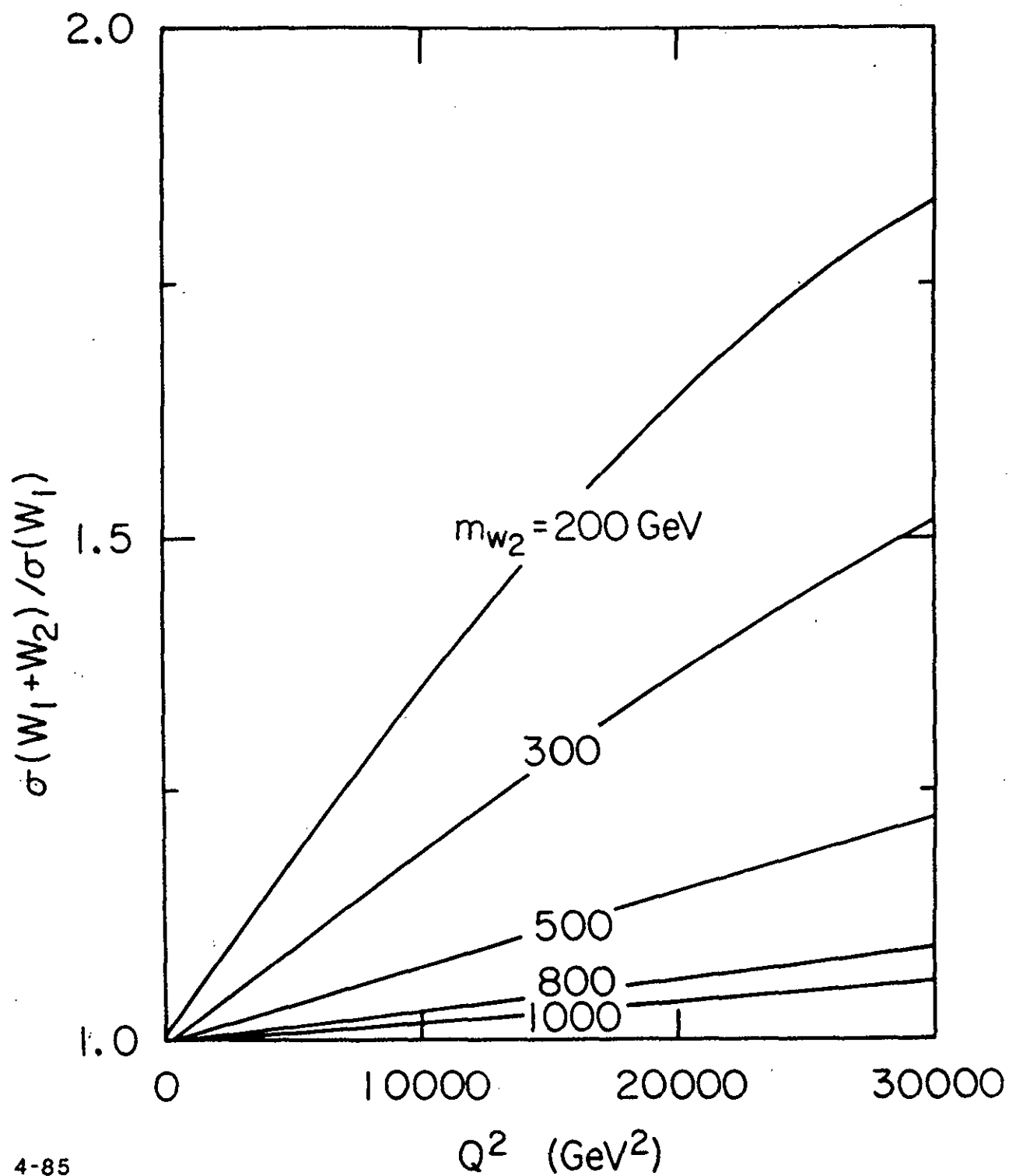
Fig. 14. The ratio of the cross sections for two and one W.

4-85

39801

left handed currents and no right handed counter parts. It has long been speculated that left-right symmetry is restored at some higher energy; namely there exist heavy right handed neutrinos N_R that couple to a right handed W_R.[12] The mass of N_R has been related to the masses of the corresponding charged lepton, m_e, and the left handed neutrino m_ν:[13] $m_{NR} \approx m_e^2/m_\nu$. For electrons this leads to the following prediction for m_{N_R}:

m_ν (eV)	0.1	1	10
m_{N_R} (GeV)	2611	261	26

Several experimental and theoretical limits have been put on the mass of W_R:

β decay of μ's
if ν is a Dirac spinor: $M_R > 380$ GeV   (Ref.14)

if ν is a Majorana spinor: no limit

Nonleptonic decays $M_R > 200\text{-}300$ GeV (Ref.15)

$K_S^0 - K_L^0$ mass difference

educated guess: $10 < M_R < 100$ TeV (Ref.16)

The lower limit on a right handed Z^0 is $M_{Z_R} \geq 150$ GeV provided $\sin^2\Theta_W < 0.25$ (Ref.15). However, a simple Higgs structure leads to $M(Z_R)/M(W_R) \approx 1.6$. This suggests also $M(Z_R)$ to be in the region of tens of TeV (Ref. 17).

3.5.5 Search for right-handed currents with longitudinally polarized electrons

Longitudinally polarized electrons make HERA ideally suited to search for right handed currents. Any nonzero cross section contribution to $e_R^- p \rightarrow \nu X$ or $e_L^+ p \rightarrow \bar{\nu} X$ scattering signals the presence of a right handed charged current (see Sect. 3.4). In the absence of a W_R contribution:

$$\frac{d^2\sigma}{dxdy} \begin{pmatrix} e_L^- p \\ e_R^+ p \\ e_R^- p \\ e_L^+ p \end{pmatrix} = \frac{G_F^2 s}{\pi} \frac{x}{(1 + Q^2/M_W^2)^2} \begin{pmatrix} (u+c)+(1-y)^2(\bar{d}+\bar{s}) \\ (d+s)+(1-y)^2(\bar{u}+\bar{c}) \\ 0 \\ 0 \end{pmatrix}$$

For neutral current reactions the situation is different. The photon is blind to the helicity of the electron but the Z^0 gives different contribution to e_L and e_R scattering as shown in sect. 3.3. Figure 15 shows the difference between the cross sections for $e_{L,R}^-$ and $e_{L,R}^+$ scattering. They amount to ~60 % at Q^2 values of 10^4 GeV^2.

4. PRODUCTION OF NEW PARTICLES

4.1 Pair Production of Heavy Quarks

Photon-gluon fusion (Fig. 4) will be a strong source of heavy quarks. A discussion of the process can be found in Ref. 18. The total cross section depends on the quark mass approximately as

$$\sigma(eq \rightarrow Q\bar{Q}X) \sim M_Q^{-4}$$

Given a t quark mass of 40 GeV and a luminosity of 200 pb^{-1} the expected number of $t\bar{t}$ events is a few hundred. Top-like quarks can be searched for up to masses of 100 - 120 GeV.

The heavy quarks will essentially be photo produced ($Q^2 \approx 0$) and will be emitted in the direction of the incoming proton. Given the high mass these heavy quarks will decay into many particles (~20 - 25 for m_t = 40 GeV) which are isotropically distributed in the plane perpendicular to the beams. Thus, the production of new heavy quarks should be discernible from other processes. Figure 16 shows for illustration the production of a $t\bar{t}$ pair assuming M_t = 40 GeV.

Another possible source of Q production might be an intrinsic $Q\bar{Q}$ component in the nucleon. It has been argued for instance[19] that the $c\bar{c}$ component could be as large as 1 % and could become an important contributor once Q^2 exceeds ~4 M_c^2.

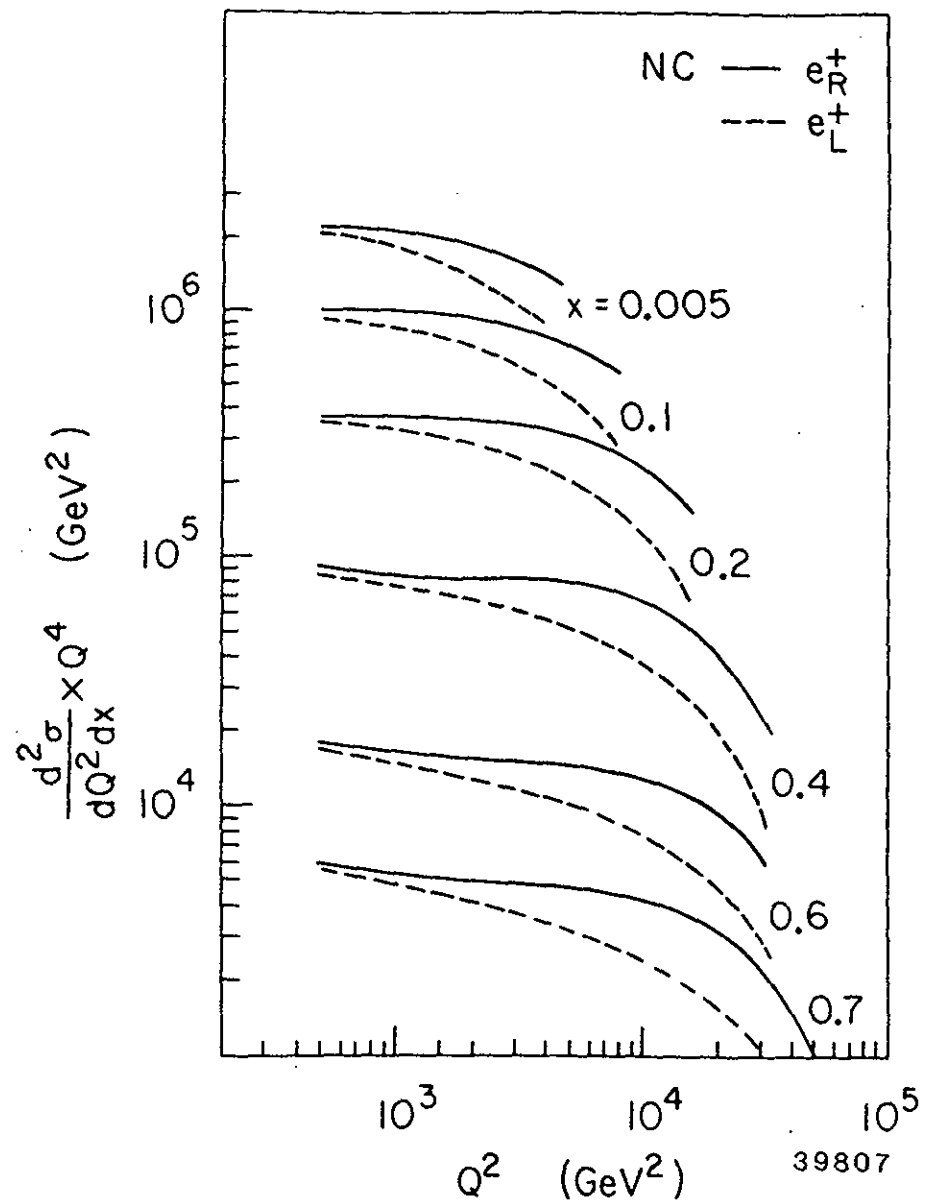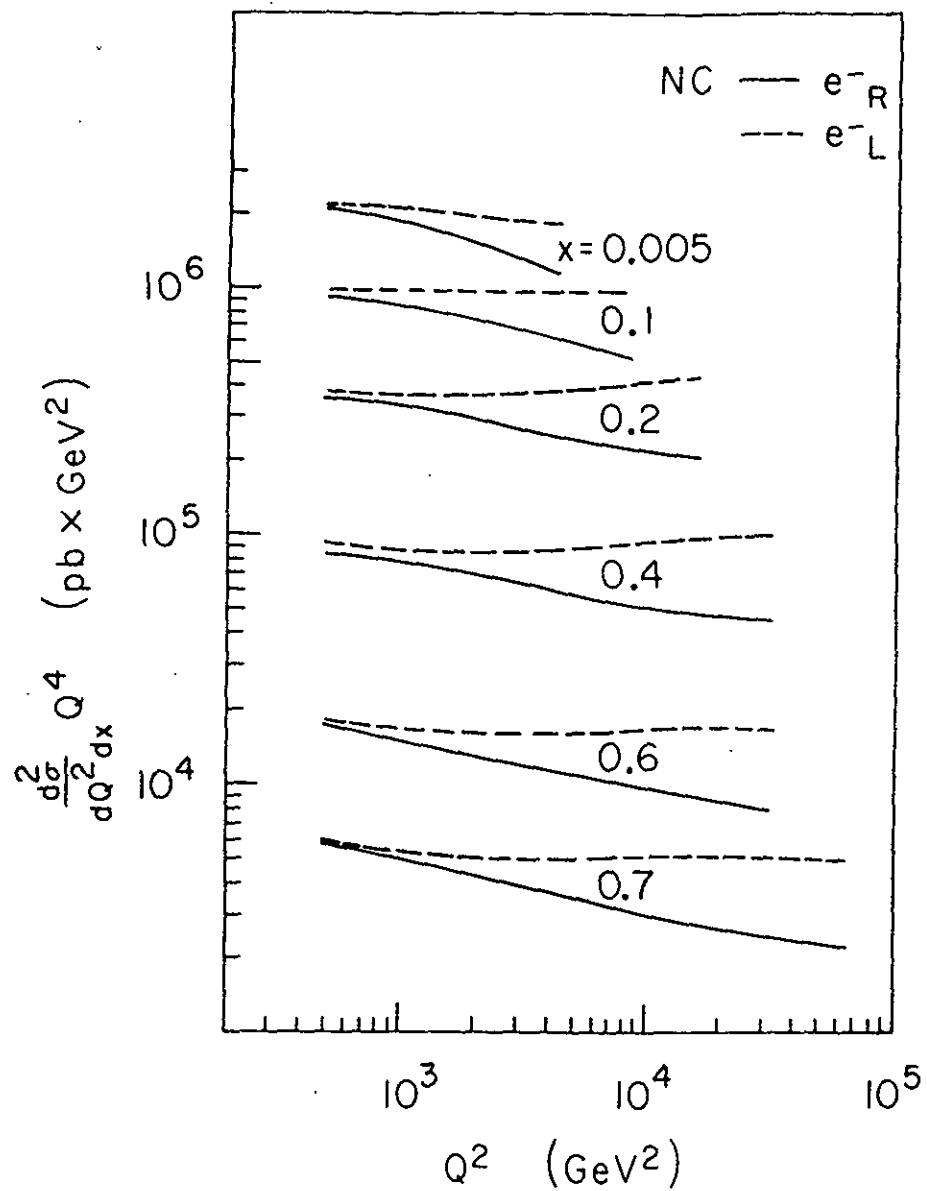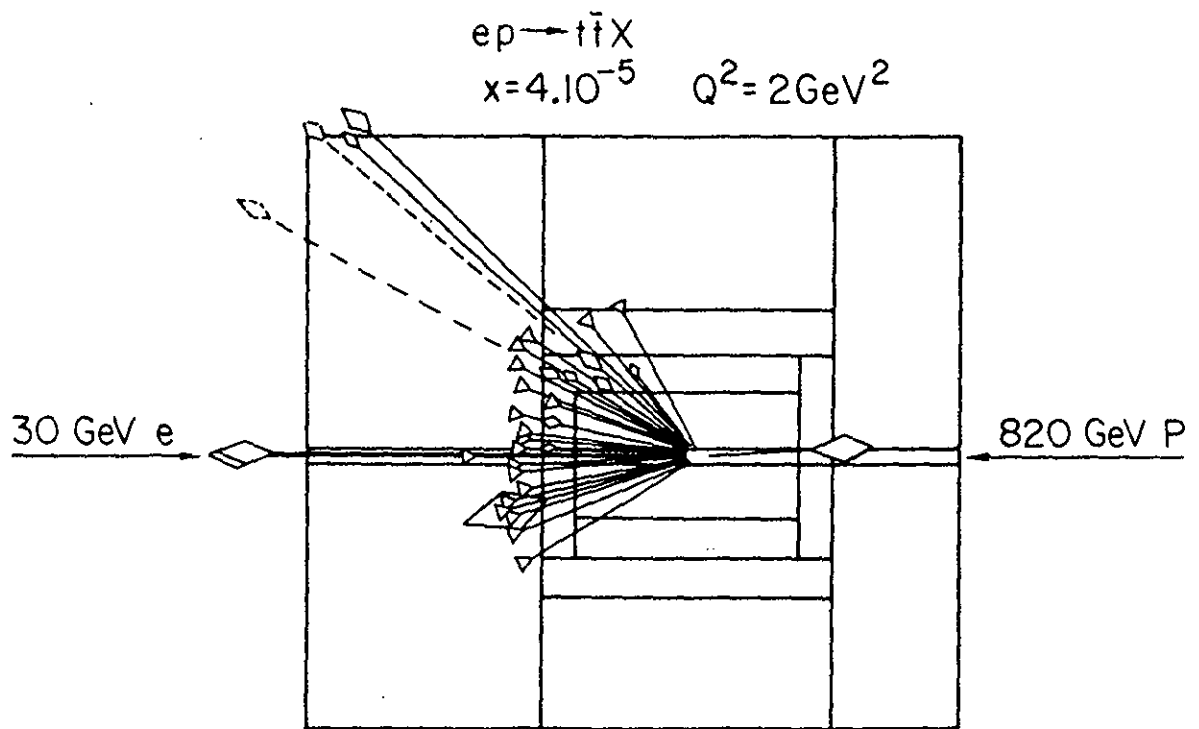Fig. 15 The neutral current cross section for left and right handed $e^{\pm}$.

$$ep \rightarrow t\bar{t}X$$
$$x = 4.10^{-5} \quad Q^2 = 2\,GeV^2$$

30 GeV e

820 GeV P

39794

Fig. 16 Example of a $t\bar{t}$ production event.

4.2 Vector Boson Production

Z^O and $W^{\pm}$ production is expected to proceed predominantly through the diagrams shown in Fig. 17a. The total cross sections are predicted to be[20]

$$\sigma(ep \rightarrow Z^O X) \approx 0.1 \text{ pb}$$

$$\sigma(ep \rightarrow W^{\pm}X) \approx 0.05 \text{ pb}$$

leading to ~20 Z^O events and ~10 $W^{\pm}$ events for 200 pb^{-1}.

In the (unlikely) case that Z^O and $W^{\pm}$ have also a strongly inter-acting component the time honoured pomeron exchange (Figs. 17b) may add to their production rate.

4.3 Higgs Production

Possible diagrams for production of Higgs particles are shown in Fig. 18. For a total of 200 pb^{-1} the expected yield of Higgs produced is not overwhelming[21]:

$M_H =$	10	20	50	100 GeV
number of events =	10	10	10	3

4.4 Excited Quarks and Leptons

If quarks and leptons are composites the existence of excited quarks and leptons q* ,e* appears to be natural (remember p,Δ). Their pro-duction would follow the diagrams of Fig. 19. The production rates are sufficient to search for q* ,e* up to masses of 250 GeV.[22]

4.5 New Currents, Quarks, Leptons

Suppose there exist new currents X^O, $X^{\pm}$ which link the known quarks and leptons to new quarks Q = U,D,S,C,B,T and leptons L, with coupling strengths equal to that of the standard weak interactions. The cross section for the dominant associated production of D and L^O as depicted in Fig. 20 is given by
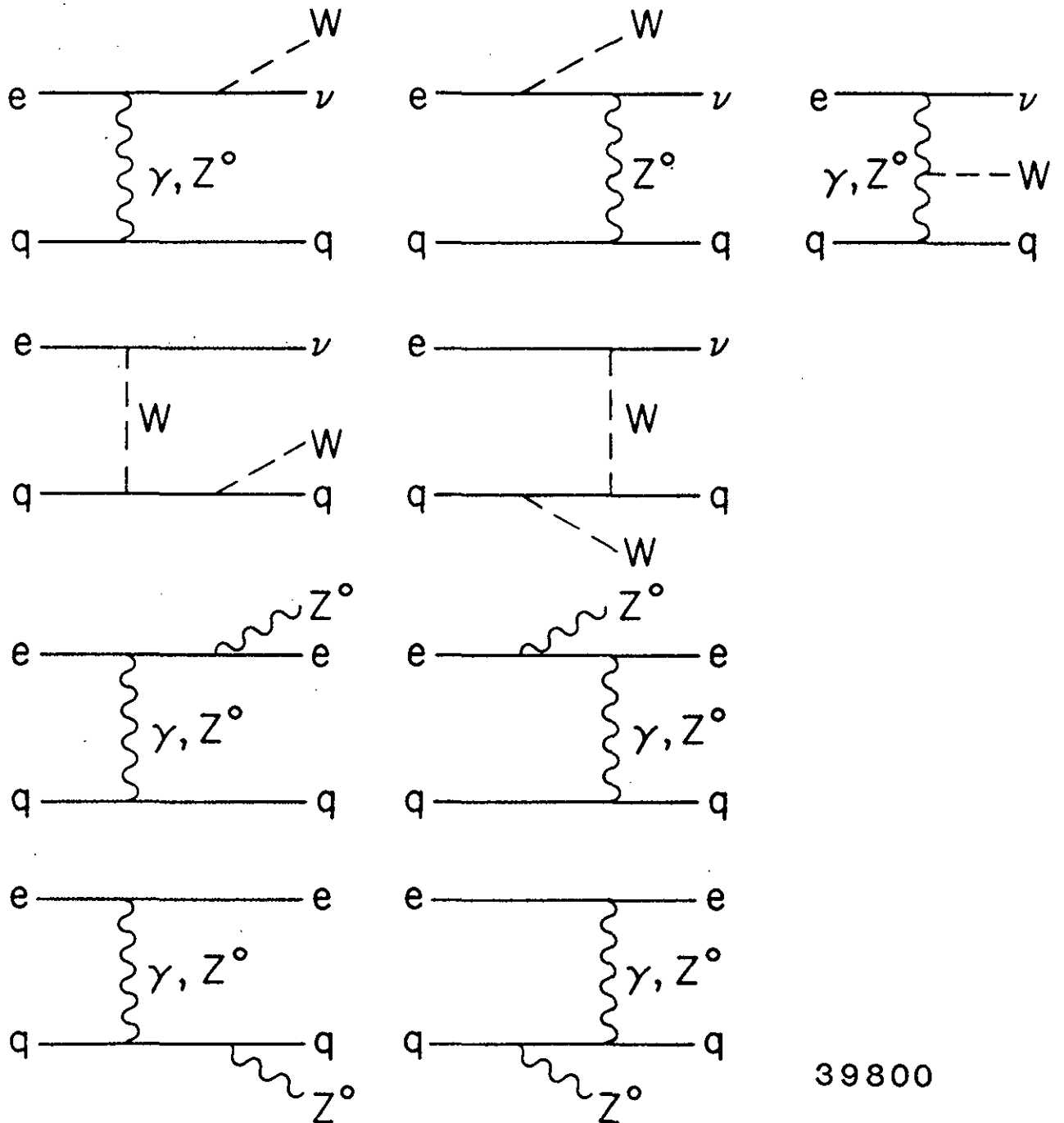
Fig. 17a Diagrams for Z^0 and $W^\pm$ production.

39800

Fig. 17b Diagrams for Z^0, $W^\pm$ production by pomeron exchange.

Fig. 18 Diagrams for Higgs production.
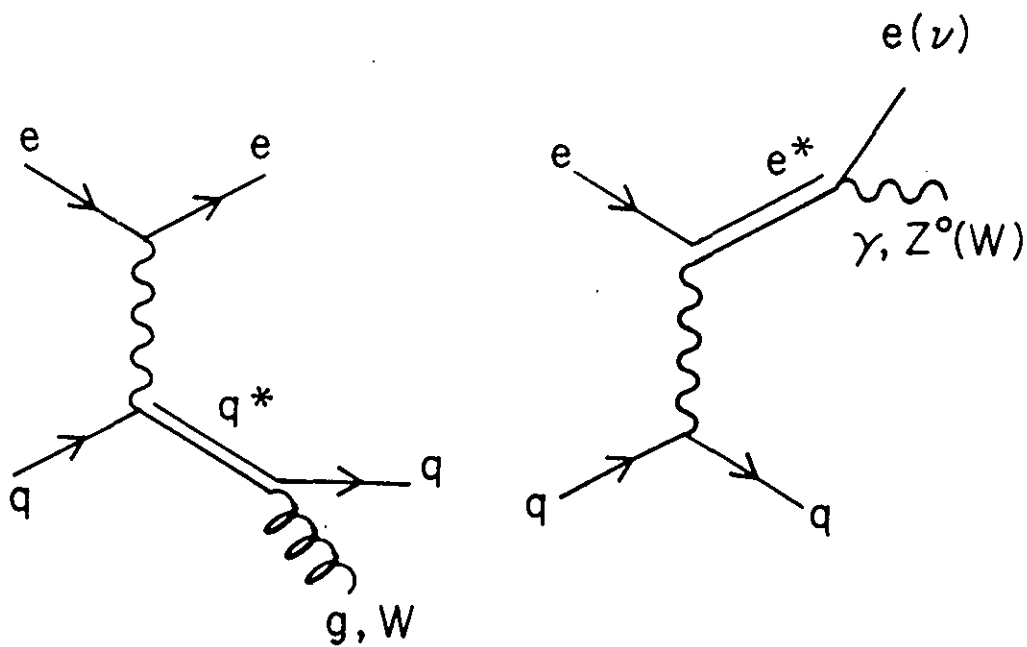
39798

Fig. 19 Diagrams for the production of excited quarks and leptons.

$$\frac{d\sigma}{dxdy} = \frac{G_F s}{2} \left(\frac{m_W}{m_X}\right)^4 \frac{1}{(1 + \frac{sxy}{M_X^2})}$$

$$\left\{ xq(x) \left(1 - \frac{m_L^2 + m_D^2}{sx}\right) + x\bar{q}(x) \left(1 - y - \frac{m_L^2}{sx}\right) \left(1 - y - \frac{m_D^2}{sx}\right)\right\}$$

where

$$q(x) = u(x) + c(x) + \ldots$$

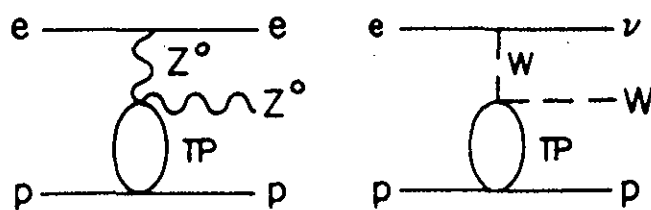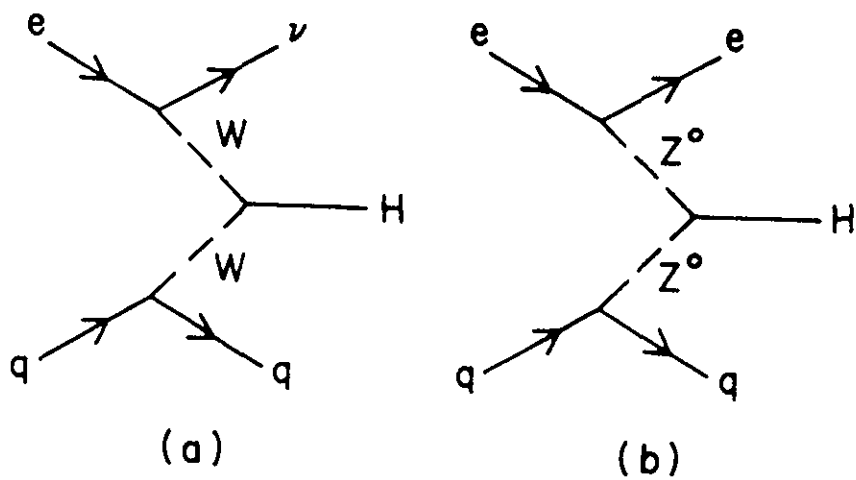$$\bar{q}(x) = \bar{d}(x) + \bar{s}(x) + \ldots$$

The kinematically allowed regions for x and y are

$$\frac{(m_L + m_D)^2}{s} < x < 1$$

$$y_- < y < y_+$$

$$y_\pm = \frac{1}{2sx} \left[sx - m_D^2 - m_L^2 \pm \sqrt{(sx - m_D^2 - m_L^2)^2 - 4m_D^2 m_L^2} \right]$$

The process will lead to the event rates shown in Fig. 21 as a function of m_D for different lepton masses m_L assuming $m_X = 83$ GeV and 10 days of running at $L = 10^{31}$ cm^{-2}s^{-1}; 200 pb^{-1} would probe up to $m_L + m_D \approx 220$ GeV.

4.6 Leptoquarks

Technicolour offers an alternative though not undisputed explanation for the Higgs mechanism. In this theory the Higgs is a pion-like composite: a state where a new quark and antiquark are bound together by the super strong technicolour force. Besides new quarks U,D,... new leptons E,M,... are also predicted which together lead to a new universe of particles. What is most exciting for HERA is the occurrence of leptoquarks TLQ = $\bar{u}$E,... The expected mass hierarchy is as follows:

	mass
- technipions (U$\bar{D}$,...)	0(10 GeV)
- leptoquarks (U$\bar{E}$,...)	0(160 GeV)
- technicolour Octets (U$\bar{D}$,...)	0(240 GeV)

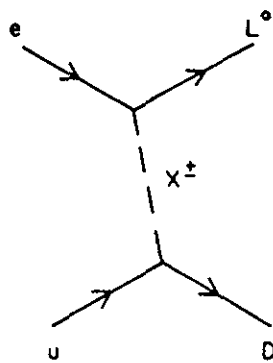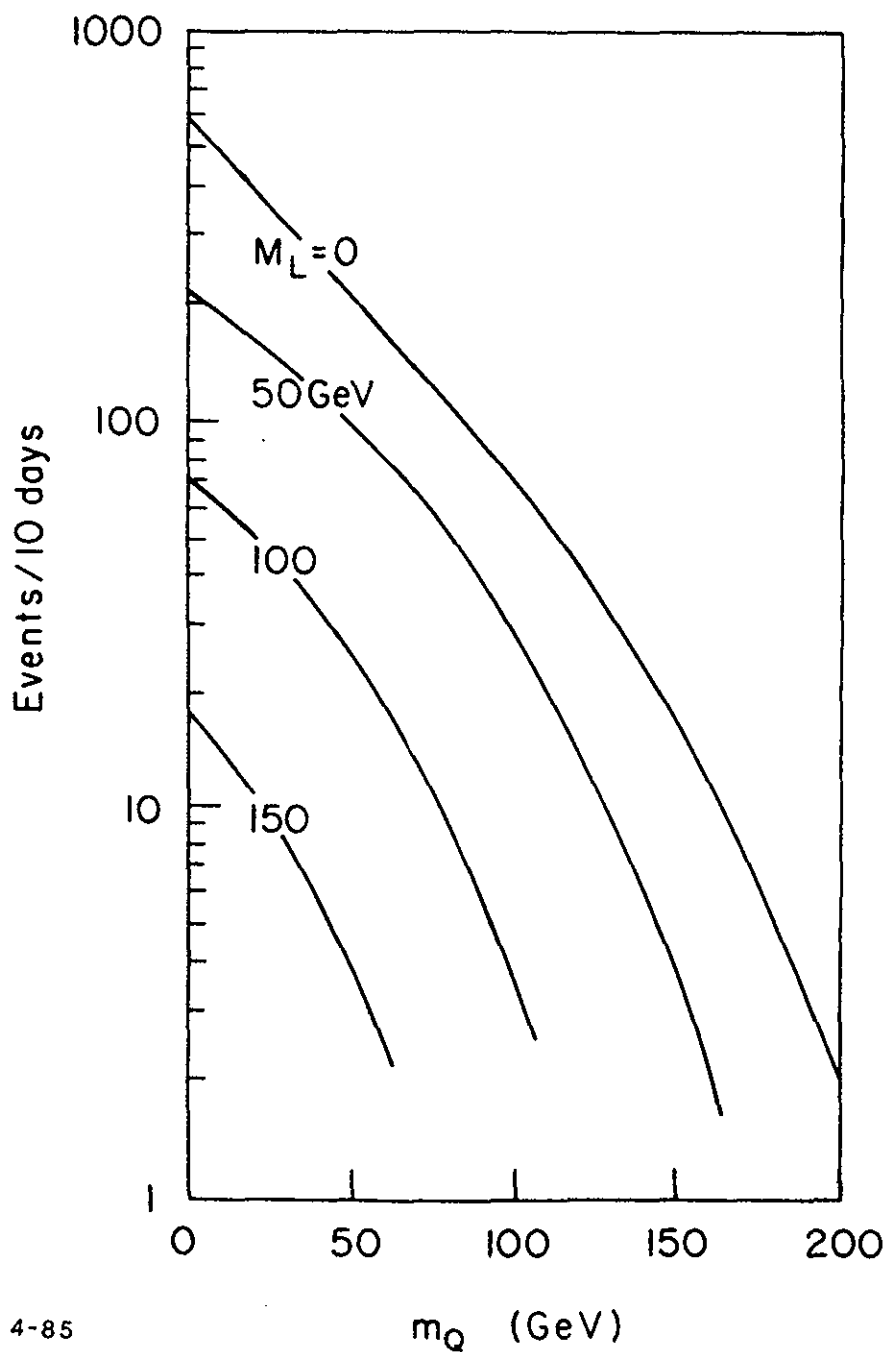Fig. 20   Diagram for new quark and lepton production.

4-85

39805

Fig. 21   Production rates for $e^-p \to DL^oX$.

Leptoquarks would be within the reach of HERA experiments. The diagrams expected to dominate the production are given in Fig. 22. The cross section for ep $\rightarrow$ TLQX is shown in Fig. 23 as calculated by[23]. Here Θ_{et} is the mixing angle. Given a $\sin^2\Theta_{et}$ of ~0.05 leptoquarks with masses up to 180 GeV can be studied at HERA (Fig. 23).

Technicolour theories already have difficulties explaining the small $K_L^0 \rightarrow \mu^+\mu^-$ branching ratio, and no evidence has been found at PETRA or PEP for low-lying technipions.

4.7. Supersymmetric Particles

HERA is a hunter's paradise for supersymmetric particles - if they exist in the accessible mass range. The prototype reaction is associated production of squark $(\tilde{q})$ and and slepton $(\tilde{\ell})$ by photino $(\tilde{\gamma})$, zino $(\tilde{Z})$ or wino $(\tilde{W})$ exchange (Fig. 24). The cross section has been calculated in Ref. 24. Figure 25 shows the cross section as a function of the squark mass for different slepton mass values. If we demand at least 10 events per 200 pb^{-1} then squark plus slepton production can be studied up to mass values of $m_{\tilde{q}} + m_{\tilde{e}} = 160$ GeV.

The production of scalar leptons has been studied in Ref. 20. The dependence on the $e^{\pm}$ polarization has been analyzed in Ref. 25.

5. DETECTION OF NEW PROCESSES

The mass range that is accessible to HERA for new particles was estimated in the previous sections by requiring the production of at least a few tens of these events a year. Since the yield of standard neutral and charged current events is many orders of magnitude larger one might wonder whether their detection will be as difficult as e.g. that of the top quark at the $S\bar{p}pS$ collider.

The events should be visible if the dominating background is ordinary neutral current scattering (eq $\rightarrow$ eq). This is a consequence of two facts: the kinematics in eq $\rightarrow$ eq is well defined, and, the decay of
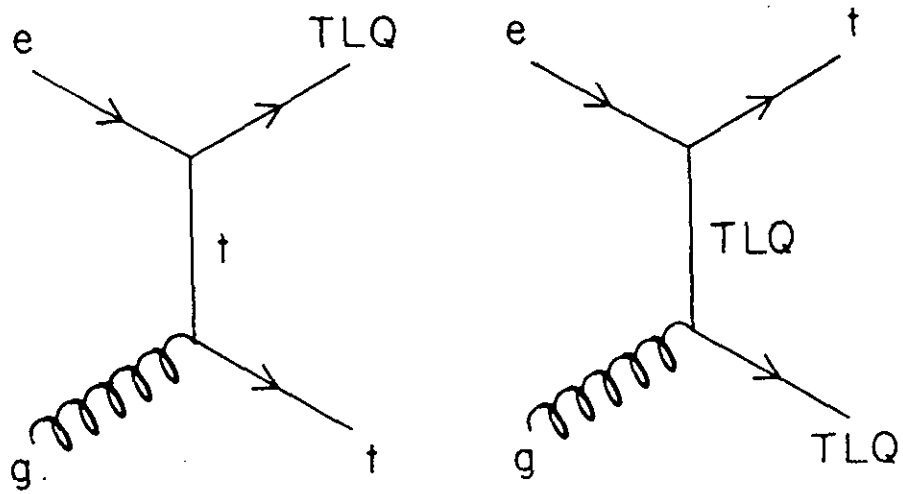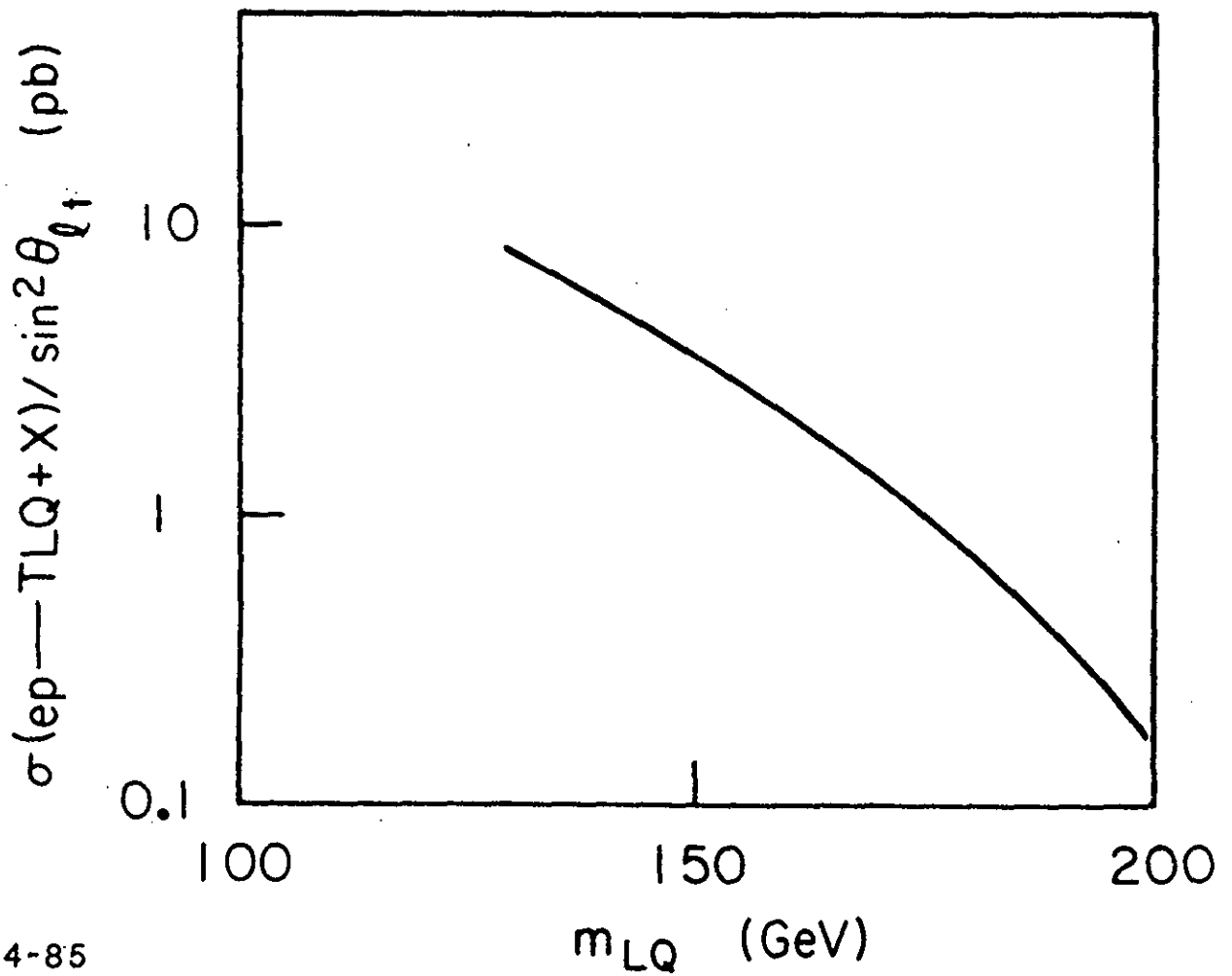
Fig. 22   Diagrams for the production of leptoquarks.

4-85

39799

Fig. 23   Cross section for the production of leptoquarks.

Fig. 24 Diagram for eq → eq.

4-85   39804
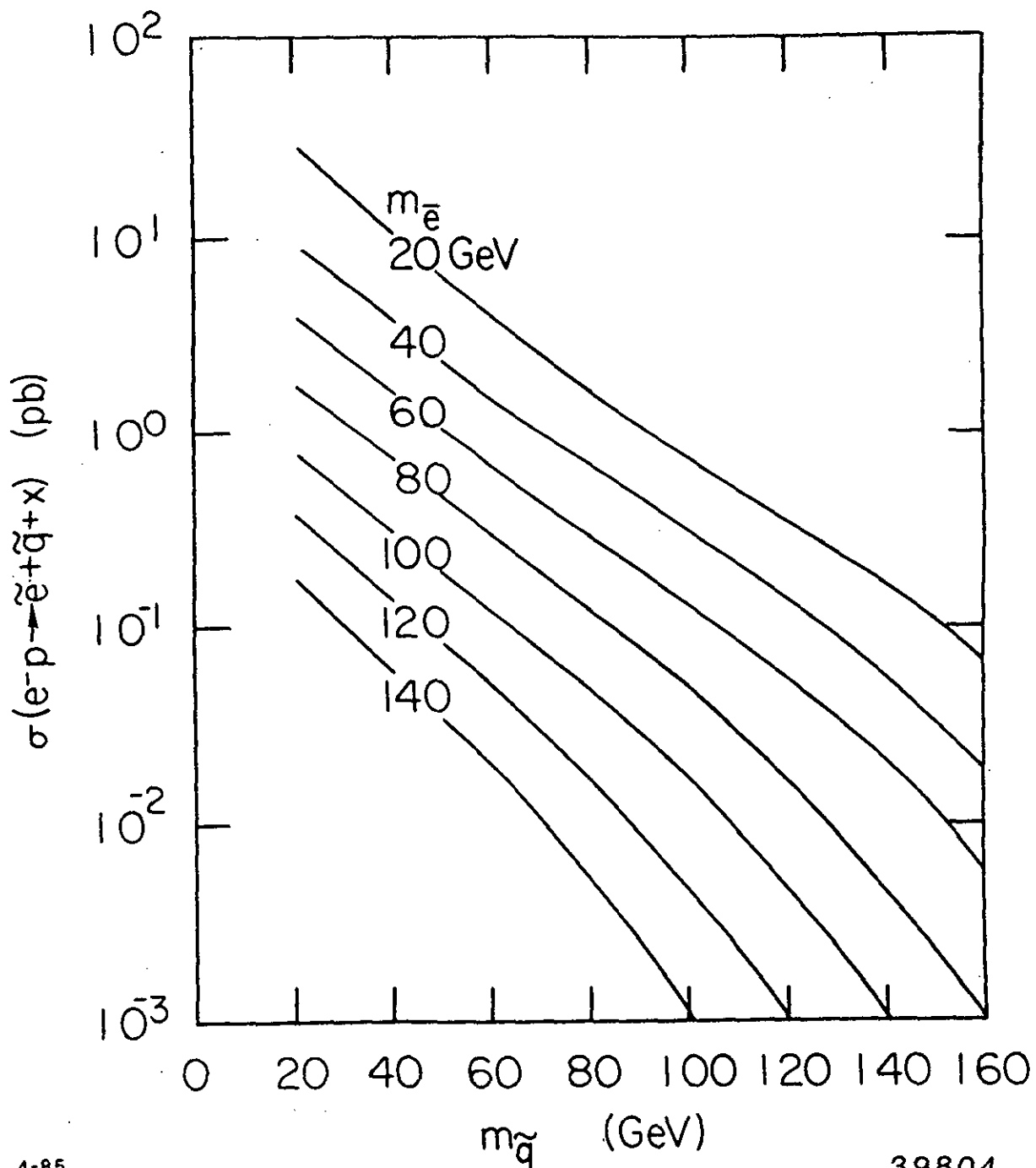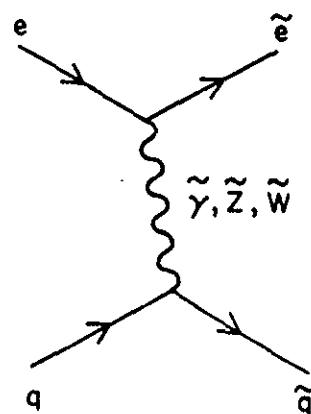
Fig. 25 Cross section for the production of supersymmetric quarks and
leptons.

a new heavy object will spread the emerging quark (lepton) over a large volume in phase space. For definiteness consider the supersymmetric reaction discussed before,

$$eq \to \tilde{e}\tilde{q}$$

The event rate relative to the standard neutral current reaction, eq → eq, is

$$\text{for } M_{\tilde{q}} + M_{\tilde{e}} = \begin{cases} 80 \text{ GeV} \\ 180 \text{ GeV} \end{cases} \quad \frac{\sigma(\tilde{e}\tilde{q})}{(eq)} \approx \begin{cases} 10^{-3} \\ 10^{-5} \end{cases}$$

The expected decay chains for $\tilde{q}$ and $\tilde{e}$ are

$$\tilde{q} \to q + \tilde{\gamma}$$

and

$$\tilde{q} \to q + \tilde{g} \to qg\tilde{G}$$

and

$$\tilde{e} \to e + \tilde{\gamma} \text{ or } \tilde{e} \to e + \tilde{G} \ .$$

Under the assumption that $\tilde{\gamma}$ and $\tilde{G}$ are weakly interacting and leave the experiment undetected the final state consists of an electron and a quark jet as in the case of an ordinary neutral current event. The difference lies in the kinematics as seen in the plane perpendicular to the beams. This is illustrated in Fig. 26.

In the standard case the electron and the quark jet are anti-collinear and balance each other in transverse momentum. For the super-symetric process e and q are neither anticollinear nor do they balance each other in transverse momentum. These two facts can be used to suppress the background. How efficiently that suppression can be done is demonstrated in Fig. 27. Here the acollinearity angle $\Delta\varphi$ is plotted versus Δy which measures the difference in y values computed from the current jet and the scattered electron:

$$\Delta_y = y_q - y_e$$

$$y_q = \frac{\Sigma E_i - P_{\parallel i}}{2E_e}$$

$$y_e = \frac{E_e' - P_{\parallel e}'}{2E_e}$$

$E_i, P_{\parallel i}$ are the energies and longitudinal momentum components of the current jet particles; $E'_e, p'_{\parallel}$ are the energy and longitudinal momentum component (measured w.r.t. the incoming proton direction) of the scattered electron.

The distributions shown in Fig. 27 have been computed by a Monte Carlo technique for a reasonably realistic detector assuming a finite hadronic energy resolution ($\Delta E/E = 60 \%/\sqrt{E}$) and a blind angular region around the beam pipe. Fig. 27(c) shows the result for $\sim 10^4$ standard neutral current events. As expected, the standard NC events cluster near $\Delta\varphi = \Delta y = 0$. In contrast, for the supersymmetric process (shown in Fig. 27(a) for $m_{\tilde{q}} = m_{\tilde{e}} = 40$ GeV and in Fig. 27(b) for $m_{\tilde{q}} = m_{\tilde{e}} = 100$ GeV). The events are spread all over the $\Delta\varphi, \Delta y$ map. Thus, supersymmetric events can be well isolated from the standard ones without significant loss in efficiency.

Fig. 26 Comparison of the kinematics

for eq → eq

and for

eq → ẽq̃ → eq + missing particles
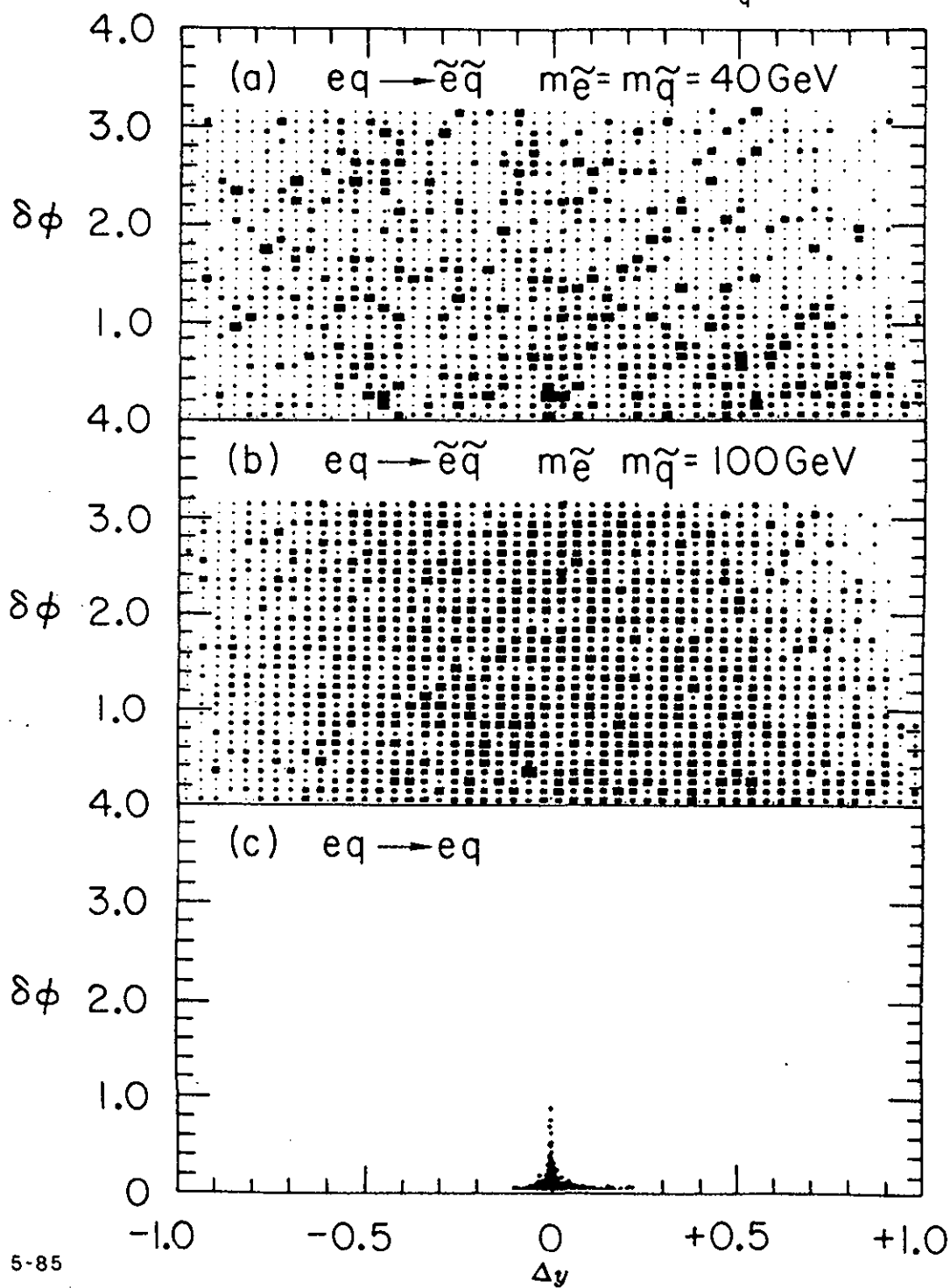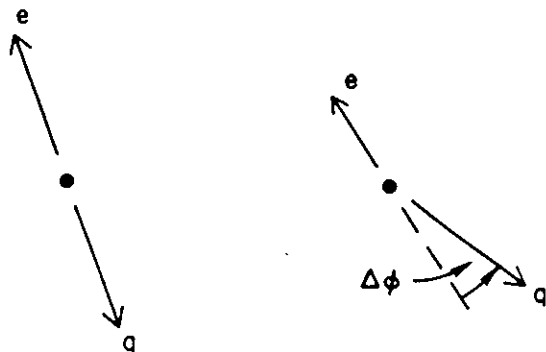
Fig. 27 Distribution of $\Delta\varphi$ versus Δy for the supersymmetric process eq → ẽq̃ with $m_{\tilde{e}} = m_{\tilde{q}} = 40$ GeV (a) and $m_{\tilde{e}} = m_{\tilde{q}} = 100$ GeV (b) and for the standard process eq → eq (c).

39803

6. THE HERA COLLIDER

The layout of HERA is shown in Fig. 28 (Ref. 26). Two separate magnet systems guide the e^- and p beams around the 6.3 km long ring. The beams cross each other in four interaction points. The salient machine parameters are listed in Table 2.

Table 2:   Parameters of HERA

	p-ring	e-ring	units
Nominal energy	820	30	GeV
c.m. energy	314		GeV
Q^2_{max}	98.400		GeV^2
Luminosity	$1.5 \cdot 10^{31}$		$cm^2 s^{-1}$
Polarization time		25	min
Number of interaction points	4		
Crossing angle	0		
Free space for experiments	±5.5		m
Circumference	6336		m
Bending radius	588	608	m
Magnetic field	4.65	0.165	T
Energy range	300-820	10-33	GeV
Injection energy	40	14	GeV
Circulating current	163	58	mA
Total number of particles	$2.1 \cdot 10^{13}$	$0.8 \cdot 10^{13}$	
Number of bunches	210		
Number of bunch buckets	220		
Time between crossings	96		ns
Beta function (β^*_x / β^*_y)	10/1.0	2/0.7	m
Beam size at crossing σ_x	0.29	0.26	mm
Beam size at crossing σ_y	0.07	0.070	mm
Beam size at crossing σ_z	11	0.8	cm
Energy loss / turn	$1.4 \cdot 10^{-10}$	127	MeV
Max. circumf. voltage	0.2/2.4	260	MV
Total RF power	1	13.2	MW
RF frequency	52.033/208.13	499.667	MHz
Filling time	20	15	min
Tune shift Q_x	0.001	0.016	
Tune shift Q_y	0.00042	0.025	

Hall
North

360m

R=797m

Hall
East

360m

HERA

e

p

Hall
West

40 GeV
protons

p

e

30 GeV
electrons

820 GeV
protons

PETRA

14 GeV
electrons

Hall
South

38444
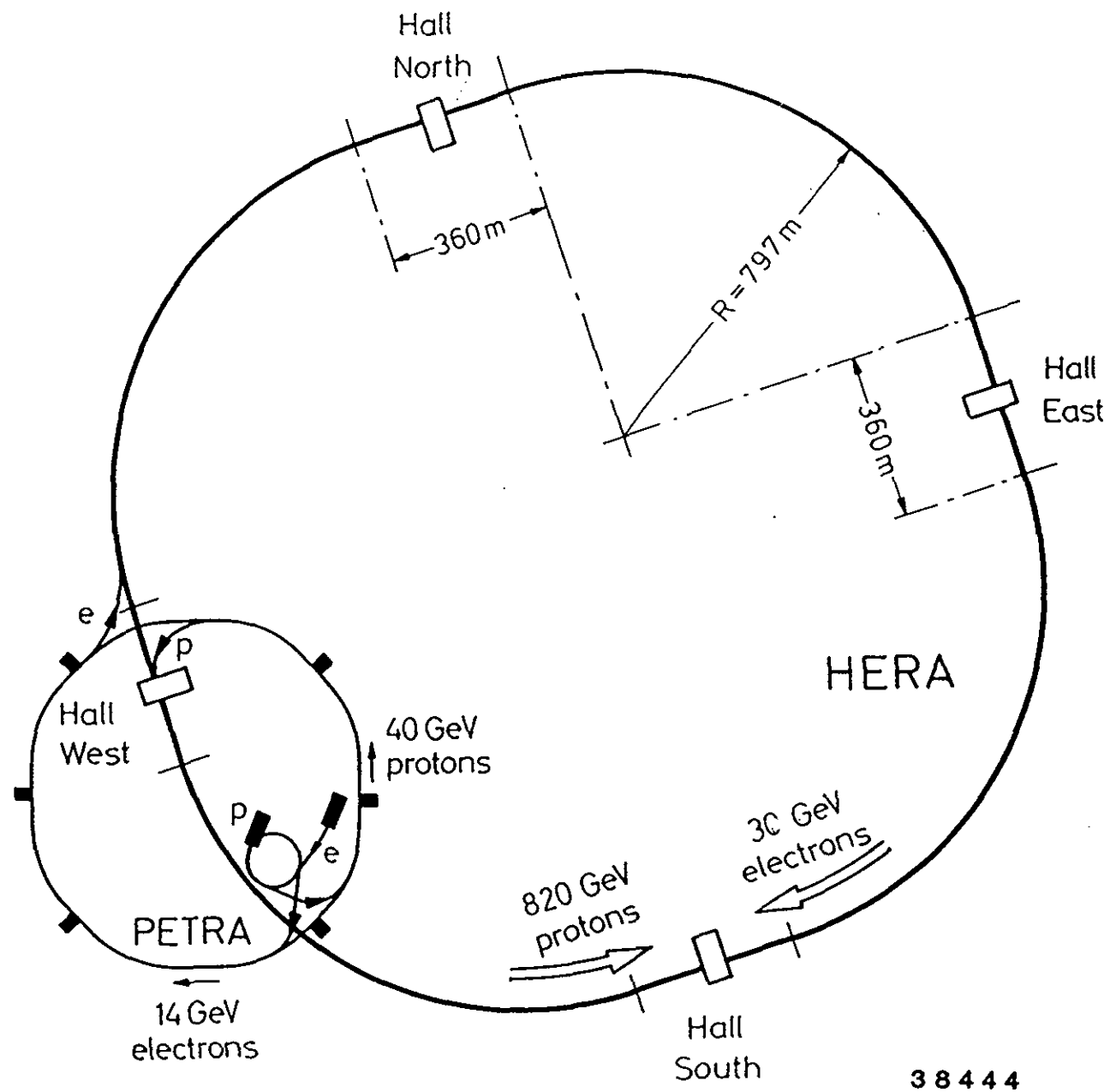
Fig. 28 Layout of HERA.

6.1   Civil Engineering

The machine houses in a tunnel that is between 15 and 20 m deep underground (Fig. 29). The tunnel is in a plane which is tilted by ~1 % w.r.t. to the vertical. About one half of the tunnel is below the water table. Most of the tunnel runs underneath public land; the stretch where HERA intersects PETRA is on DESY property. As a consequence, most of the installations for cryogenics, electrical and cooling power etc. are located on the DESY site and feed the rings through Hall West while the surface activities near the other halls - which are on public land - are restricted so as to keep the disturbance of the environment there at a minimum.

A cross section of the tunnel is shown in Fig. 30. It has an inner diameter of 5.2 m. The proton ring is located above the electron ring. Fig. 30 also indicates the supply lines for liquid and gaseous Helium and for cooling water.

HALLE WEST HALLE NORD HALLE OST

+50
+40
+30 VERBINDUNG
      PETRA
+20
+10
± 0

0+000   M 1:5000   3+166

M 1:500

HALLE OST HALLE SÜD HALLE WEST

+50
+40   PETRA
+30
+20
+10   ∅5,00m   ∅3,20m
± 0

3+166   RINGUMFANG IN Km+m   4+750   6+332

HÖHE NN + m

39832

Fig. 29 The HERA tunnel.

HERA
Bogenbereich   37410

Fig. 30 Cross section of the HERA tunnel.

6.2 Injection System

The *injection system* uses the rebuilt synchrotron DESY and the storage ring PETRA (Fig. 31). H^- ions are accelerated to 50 MeV in a newly constructed LINAC, to 7.5 GeV in the new synchrotron, DESYIII, to 40 GeV in PETRA (which requires bypasses around the RF cavities for the $e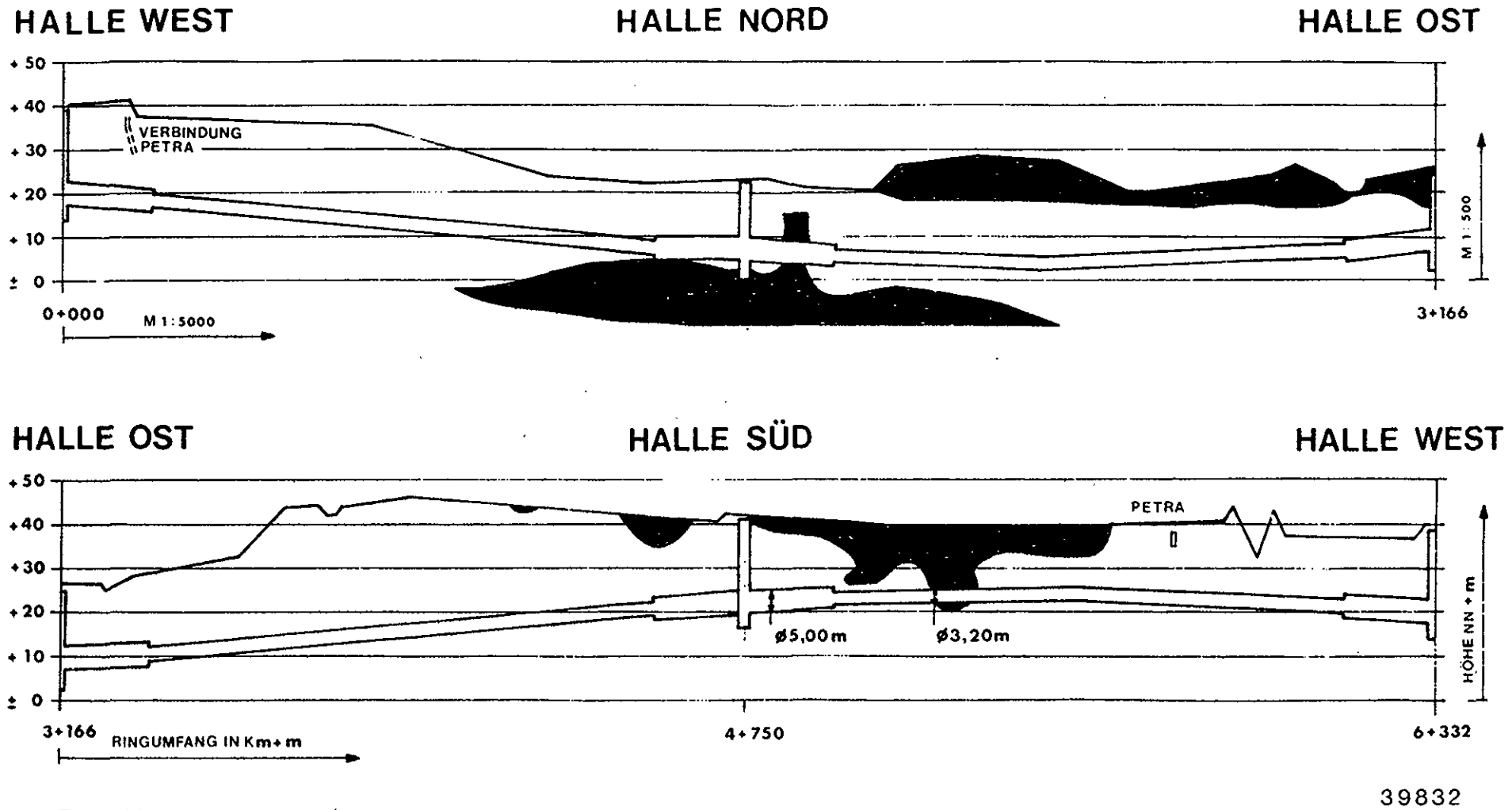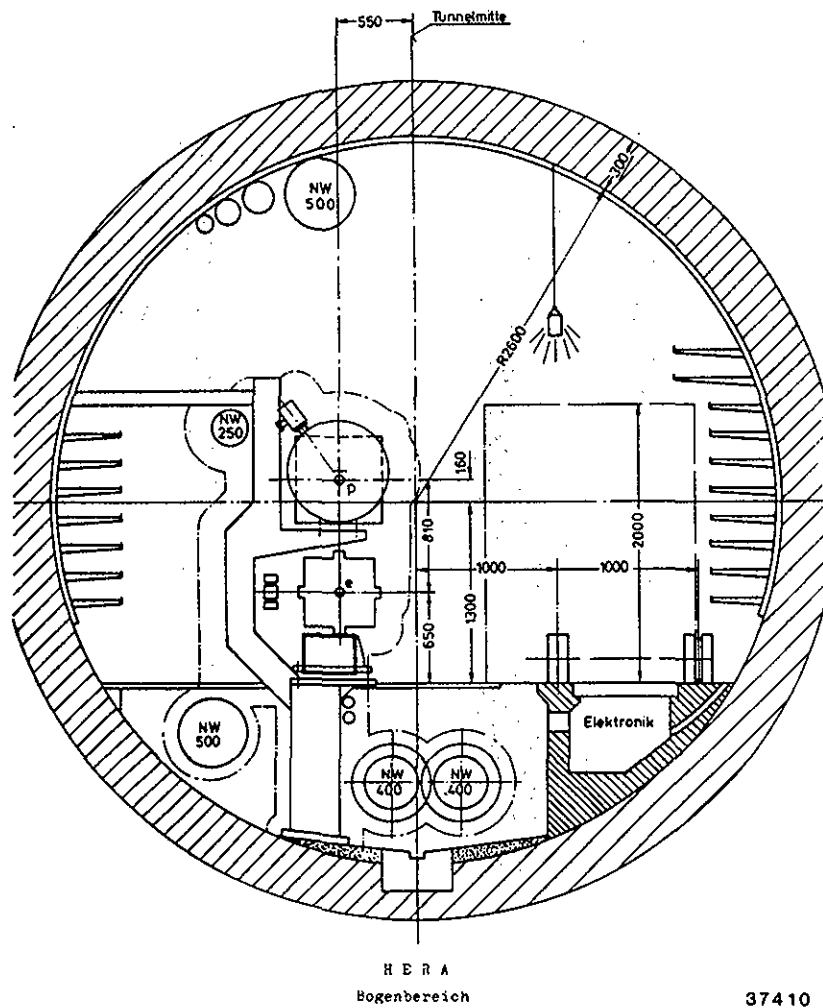^{\pm}$ beams) and injected into HERA. Electrons pass from a LINAC (50 - 400 MeV) to the newly constructed synchrotron DESY II (9 GeV), to PETRA (14 GeV) and finally to HERA. The filling takes for each beam between 15 and 20 min.

6.3 Electron Ring

At 30 GeV a bending field of 0.165 T is required. This can be achieved with conventional magnets. In Fig. 32 a half cell of the magnet system is shown. Dipole, quadrupole and sextupole are premounted on one common support, the total length of a half cell being 11.8 m. Figure 32 also shows cross sections for the three different types of magnets. The dipole magnet is excited by a single conductor which carries at 30 GeV a current of 6767 A.

6.4 Proton Ring

The technological challenge of HERA lies in the superconducting magnet system for the proton beam. A bending field of 4.65 T is required to keep an 820 GeV proton beam on orbit. At this field strength iron cannot be used for field shaping and homogeneity has to be achieved by proper shaping of the superconducting coils. Figure 33a,b indicates schematically the manner in which the windings are wrapped around the beam pipe. In order to obtain a homogeneous field the current density has to follow a $\cos\varphi$ distribution, $I = I_o \cos\varphi$.

The mechanical accuracy required is quite demanding. Consider the case where the height of the left coil halves is larger by 2δ and that of the right coil halves is shorter by 2δ (Fig. 33c). If $\delta = 20$ μm, the skew quadrupole component is $a_2 = 1.7 \cdot 10^{-4}$ which is at the tolerable limit. Hence, a mechanical precision of typically 20 μm has to be kept.

HERA Injection Scheme

HERA
p = 820 GeV
e+ = 30 GeV

e+
e- } = 30 GeV

PETRA Halls N

PETRA Hall NE

PETRA Hall NW

p,e+

HERA Hall West

Cryo-Technic Hall

Magnet Test Hall

e-,e+

p,e+
p = 40 GeV

Positron Linac

PETRA Hall E

PIA

PETRA Hall W

e-,e+

DESY II

p,e+

DESY III

DESY II

e+ 450 MeV

Electron Linac
220 MeV

PETRA

H- Linac
50 MeV

e-, e+
7 GeV

p
7 GeV

HERA

PETRA Hall SW

PETRA Hall SE

Proton bypass

38596
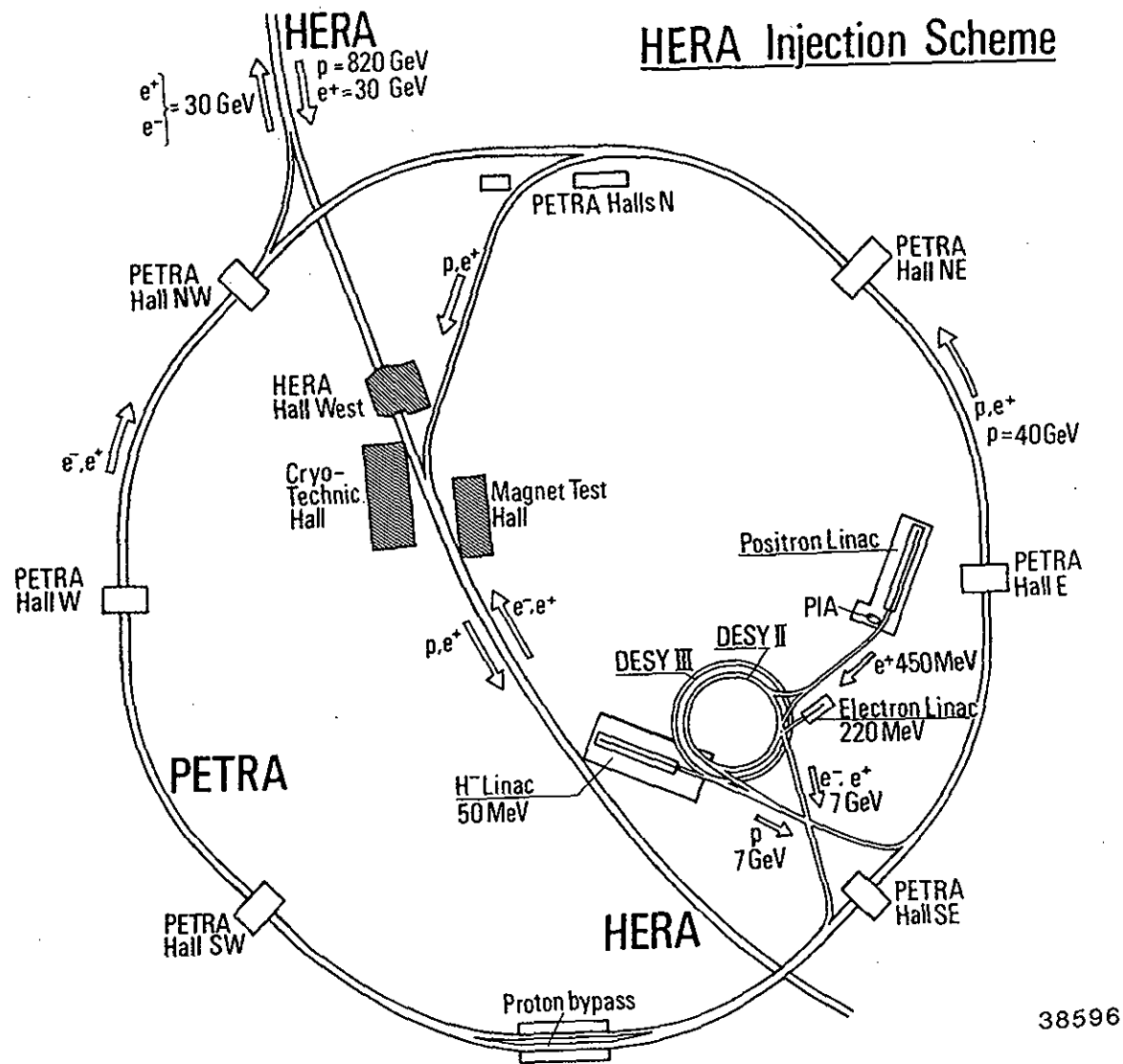
Fig. 31 The injection system for HERA.

Correction Dipole

Quadrupole Magnet

Correction Dipole

Key plate

S1 D S2

Sextupole Magnets

e⁻-Dipole Magnet

Quadrupole Magnet Sextupole

- 45 -

Quadrupole Magnet

rein forcing angle
Iron yoke
Copper coil
Separating plane

Cross section Sextupole Magnet

cooling water tube
Iron yoke
Coil
Separating plane

Cross section e⁻-Dipole Magnet

rein forcing girder
Iron yoke
Vacuum chamber
Distributed vacuum pump
Local joint between yoke and girder
Insulation
Al-conductor
Cooling channel
Electron beam Water cooled radiation absorber
Key plate
315mm
380mm
380mm

TECHNICAL DATA at 30 GeV

field gradient	0.1314 T/cm
bore diameter	74 mm
conductor (copper)	13.3×13.3 mm^2
hole diameter	5.7 mm
turns per coil	20
current	358 A
power	2.73 kW
mass	1020 kg

TECHNICAL DATA at 30 GeV

Sextupole strength	0.0409 T/cm^2
bore diameter	96 mm
conductor ribbon (copper)	28×0.5 mm^2
turns per coil	138
current	45 A
power (620 mm long magnet)	3.5 kW
mass (620 mm long magnet)	550 kg

TECHNICAL DATA at 30 GeV

Field strength	0.1638 T
Bending radius	610.4 m
Gapheight	51.5 mm
Good field cross-section	40×80 mm^2
Conductor (aluminum)	100 cm^2
Number of turns in coil	1
Current	6767 A
Power	2.57 kW
Mass (including girder for quadrupole and sextupole	4200 kg

40005

Fig. 32 A half cell of the electron ring.

a)

$\vec{B}$

beam

b)

$I = I_0 \cos \varphi$

φ

$\odot$ $\otimes$

c)

δ δ

δ δ

d)

$-I$ $+I$

F_{nor} F_{nor}
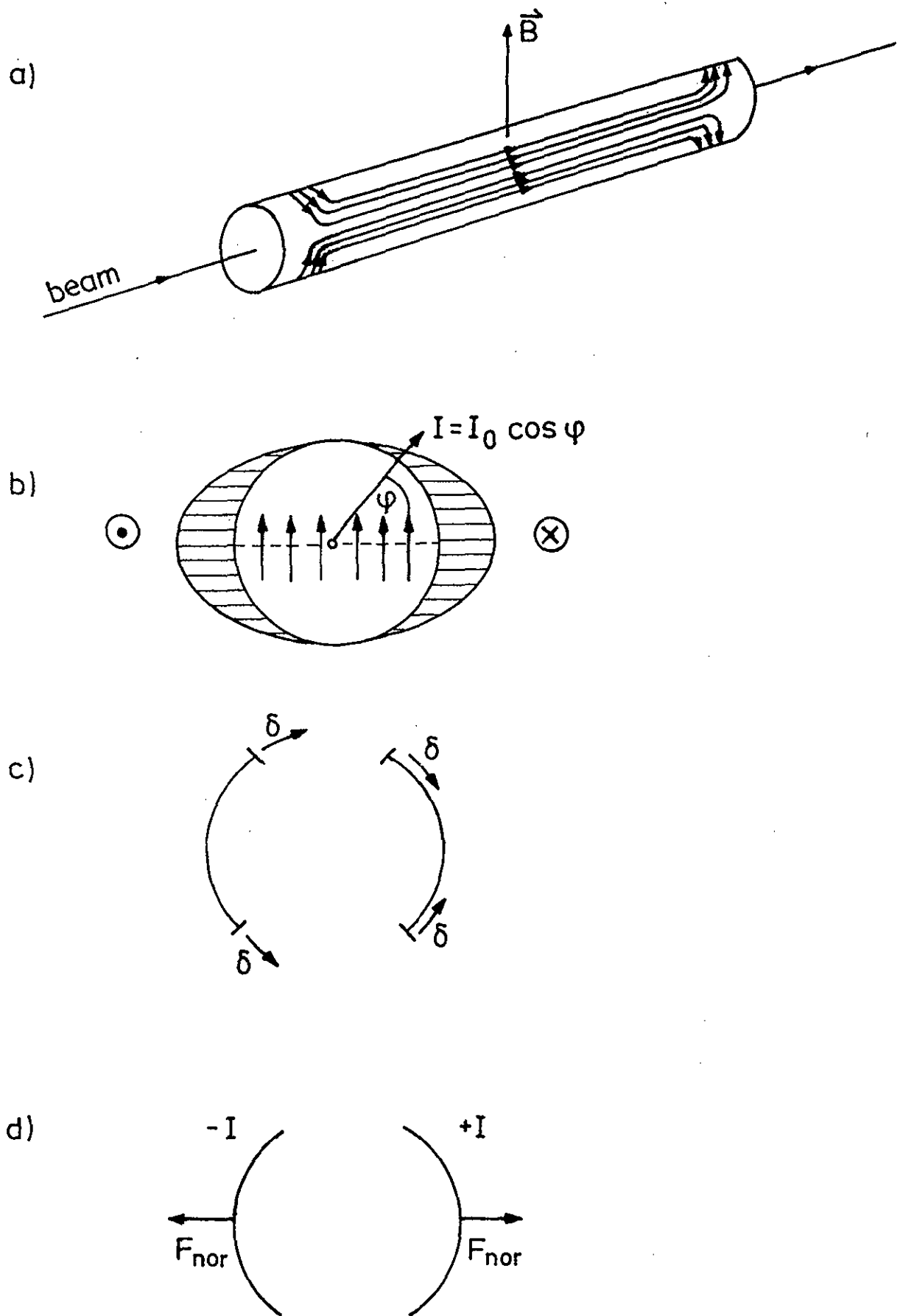
40013

Fig. 33 The mechanics of a superconducting dipole.

It has to be kept in the presence of a magnetic pressure which tries to push the two coil halves apart with a force of ~100 t per meter (Fig. 33d).

The design of the HERA magnets has started from the FNAL-TEVATRON and BNL magnets and has lead to a novel concept shown in Fig. 34a. The coils are clamped by aluminum collars. The collaring is reinforced by the cold iron yoke which surrounds the collar tightly. Vacuum and superinsulation shield the iron yoke from the ambient temperature. The dipole magnet has an overall length of 9 m.

In Fig. 34b the load line measured for dipole Nr. 3 is shown. At 4.6 K the quench occurred at 5.8 T which is about 25 % higher than the field required for 820 GeV.

The advantages over a warm iron design are a 12 % gain in field, a smaller static heat load at 4 K and better quench protection. The disadvantage is a 5 times larger cold mass; however, the cooldown-warmup cycle takes the same amount of time in both cases, about 30 - 40 h.

A schematic drawing of a proton ring cell with the dipole, quadrupole and correction magnets is shown in Fig. 35. The length of one cell is 47.08 m.

6.5 RF System

6.5.1 Electron ring

The circulating electrons of energy E loose energy by synchrotron radiation:

$$\Delta E/turn = \frac{0.088 \ E^4}{\rho}$$

where ρ is the bending radius in m, ρ = 608 m. For E = 30 GeV, ΔE = 112 MeV/turn. For an electron current of 58 mA the power lost by synchrotron radiation is 6.5 MW. The power loss is compensated by RF which is fed into cavities that are traversed by the electron beam.

The frequency chosen for the RF of HERA is 500 MHz, which is the same as for DESY, DORIS and PETRA (see Table 2). For operation below 30 GeV HERA will be equipped with cavities formerly used at PETRA. There is, however, a strong physics desire to run the electron beam at
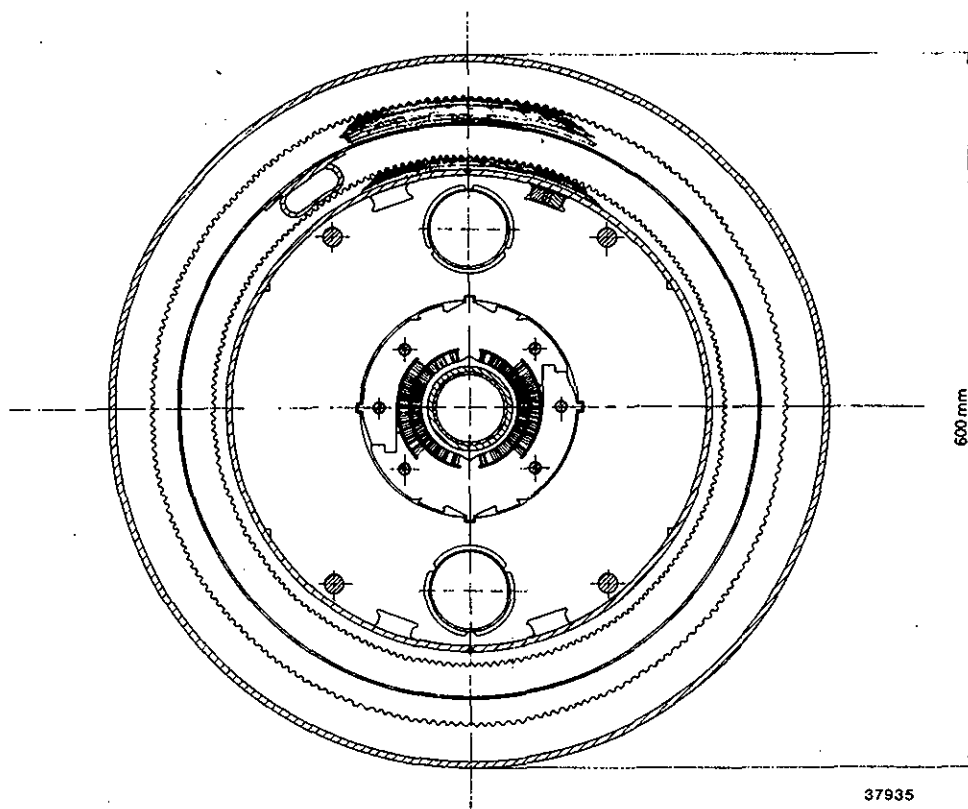
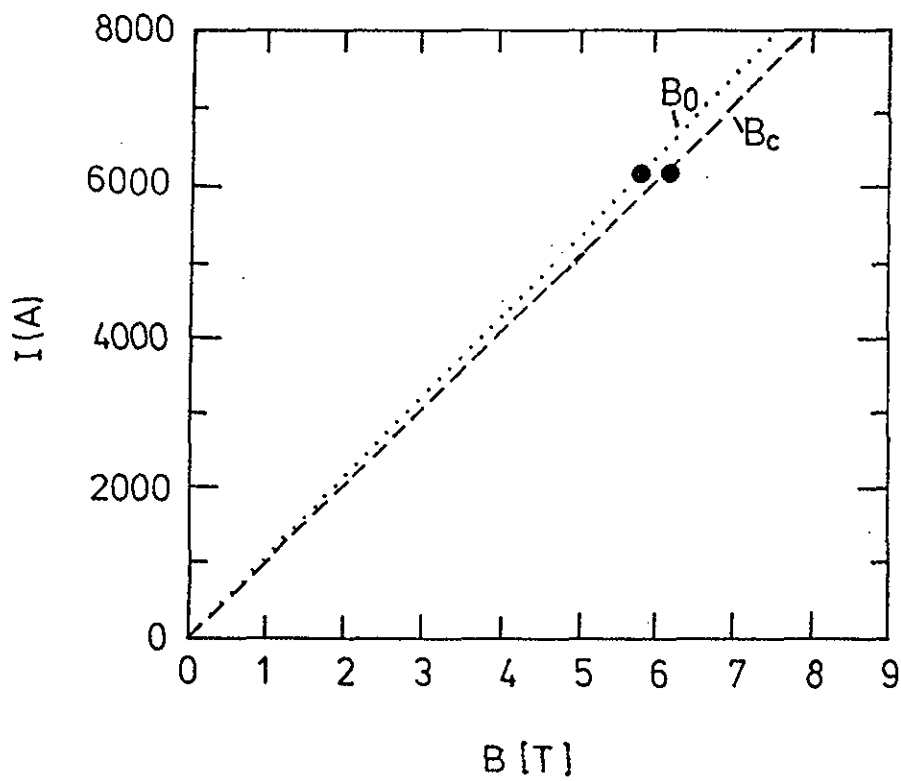Fig. 34a   Cross section of the superconducting dipole.

Fig. 34b   Load line for dipole Nr. 3. B_o field on axis, B_c maximum field
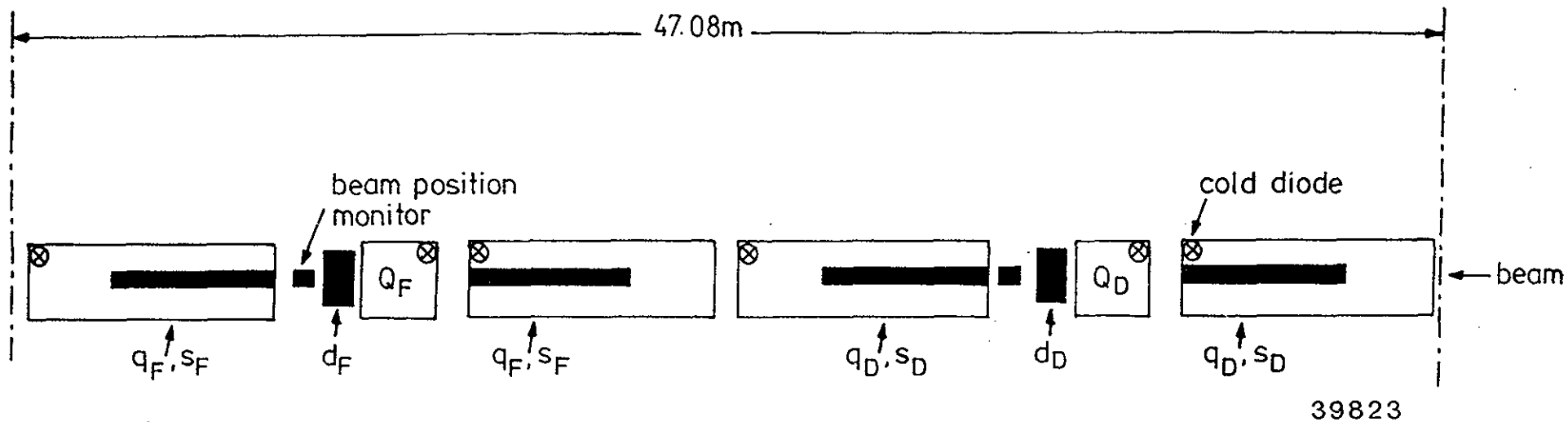at conductor, at 4.6K (S. Wolff, priv. comm.).

Fig. 35   Sketch of a cell of the proton ring with four dipoles plus quadrupole (q) and
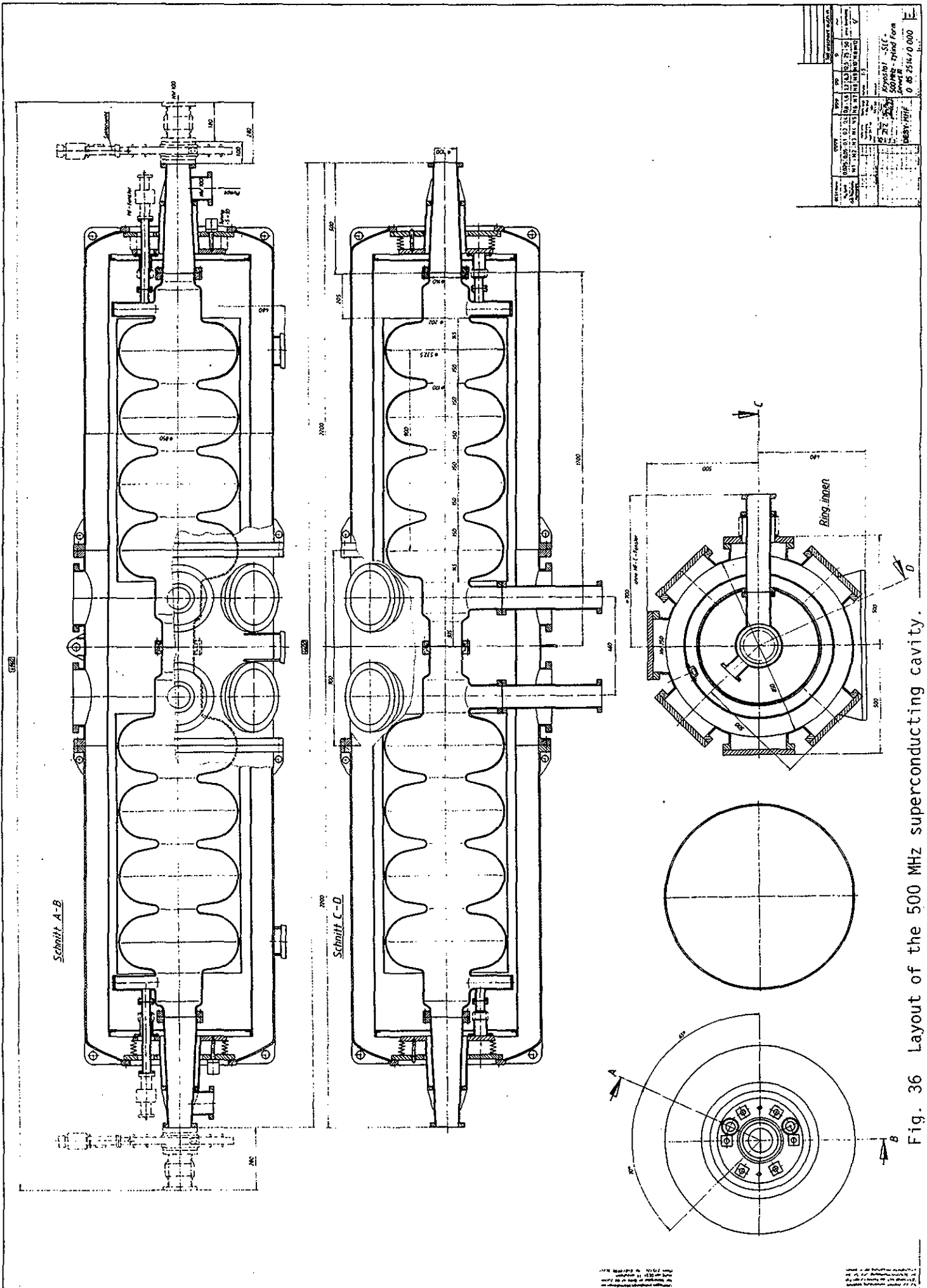sextupole (s) correction coils, and two quadrupoles (Q).

Fig. 36   Layout of the 500 MHz superconducting cavity.

somewhat higher energy: at E = 27 GeV the polarization time (see sect. 6.6) is 43 min compared to 12 min at E = 35 GeV.

In order to reach 35 GeV it is planned to add superconducting cavities (see Table 3). Superconducting 500 MHz cavities are under development at DESY (Fig. 36). With a 2 x 4 cell cavity in a single cryostat an accelerating field of 12 MV or a gradient of 5 MV/m is expected. About 240 kW/cryostat are fed to the beam. The expected heat loss is 85 W/cryostat at 4K and 5 MV/m.

In a prototype test a 1 GHz 9 cell superconducting cavity with 2.7 MV/m has been installed in PETRA. It has been run for 5 months in normal operation with very encouraging results.[27]

Table 4: RF for the electron ring.
          A total available RF power of 7 MW is assumed.

number of normal c.cavities	number of super c.cavities	E (GeV)	max I (mA)	polarization time (min)
88	-	27	46	42
88	-	29	11	30
88	8	30	27	25
-	32	35	30	12

6:5.2 Proton ring

The loss of synchrotron radiation by the proton beam is negligible (remember $\Delta E \sim mass^{-4}$). For the proton beam new cavities and clystrons have to be developed. The frequency of the RF will vary from 52 MHz at injection (40 GeV) to 208 MHz at 820 GeV.

6.6 Electron Polarization

After coasting for some time the electrons will become polarized transverse to the ring plane (Fig. 37a). The build-up time for polarization follows from the relation
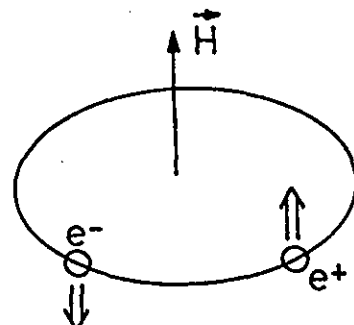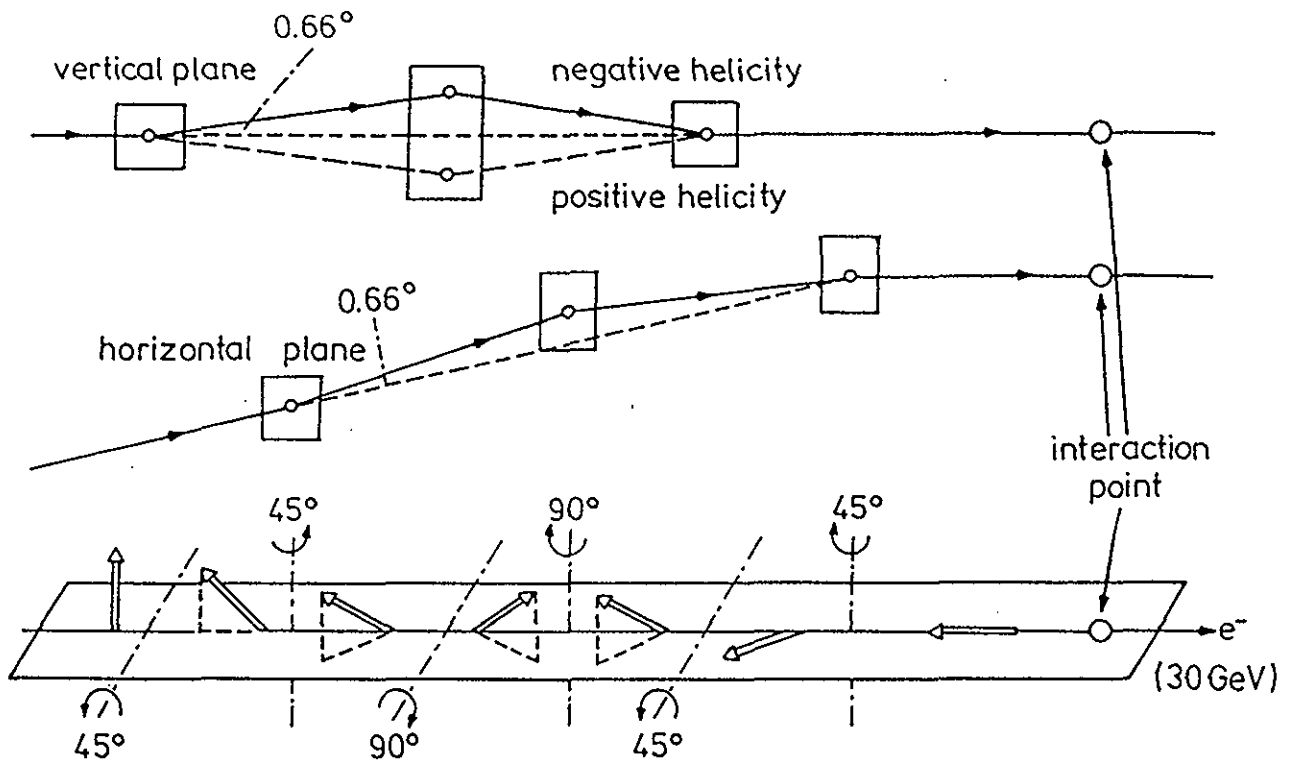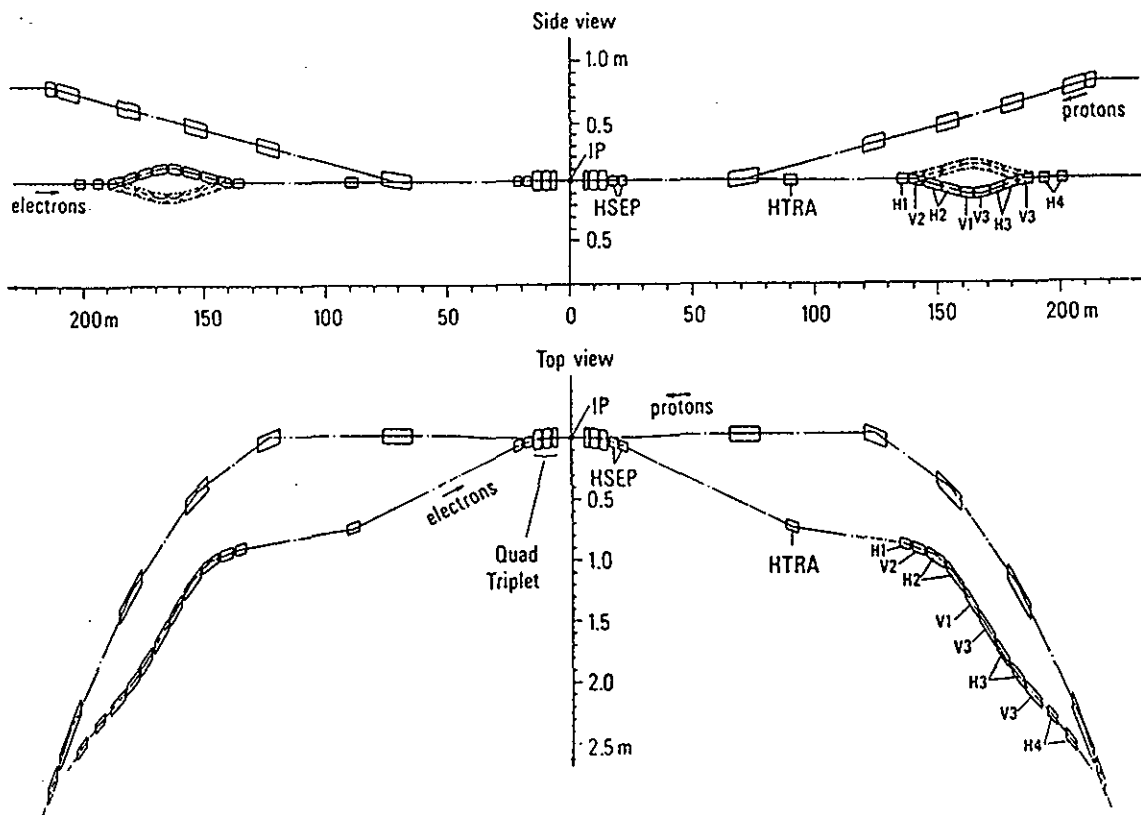
Fig. 37a Transversely polarized $e^{\pm}$ beams.

Fig. 37b Spinrotator.

39822

Fig. 38a Layout near the interaction region with spin rotators and zero crossing angle geometry.

$$P(t) = P_o \ (1 - e^{-t/\tau_p},$$

with $\quad\quad P_o = 92 \ \%$

and

$$\tau_p = \frac{98 \ \rho^2 \ R}{E^5}$$

where τ_p in s, ρ bending radius in m, R average radius in m and E in GeV. For E = 30 GeV, τ_p = 25 min.

For particle physics, instead of transverse polarization an electron beam of definite helicity is needed (see eg. sect. 3.5.5). This can be achieved in the following way. In the arcs the electrons remain transversely polarized. Shortly before reaching the interaction point the spin is rotated into the beam direction (or opposite to it) and as the beam leaves the interaction region the rotation is undone. Notice, that the two rotations have to be done with utmost precision since the build up time for polarization is O(1000s) during which the electrons pass $2 \cdot 10^8$ times the rotators. It is clear that a tiny misalignment can destroy the polarization. The spin rotator makes use of the difference between the frequencies for spin precession (ω_{Larmor}) and revolution ($\omega_{cyclotron}$) in a magnetic field which results from the anomalous magnetic moment of the electron:

$$\omega_{Larmor} - \omega_{cyclotron} = \gamma \ \frac{g-2}{2} \ \frac{e}{m} \ B$$

where γ = E/m, m electron mass. This leads to a spin rotation angle of

$$\Theta_{rot} = 0.001159 \ \gamma\varphi$$

where φ is the angle by which the electron direction is bent in the magnet.

Numerous design studies have been made to find the optimum spin rotator (Ref. 28). A spin rotator of the siberian snake type is shown in Fig. 38; V and H define vertically and horizontally bending magnets. The total length of the rotator is about 70 m. The maximum degree of longitudinal polarization is expected to be $P_L \approx 80 \ \%$.

6.7   Interaction Region

The interaction region was originally planned with a finite crossing angle (~20 mrad). When simulations showed that this will lead to beam blow-up via betatron oscillations (Ref. 29) a geometry with zero crossing angle (head-on collisions) was chosen. This necessitated the introduction of additional bending magnets close to the interaction point in order to bend the electron beam away from the proton beam ahead of the first proton ring magnet (see Fig. 38a). The necessary bending power is provided by three quadrupoles which also act as a low beta insertion. The bending of the electron beam produces a strong beam of synchrotron radiation (total power at 35 GeV: 9 KW with critical energy 80 keV, $8 \cdot 10^{17}$ photons/s with k > 20 keV) which passes through the interaction region (see Fig. 38b). For a safe operation the γ flux in a typical drift chamber at a distance of 15 cm from the interaction point should not exceed $\sim 10^{8}$ γ/s, k > 20 keV. This can be achieved by placing the beam pipe asymmetrically with respect to the beam axis so that the synchrotron radiation fan can pass unhindered and by installing suitable masks and collimators (Fig. 38b), see e.g. Ref. 7.
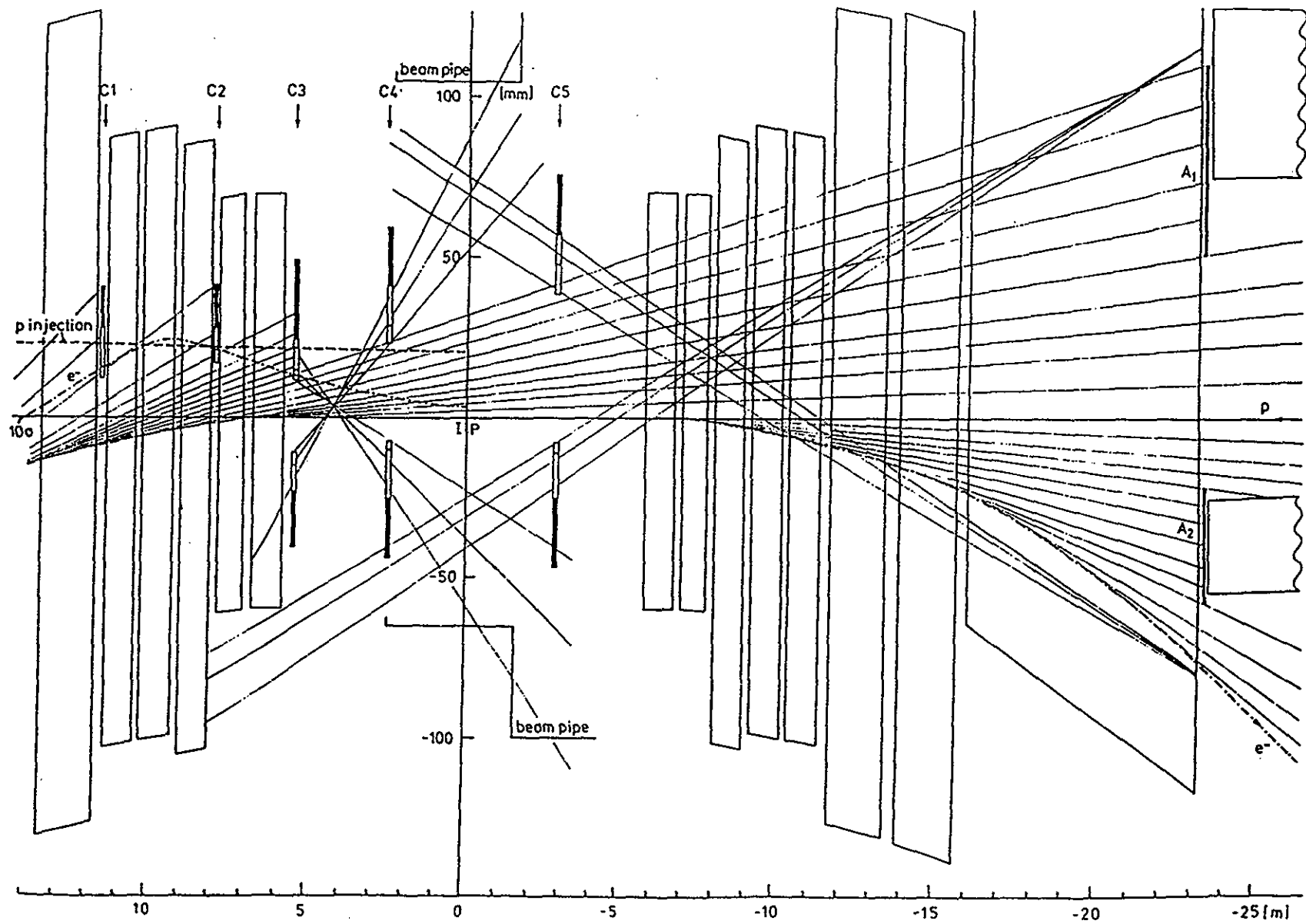
Fig. 38b   Arrangement of magnets and collimators (C_1, C_2,..) and synchrotron radiation absorbers (A_1, A_2) close to the interaction region.

6.8 Construction Schedule and Status of HERA

The schedule foreseen for the construction of HERA is given in Table 5.

Table 5: The HERA schedule

Authorization	4/1984
Start civil engineering	4/1984
DESY II assembled	1985
Delivery of first e⁻ series magnets	8/1986
Start installing machine components in tunnel	10/1986
DESY II operational	end 1986
Electron injection into first quadrant	4/1987
Commissioning of proton LINAC	4/1987
Delivery of last e⁻ magnet	9/1987
Civil engineering completed	12/1987
Commissioning of DESY III	12/1987
Refrigeration plant operational	3/1988
Proton injection into first quadrant	4/1988
Delivery of last superconducting magnet	10/1988
Commissioning of proton ring	6/1989
Electron-proton physics	1990

The status of the project as of June 1986 is as follows:

Buildings

tunnel   : one half of the tunnel is done; the quadrant South Hall to West Hall is ready.

halls   : South Hall and West Hall are nearly ready; the other two halls are under construction.

DESY II   : is being tested.

e⁻ ring   : series production of dipoles, quadrupoles, sextupoles has started.

H⁻ LINAC : all components have been ordered. The ion source works within specification.

p ring   : three 9 m long dipoles have been built and tested; the
quality of the field is good. They reach fields 25 % above
their nominal value. The quality of the field is well within
specification. Saclay has constructed two prototype quadru-
poles. They reach gradients well above the nominal value with
acceptable field quality. Production of the preseries of the
correction magnets has started in the Netherlands.

cryogenic plant: The components are being installed. The first of the
.three plants will start in October 1986.

6.9   Cost and Financing

The capital costs for HERA in 1981 prices are

General: site, buildings, power	260 MDM
Electron ring	112 MDM
Proton ring	282 MDM
Sum	654 MDM

The Federal Government of Germany and the city of Hamburg share the
financial burden in the ratio 9 : 1. However, 15 - 20 % of the expen-
ditures are paid by foreign contributions. These are from

Canada	: beam transport, proton RF
China	: staff
France	: development of the proton quadrupole and construction of a part of the quadrupoles
Israel	: currents leads for proton magnets
Italy	: half of all proton dipoles
Netherlands	: correction magnets for the proton ring
Poland	: staff and components
Switzerland	: prototype of the helium transfer line
UK	: technical help
USA	: test of the superconducting cables and cryogenic components.

7.   EXPERIMENTATION AT HERA

Construction of a good detector for HERA is a challenge. Table 6 lists the requirements for several classes of physics. Particles and jets with energies up to 820 GeV have to be measured with precision. The large momentum imbalance between incident protons and electrons and the nature of space like processes send most particles into a narrow cone around the proton direction (see Fig. 39). Thus the calorimeter has to achieve simultaneously hermeticity, energy resolution and segmentation in a way not yet realized in any existing experiment. The detector has also to cope with high particle densities and with a time distance between bunch crossings of only 96 ns.
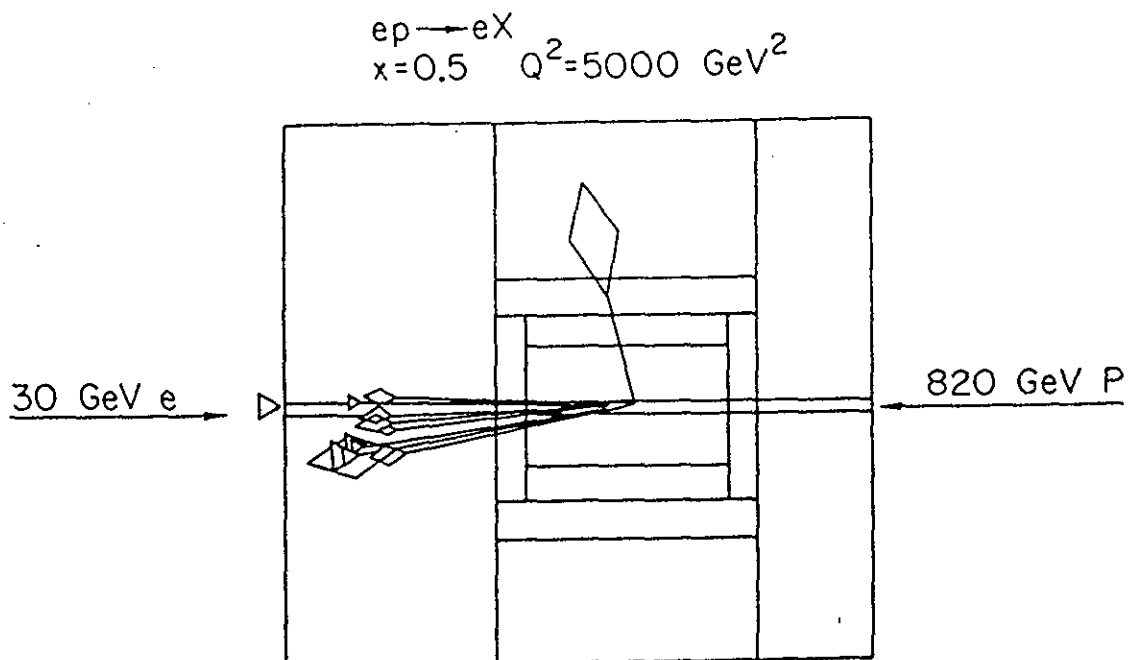
$$ep \longrightarrow eX$$
$$x = 0.5 \quad Q^2 = 5000 \ GeV^2$$

30 GeV e   820 GeV P

Fig. 39   Example of a neutral current event.

Table 6: HERA physics and detector requirements

topic	comments	requirements
• structure of proton, quark, e	• safe prediction of standard theory; look for deviations	• inclusive measurement of e for NC, current jet for NC,CC
	• reactions occur at parton level large $Q^2 \leq 40\ 000\ \mathrm{GeV}^2$ accessible	→ hermetic electromagnetic and hadronic calorimeters with uniform response to photons and hadrons, best possible hadron energy resolution
	• polarized $e^{\pm}_{L,R}$ provide excellent handle on preon structure and on new currents	→ precise measurement of E_{jet}, Θ_{jet}
• new particles t,LQ,e^*,q^*,N_R, SUSY	• mass range: up to 120-200 GeV	• measurement of jets, jet topology and missing p_T
	• very clean signatures	→ calorimetry as above
	• particles produced by CC alone are unique to HERA	• measurement of isolated e, μ and on jets → tracking detectors over full solid angle; excellent e,μ identification
• photoproduction	• c.m. energies up to 250 GeV attainable	→ forward electron tagging

7.1. Calorimetry

Good calorimetry will be vital for HERA experiments. For this reason we shall discuss the properties of calorimeters in some detail. For reasons of economy the calorimeter has to be of the sampling type pictured in Fig.40: it consists of absorber plates interleaved with detection layers to measure the electromagnetic and hadronic showers.

The energy resolution of a calorimeter results from a combination of different effects. Event-to-event fluctuations which determine the intrinsic resolution and sampling fluctuations usually dominate.

For <u>electromagnetic</u> showers the ultimate resolution is determined by the sampling fluctuations of the electromagnetic cascade, which are well understood and can be described by simulation programs such as EGS (Ref. 30). For a calorimeter made of high Z material (e.g. Pb, U), the energy resolution is

$$\sigma/E \approx 0.05 \ \frac{\sqrt{\Delta E(1 + 1/N_{pe})}}{\sqrt{E}}$$

where E is the incident electron energy in GeV, ΔE is the energy loss per layer in MeV and N_{pe} the number of electrons seen by the detector per minimum ionizing particle (mip) and layer. For instance, for 3.0 mm uranium plates, 2.5 mm scintillator and N_{pe} = 4 one finds

$$\sigma/E \approx \frac{14 \ \%}{\sqrt{E}}$$

The performance of a calorimeter for <u>hadrons</u> depends strongly on its relative responses to electrons and hadrons. This can be understood by considering a simple example. Assume a standard calorimeter with a response ratio of e/h = 1.4, and hadronic showers which consist only of $\pi^{\pm}$ and π^{0}. On the average the energy carried by $\pi^{\pm}$'s, $E_{\pi^{\pm}}$, will be twice that carried by π^{0}'s, $E_{\pi^{0}}$. In individual events the $E_{\pi^{\pm}} : E_{\pi^{0}}$ ratio can fluctuate widely. This will lead to a large spread of the energy measured by the calorimeter and consequently to a poor energy resolution:

$E_{\pi^{\pm}} : E_{\pi^{0}}$ = 3 : 0	rel. energy measured : 1.0
3 : 1	1.13
1 : 2	1.27
0 : 3	1.40

Obviously, the energy resolution can be strongly improved if the calorimeter has equal response to electrons and hadrons, e/h = 1 (compensated calorimeter). It has been shown (Ref. 31) that in this case a hadron energy resolution as good as $\sigma/E = (0.30 - 0.35)/\sqrt{E}$ can be achieved while noncompensating calorimeters yield typically $(0.5 - 0.6)/\sqrt{E}$.

In hadronic showers, the energy is deposited through electromagnetic cascades (E_{em}), ionization by charged hadrons (E_{had}) and nuclear breakup and excitation energy (E_{nuc}), (Ref. 32). The detection layers of the calorimeter respond differently to these different components and compensation requires a delicate balance between them. Up to now equal response to electrons and hadrons has been achieved only in calorimeters made from depleted uranium (DU) and scintillator (Ref. 31).

7.2 Compensation in a DU-Scintillator Calorimeter

The following effects determine the response of a DU-scintillator calorimeter to hadronic showers (see Fig. 41):

1. Ionization by charged particles produces energy loss in the detector (dE/dx).

2. Electromagnetic showers are the result of the decay of π^{0}'s. Electromagnetic energy (mainly low energy γ's) is predominantly lost in the high Z material. The difference in response to electromagnetic showers and minimum ionizing particles (e/mip ratio) (Ref. 33) is due to the different Z dependence of the cross sections for ionization $(\sim Z^{1})$, pair production $(\sim Z^{2})$, bremsstrahlung $(\sim Z^{2})$, photoelectric effect $(\sim Z^{5})$ and Compton effect $(\sim Z^{1})$. In a DU-scintillator sampling structure the e/mip ratio is around 0.6, weakly dependent on the plate thickness (see Fig.42). Crudely speaking, almost all of the energy of low energy photons is absorbed via the photoelectric effect in the nonactive high Z absorber material.

3. The hadron nucleus scattering in hadronic showers leads to nuclear breakup and fission; e.g. in massive uranium 0.6 GeV/c protons produce 9.8 fissions per GeV, 300 GeV/c pions produce 4.1 fissions per GeV (Ref.34). The missing binding energy E_{bind} is taken from the energy E_{inc} of the incident particle. In uranium for $E_{inc} = 10$ GeV the energy lost due to binding is typically $E_{bin} = (15-20\%) \, E_{inc}$ (Ref. 31). Some energy E_{ν} is also lost to neutrino emission. The sum of both shall be called E_{nuc},
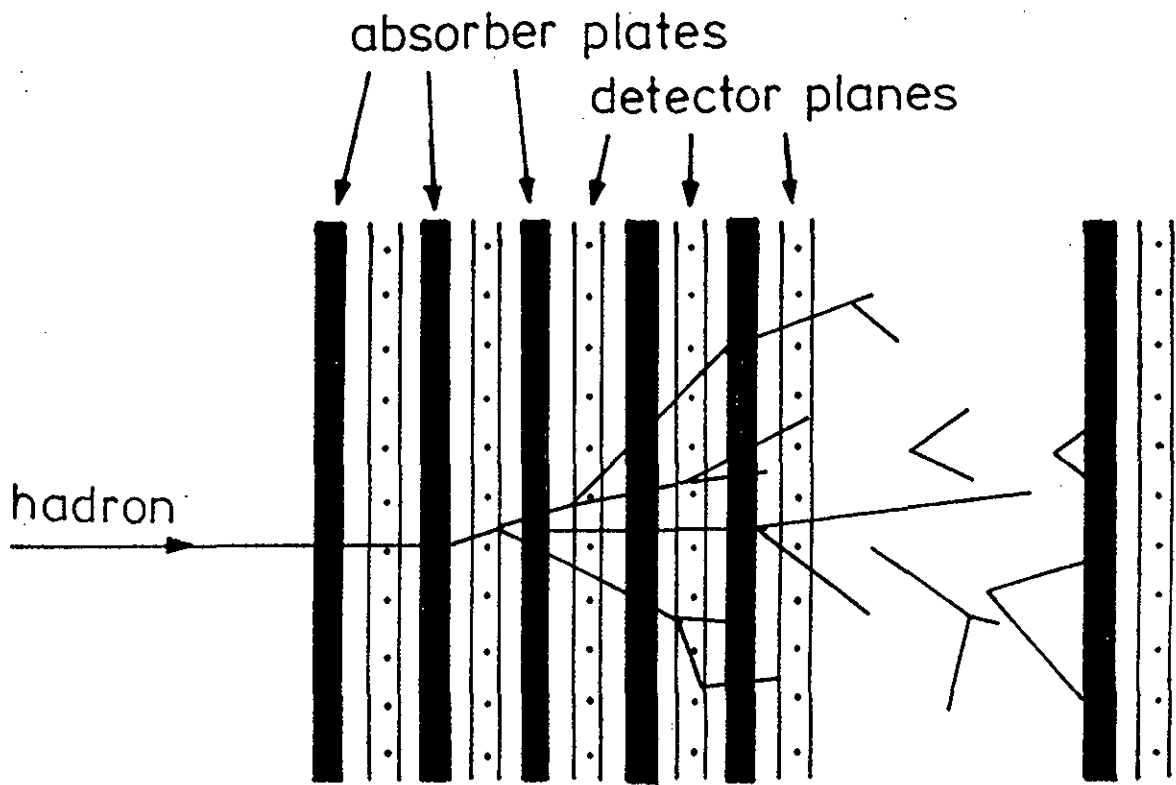
$$E_{nuc} = E_{bind} + E_{\nu}$$

absorber plates

detector planes

hadron

Fig. 40 Sketch of a sampling calorimeter.

Intranuclear Cascade Process

prim.
fission
second.

neutrons

charged
particles

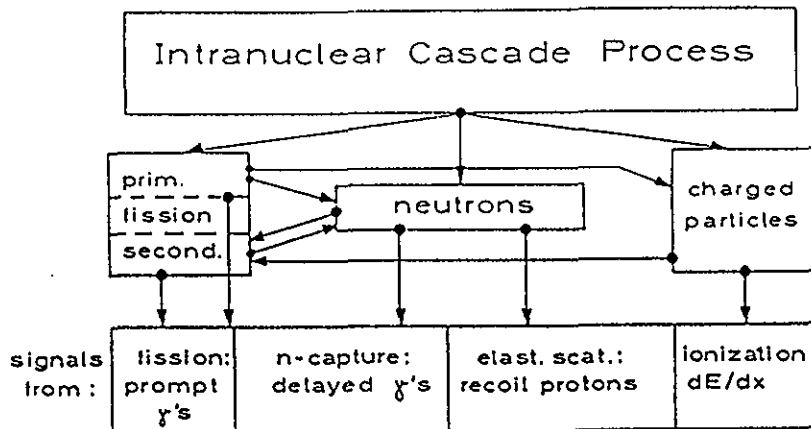| signals from : | fission: prompt γ's | n-capture: delayed γ's | elast. scat.: recoil protons | ionization dE/dx |

Fig. 41 Interactions contributing to compensation. Not shown
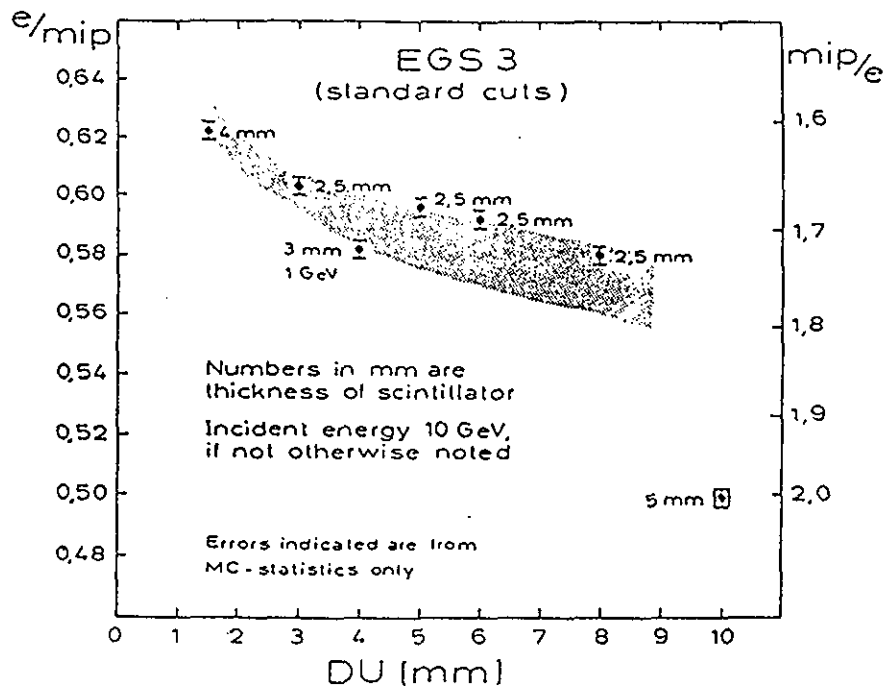is the electromagnetic component of hadronic showers.

Fig. 42   The e/mip ratio for several DU-scintillator structures,
          calculated with EGS (Ref. 7).*
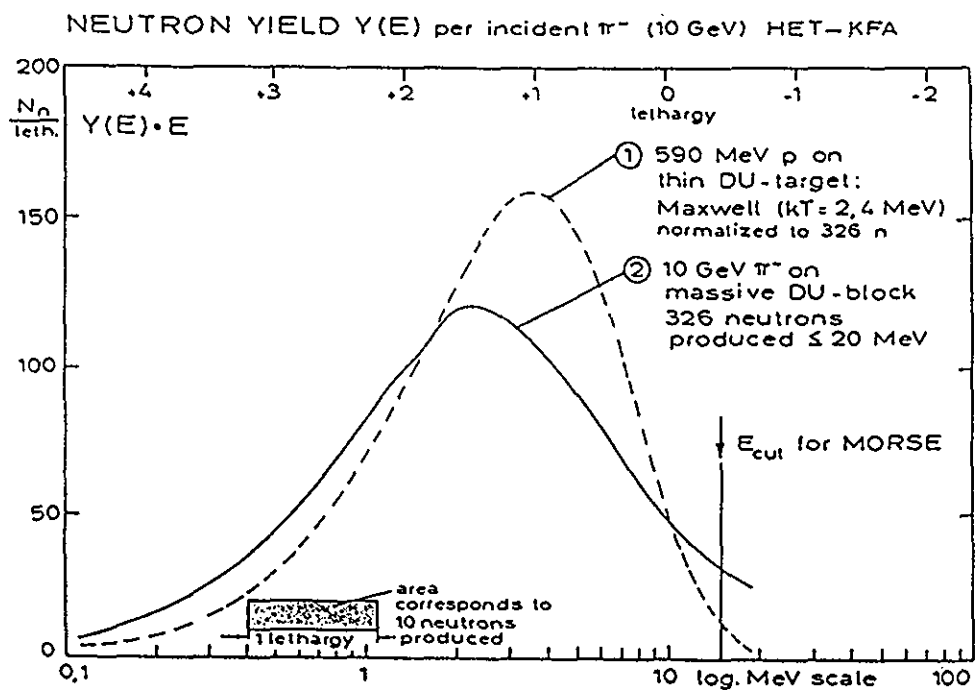

Fig. 43a   The neutron yield spectrum for a massive DU block (Ref. 7).

---

*
  Recent calculations with EGS4, using an improved stepping for electrons,
  indicate a larger e/mip value, e.g. e/mip = 0.67 instead of e/mip = 0.58.

4. In material with very high Z like DU, hadronic showers produce a significant number of neutrons with energies in the MeV range (Fig. 43a). For instance at E_{inc} = 10 GeV an average of about 450 neutrons is produced with a mean energy around 3 MeV. The hydrogen content of an organic scintillator converts most of the kinematic energy of the neutrons into measurable proton-recoil energy. Thus the hadron response is boosted considerably. In contrast, if liquid argon were used as detector material, the maximum energy transfer to the argon nucleus in an elastic n-Ar collision is 1/40 ($\equiv$ 1/A) of that of an np collision and consequently the boost of the hadron signal would be negligible.

5. Not all of the proton energy is detected in the scintillator, however, due to saturation of the scintillator. The average neutron energy is only 3 MeV, that of the recoil protons is even less. The velocity of a 3 MeV proton is β = 0.08. Since the ionization loss $dE/dx \sim 1/\beta^2$ the resulting ionization density is very high. The light output of the scintillator saturates according to Birk's law

$$\frac{dL}{dx} = \frac{S\ dE/dx}{1 + KB\ dE/dx}$$

where the factor KB has to be determined empirically. For NE102A KB = $1.0 \cdot 10^{-2}$, for SCSN38 KB = $0.85 \cdot 10^{-2}$ (Ref. 7) in units of $gcm^{-2}\ MeV^{-1}$. Fig. 43b shows the ionization loss and the light output for protons as a function of their kinetic energy.

6. The neutrons in the MeV range are moderated in energy mainly by elastic collisions with hydrogen. At very low neutron energies the neutron capture process dominates which yields delayed gamma radiation and hence a delayed boost of the signal.

7. Every spallation and every fission process is accompanied by prompt nuclear gamma deexcitation. Although the γ efficiency of scintillator is very low, the effect still contributes to the compensation. Liquid argon would detect a larger fraction of this and the delayed γ components due to its shorter radiation length (14 cm vs. 42 cm).

The preceding discussion shows that the calorimeter response to electrons and hence also to,photons is suppressed by about 40 % relative to a mip. The response to hadrons, in general, is suppressed even more. About 20 % of the energy is lost in the nuclear breakup. However, the breakup of uranium either by primaries or by secondaries (e.g. low energy neutrons) produce extra neutrons which release their energy mainly in the scintillator by elastic np scattering. What fraction of the neutron's energy

finally is seen by the photomultiplier depends on the saturation proper-
ties of the scintillator. As shown in the following, the uranium and scin-
tillator layers can be tuned to yield equal response to electrons and
hadrons.

We shall express the e/h ratio in terms of the pulse height contri-
butions for the electron and the hadron:

Electrons of energy E yield a pulse height $G_e(E)$;

Hadrons of energy E yield:

- π^0's with a total energy of E_1 yielding a pulse height of $G_e(E_1)$,

- charged hadrons with a total energy E_2 yielding via dE/dx a pulse
  height $G_x(E_2)$,

- neutrons with total energy E_3 yielding via proton recoil a pulse
  height $G_{rec}(E_3)$,

- energy E_4 lost to binding and neutrinos.

Note, the small contributions from prompt and delayed γ's have been
neglected; in the case of scintillator their energy can be included
in E_4.

Now make the following assumptions:

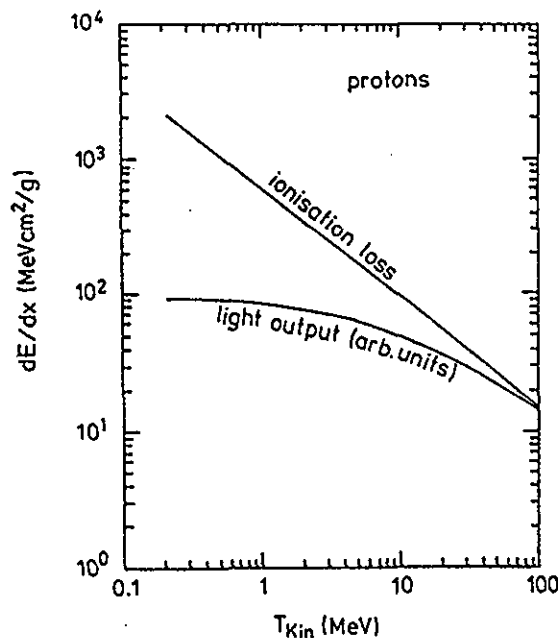1. The pulse height $G_i(E)$ (i = e,x,...) is proportional to E, i.e.
   $G_i(E) = g_i E$.

Fig. 43b   The ionization loss and the light output (in arb. units) for
protons for a KB value of 0.01 $gcm^{-2}MeV^{-1}$.

2. The energy carried by neutrons is proportional to the energy lost to the binding energy (plus neutrinos),

$$E_3 = aE_4$$

and

$$E = E_1 + E_2 + E_3 + E_4$$

This yields

$$\frac{h}{e} = \frac{G_h(E)}{G_e(E)} = \frac{g_e E_1 + g_x E_2 + g_{rec} E_3}{g_e E}$$

$$= 1 - \left[1 - \frac{g_x}{g_e}\right]\frac{E_2}{E} - \left[(1 + \frac{1}{a}) - \frac{g_{rec}}{g_e}\right]\frac{E_3}{E}$$

We shall now make a further and not yet well founded assumption:

3. The pulse heights produced by electrons and produced via dE/dx by hadrons are equal,

$$g_x = g_e,$$

and obtain

$$\frac{h}{e} = 1 - \left[(1 + \frac{1}{a}) - \frac{g_{rec}}{g_e}\right]\frac{E_3}{E}$$

Compensation can now be achieved for any energy partition E_3/E and therefore separately for each event if

$$\frac{g_{rec}}{g_e} = (1 + \frac{1}{a})$$

With an e/h ratio equal to unity for each individual event we expect to obtain the best energy resolution possible.

Figure 44 illustrates how the ratio g_{rec}/g_e might be tuned to achieve compensation. It is the result of a model calculation for a DU-scintillator calorimeter with d_u = 3 mm thick DU plates and variable scintillator thickness d_s (Refs. 7, 35). The air gaps between scintillator and DU plates are assumed to be small (< 0.5 mm). The scintillator is assumed to have a kB factor of $0.85 \cdot 10^{-2}$ g/MeV cm^2 (as is the case e.g. for SCSN38). The gate length is assumed to be 100 ns. Compensation is predicted for d_u/d_s = 1.4 or a scintillator thickness of 2.1 mm. This is close to the 2.5 mm that has been used by Ref. 31 for their DU-
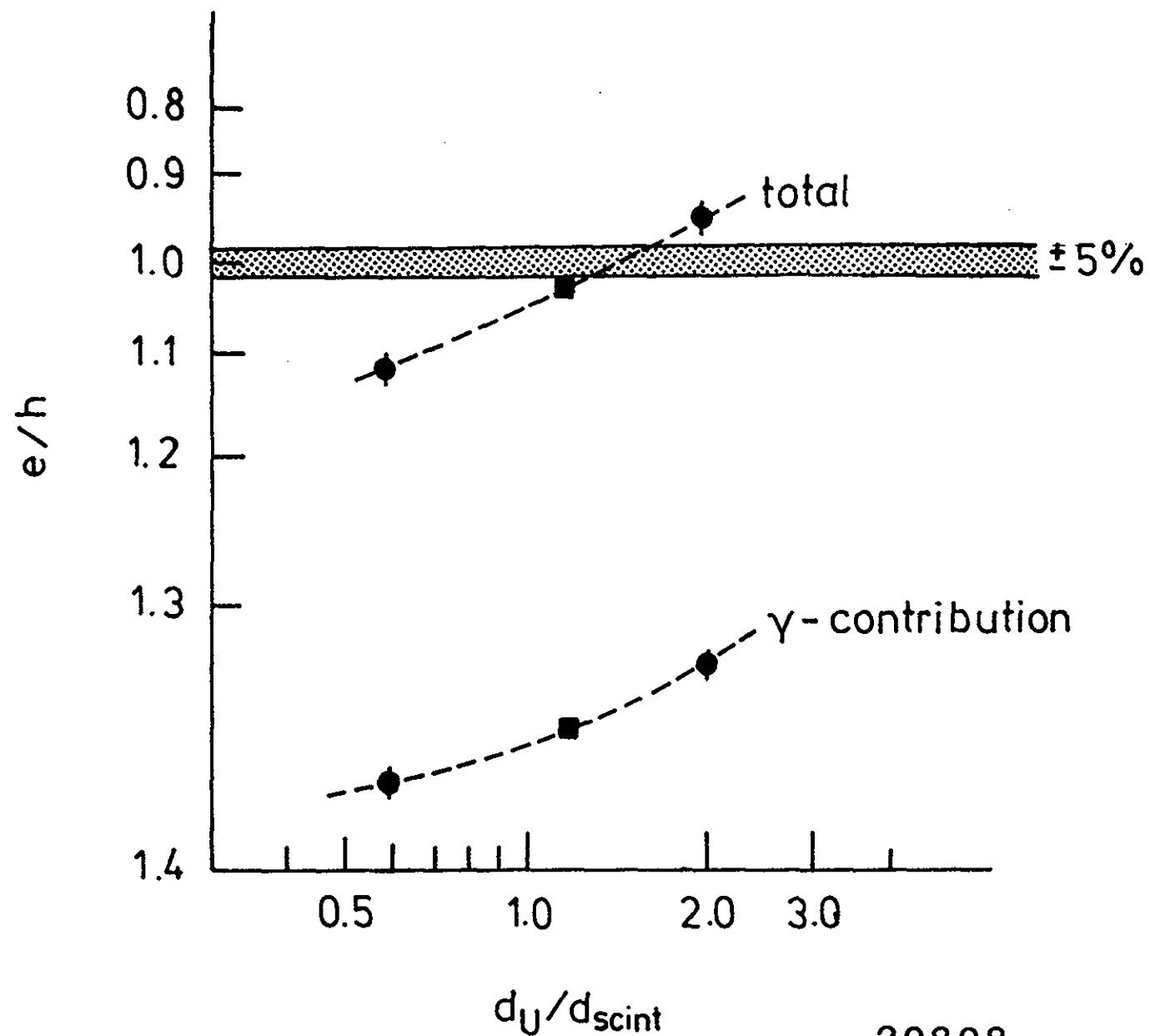
Fig. 44   The e/h ratio as a function of the ratio of the DU to
scintillator thickness (Ref. 7).

39828

scintillator calorimeter. Figure 44 shows that for a fixed DU plate thickness a thicker scintillator will increase the e/h ratio, a thinner one will decrease it.

The energy resolution in a compensated DU-scintillator calorimeter can be written as (Ref. 36):

$$\frac{\sigma(E)}{E} = \frac{22 \ \%}{\sqrt{E}} \oplus \frac{0.09 \ \sqrt{\Delta E(1 + 1/N_{pe})}}{\sqrt{E}}$$

where ΔE measures in MeV the energy loss of a mip per absorber plate. The $\oplus$ sign stands for quadratic addition. The second term under the square root represents the contribution from photon statistics: N_{pe} is the number of photoelectrons seen by the phototube per mip and layer. For instance for 3 mm DU, 2.5 mm scintillator, N_{pe} = 4 the expected energy resolution is

$$\frac{\sigma(E)}{E} = \frac{22 \ \%}{\sqrt{E}} \oplus \frac{25 \ \%}{\sqrt{E}} = \frac{33 \ \%}{\sqrt{E}}$$

The potential of a uranium scintillator calorimeter is illustrated in Figs. 45a,b. On top is shown the pulse height distribution measured by ZEUS (Ref. 7) with a lead-scintillator calorimeter (5 mm Pb plates, 5 mm scintillator) for a 5 GeV beam composed of electrons, muons and hadrons. The electron signal is considerably larger than that for the hadrons, e/h ≈ 1.3. The bottom distribution shows the result obtained for the same beam with the same calorimeter after replacing the lead plates with 3.2 mm thick uranium plates. The electron and hadron signals are almost equal, e/h ≈ 1.07. (Note, that the choice of scintillator thickness was not optimum). It is also evident that the hadron signal has become narrower.

Figure 45c shows measurements (Ref. 37) from the NA34 experiment at CERN using 3 mm DU plates interleaved with 2.5 mm scintillator plates. The resolution varies between $\sigma/\sqrt{E}$ = 28 % and 36 %, the average being 33 % for pions from 8 to 200 GeV.

7.3   Weighting in a Noncompensating Calorimeter

The energy resolution in a noncompensating calorimeter such as Fe-scintillator is given by

$$\frac{\sigma(E)}{E} \approx \frac{40 \ \%}{\sqrt{E}} \oplus \frac{0.09 \ \sqrt{\Delta E(1 + 1/N_{pe})}}{\sqrt{E}} + 5.5 \ \%$$

The last term arises from the event-to-event fluctuations in the energy deposited by π^{0}'s and the difference in response to e and h. One can get
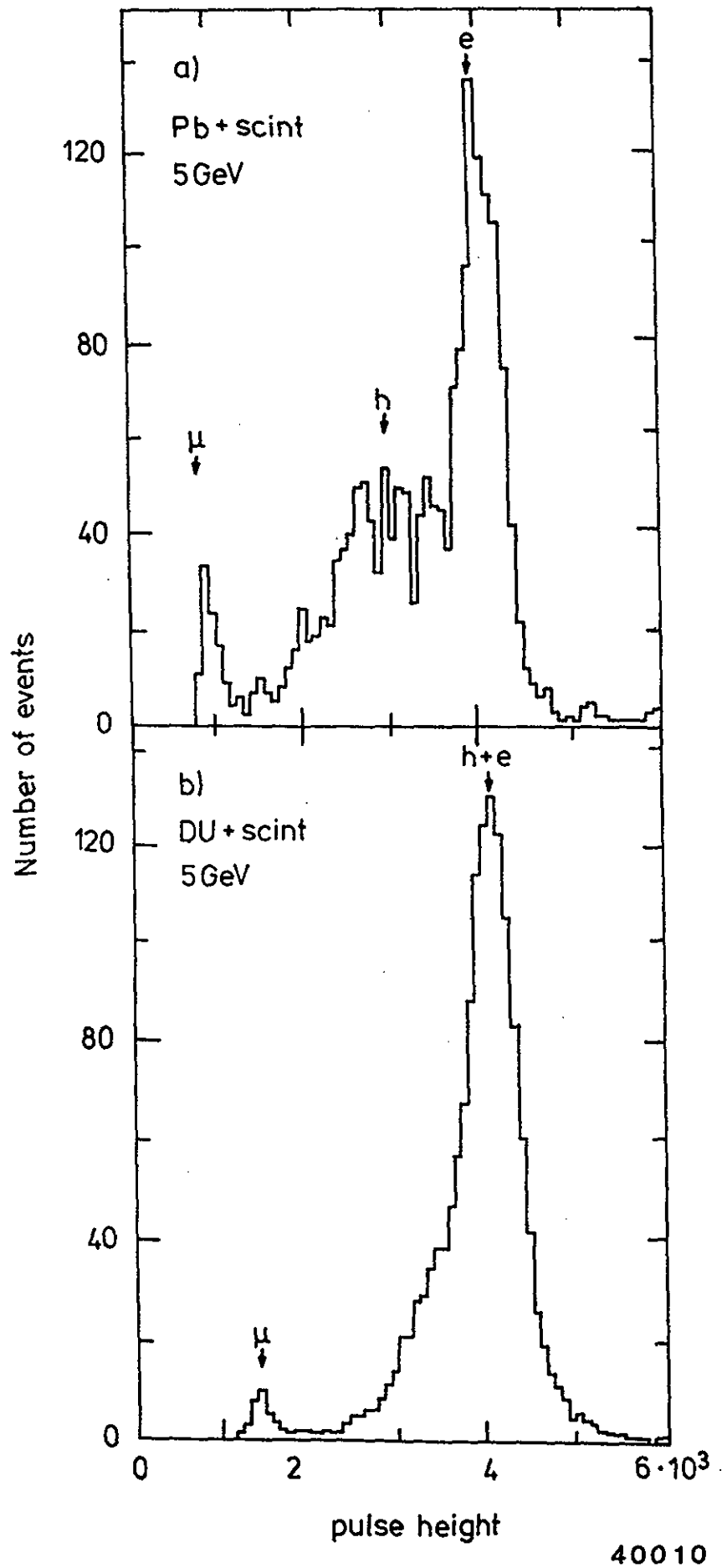
ZEUS

40010

Fig. 45 Pulse height distributions for 5 GeV electrons, muons and
hadrons observed with a lead - scintillator (5 mm Pb, 5 mm scint)
calorimeter (a), and with a uranium - scintillator (3.2 mm DU,
5 mm scint) calorimeter (b). From ZEUS collaboration.

rid of this term by a crude estimate of the π^0 content of the shower. The idea is the following: The shower of a charged hadron is typically spread over 3 - 5 absorption lengths, (e.g. $\lambda(Pb)$ = 17.0 cm) while the energy of a π^0 is absorbed within 5 to 10 radiation lengths, X_0 (e.g. $X_0(Pb)$ = 0.58 cm). The π^0 energy deposits are therefore very localized in a hadronic shower; they form hot spots. By measuring the energy content of hot spots the energy deposited by π^0's can be estimated.

In practice it is sufficient to measure the first and second moment of the energy release along the shower. Figure 46 shows the result from an iron-scintillator calorimeter (Ref. 38) using 2.5 cm thick Fe plates
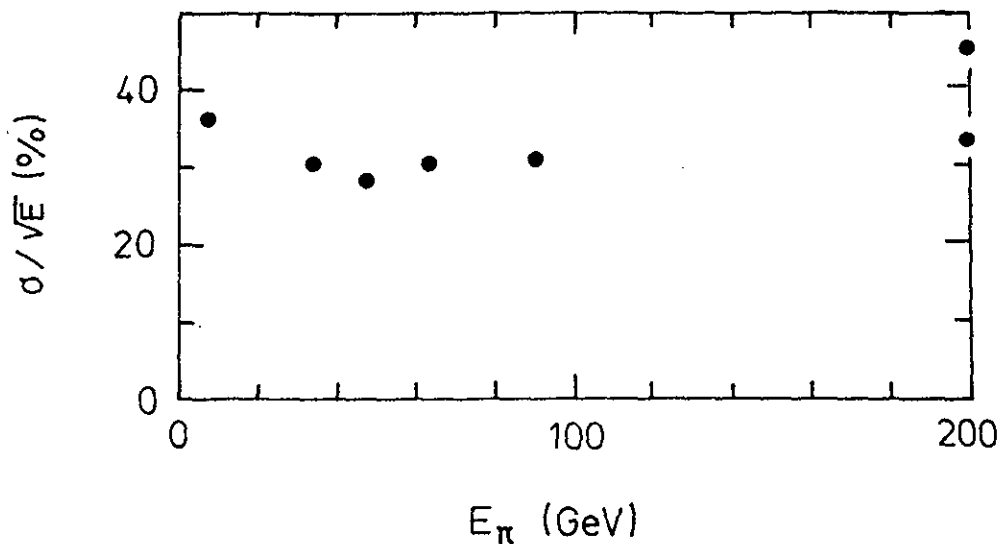

Fig. 45c The energy resolution of a DU-scintillator calorimeter (Ref. 7).

(λ(Fe) = 16.8 cm). Every 5 layers were readout by a separate phototube i yielding the measured energy E^i_{meas}. The corrected energy E^i_{corr} is found by (Refs. 38, 39)

$$E^i_{meas} = E^i_{corr} \, (1-\alpha \, E^i_{corr})$$

$$E_{meas} = \sum_i E^i_{meas} = \sum_i E^i_{corr} - c \, \frac{\sum_i (E^i_{corr})^2}{\sqrt{\sum_i E^i_{corr}}}$$

The constant c depends on the e/h ratio.

As shown by Fig. 46 the energy resolution in the unweighted case increases from $\sigma(E)/\sqrt{E}$ = 60 % near E = 10 GeV to ~100 % at 200 GeV incident pion energy. After weighting the energy resolution remains 60 % over the full energy range.

7.4 Depth of the Calorimeter

In order to preserve the optimum energy resolution at all energies, the calorimeter has to be sufficiently deep. The depth profile of hadronic showers was measured experimentally in the WA78 experiment at CERN using a 5.2 λ deep DU-scintillator calorimeter followed by a 7.5 Fe-scintillator calorimeter. Fig. 47 shows as an example the fraction of 30 GeV/c single hadron showers and of jet showers with 90, 95 and 97 % energy containment as a function of the calorimeter depth. In order to have 95 % containment for 90 % of 30 GeV/c hadrons a depth of 6 λ is required. For jets the necessary depth is about 1 λ smaller.

The maximum jet energy for HERA is shown in Fig. 48 as a function of the production angle Θ. It reaches 800 GeV near the forward direction, falling to 300 GeV at 30°, 100 GeV at 60° and less than 50 GeV beyond 90°. Requiring 99 % containment leads to a depth of ~11 λ in the forward direction, 7 λ at 90° and 6 λ at 180°.

In general, cost considerations prohibit the construction of a high resolution calorimeter over the full depth. Instead, the calorimeter is divided into a high resolution front part and a backing calorimeter with moderate energy resolution. The backing calorimeter recog-
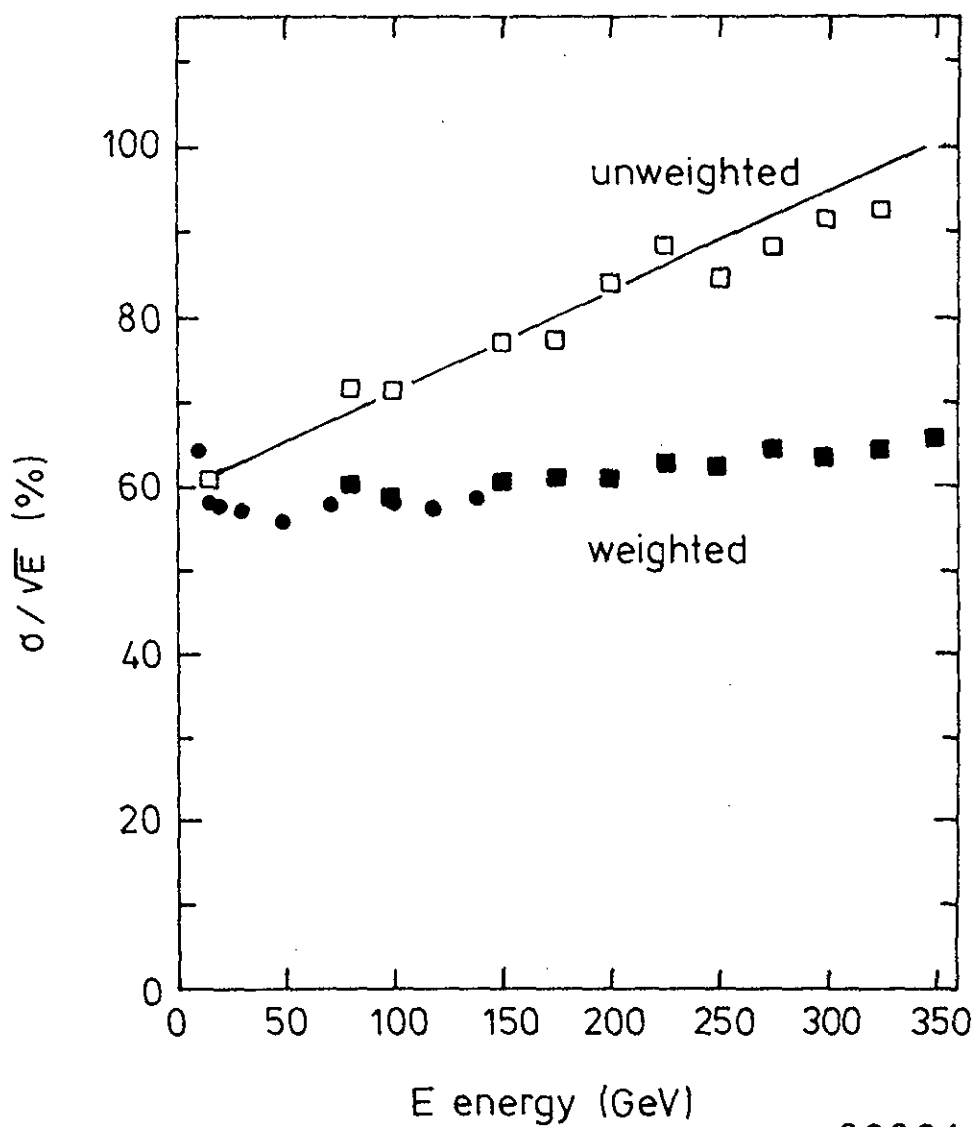
Fig. 46 The energy resolution of a Fe-scintillator calorimeter
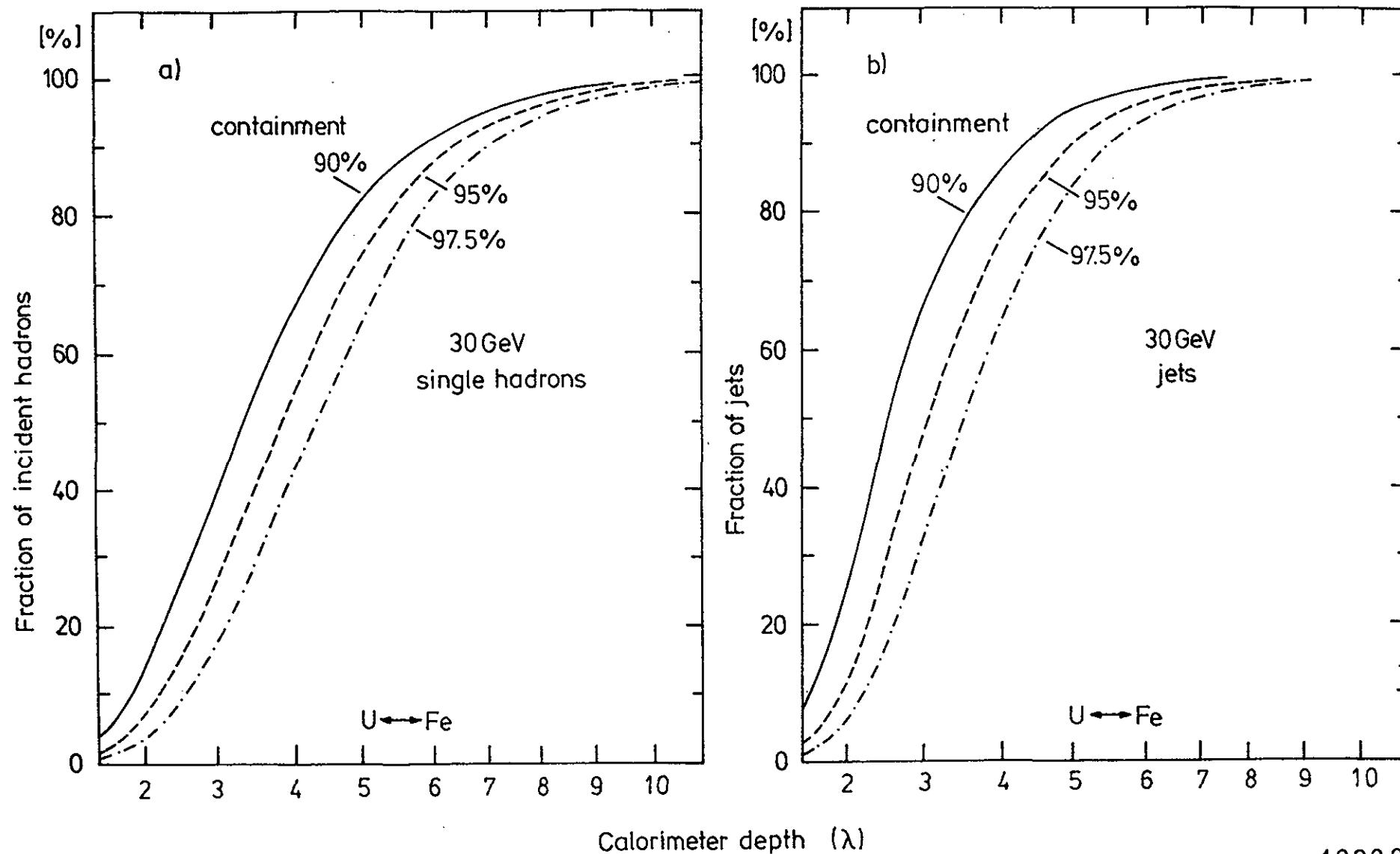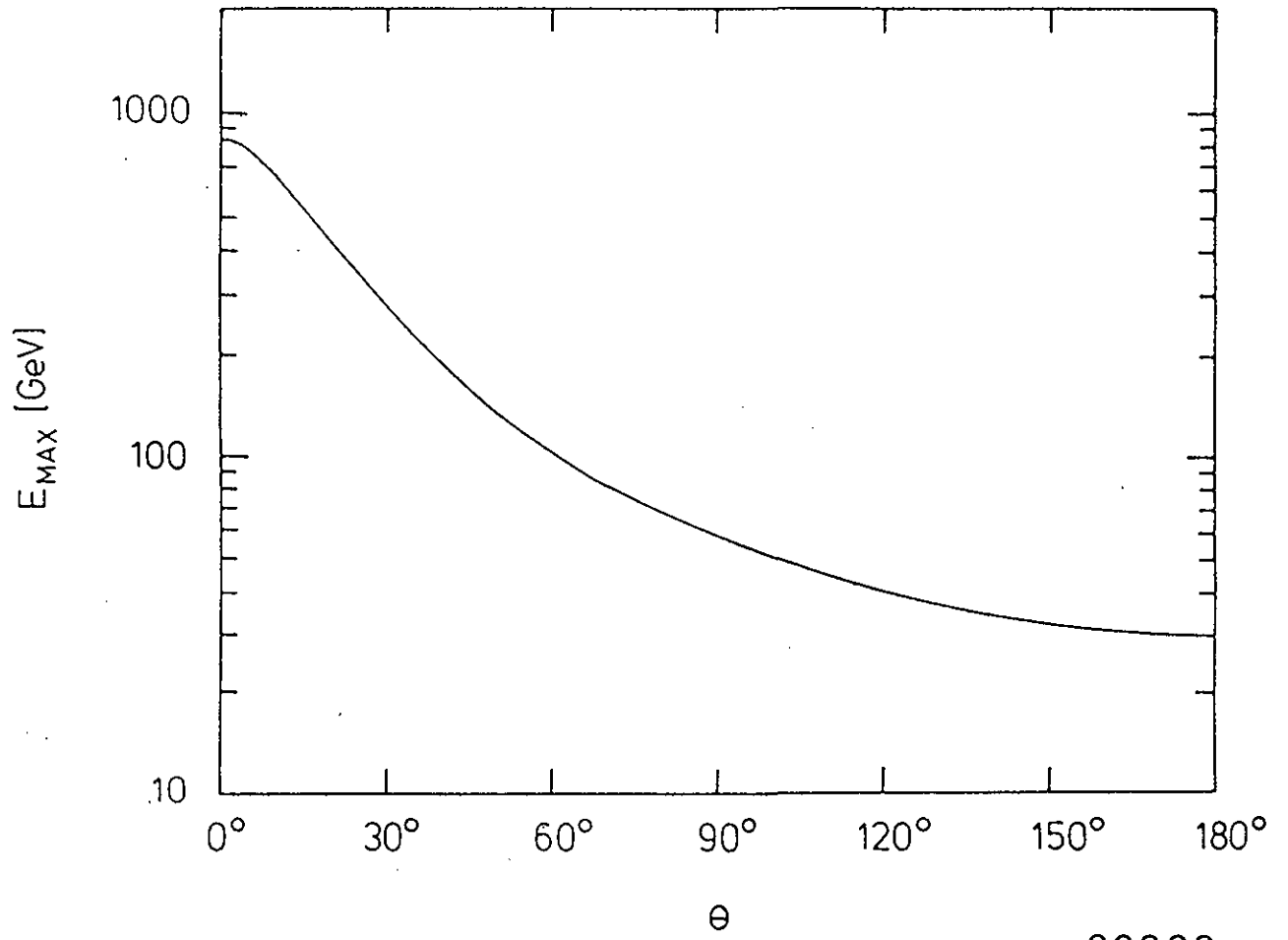before and after weighting (Ref. 38).

Fig. 47   Fraction of 30 GeV single hadrons (a) and of 30 GeV jets with 90%, 95% and 97.5%

energy containement versus calorimeter depth (J. Krüger, priv. comm.).

Fig. 48 Maximum jet energy as a function of polar angle.

nizes late showers and can be used to correct for energy leakage or to select a high resolution sample.

8.   PROPOSED HERA EXPERIMENTS

Two collaborations, ZEUS and H1, have proposed to construct detectors for HERA. In 1985 they have submitted letters of intent (Ref. 40, 41) which have been followed in 1986 by technical proposals (Refs. 42, 43). These proposals are presently under review by the DESY Physics Research Committee and approval is expected for summer of this year.

Both detectors require large efforts in terms of personnel and investment. The ZEUS collaboration consists of 268 physicists and estimates the material budget required to build the detector at 135 MDM. The corresponding numbers for H1 are 165 physicists and 92 MDM. Both groups envisage completion of the detector by 1990.

8.1   The H1 Detector

The layout of the detector is shown in Figs. 49, 50. Starting from the interaction point,charged particle tracking in the central and forward region is provided by a central jet-chamber interleaved with two z-chambers, and MWPC's (1) (inner, outer radii: 15, 90 cm) and a forward tracker (2) consisting of a series of radial and planar drift chambers interleaved with three layers of MWPC's and transition radiators. In combination with a magnetic field of 1.2 T the momentum resolution expected for isolated charged particles between 7° and 150° is $\sigma(P)/P^2 \leq 0.003$.

The EM calorimeter utilizes Pb plates with liquid argon as readout in the barrel and forward region (3) and a lead scintillator sandwich in the backward region (5). The liquid argon part of the EM calorimeter is highly segmented. It consists of 3×3 cm^2 towers and 4 longitudinal readouts in the forward direction and of 8×8 cm^2 towers and 3 readouts in the backward barrel region.

**Layout of the
H 1 detector**

**Vertical cut
along the beam**

1 CENTRAL TRACKING
2 FORW. TRACKING + TRD
3 ELECTR. LIQU. AR. CALORIM.
4 HADR. LIQU. AR. CALORIM.
5 BACKW. ELECTR. CALORIM.
6 COIL
7 INSTRUM. IRON
8 IRON TOROID
9 MUON CHAMBERS
10 PLUG CALORIMETER
11 COMPENS. COIL
12 MACHINE QUADRUPOLE
13 CONCRETE
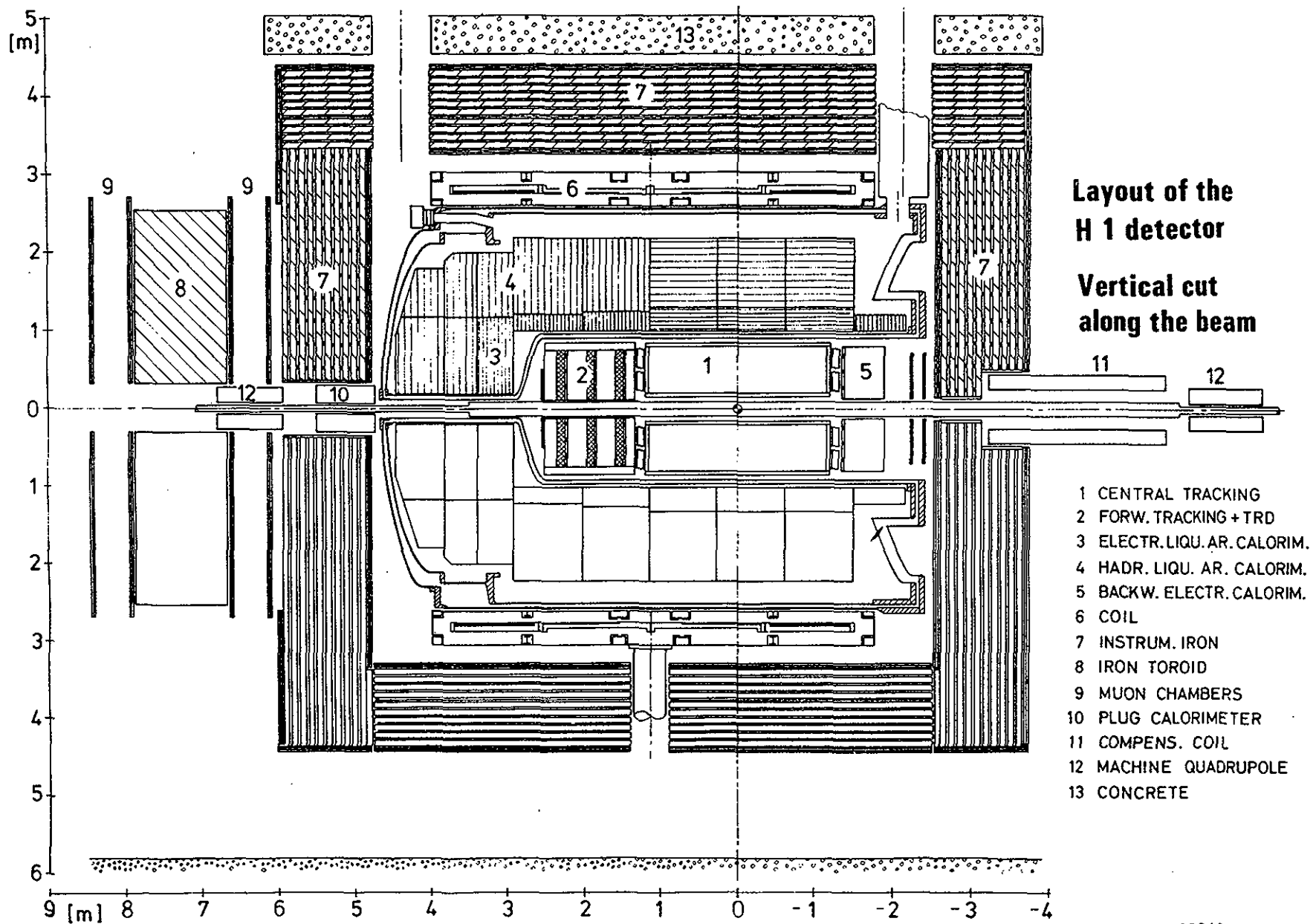
Fig. 49 Section of the H1 detector along the beam.

39612

Layout of the H 1 detector

**Vertical cut
transversal to the beam**

1 CENTRAL TRACKING
3 ELECTR. LIQU. AR. CALORIM.
4 HADR. LIQU. AR. CALORIM.
6 COIL
7 INSTRUM. IRON
9 MUON CHAMBERS
13 CONCRETE
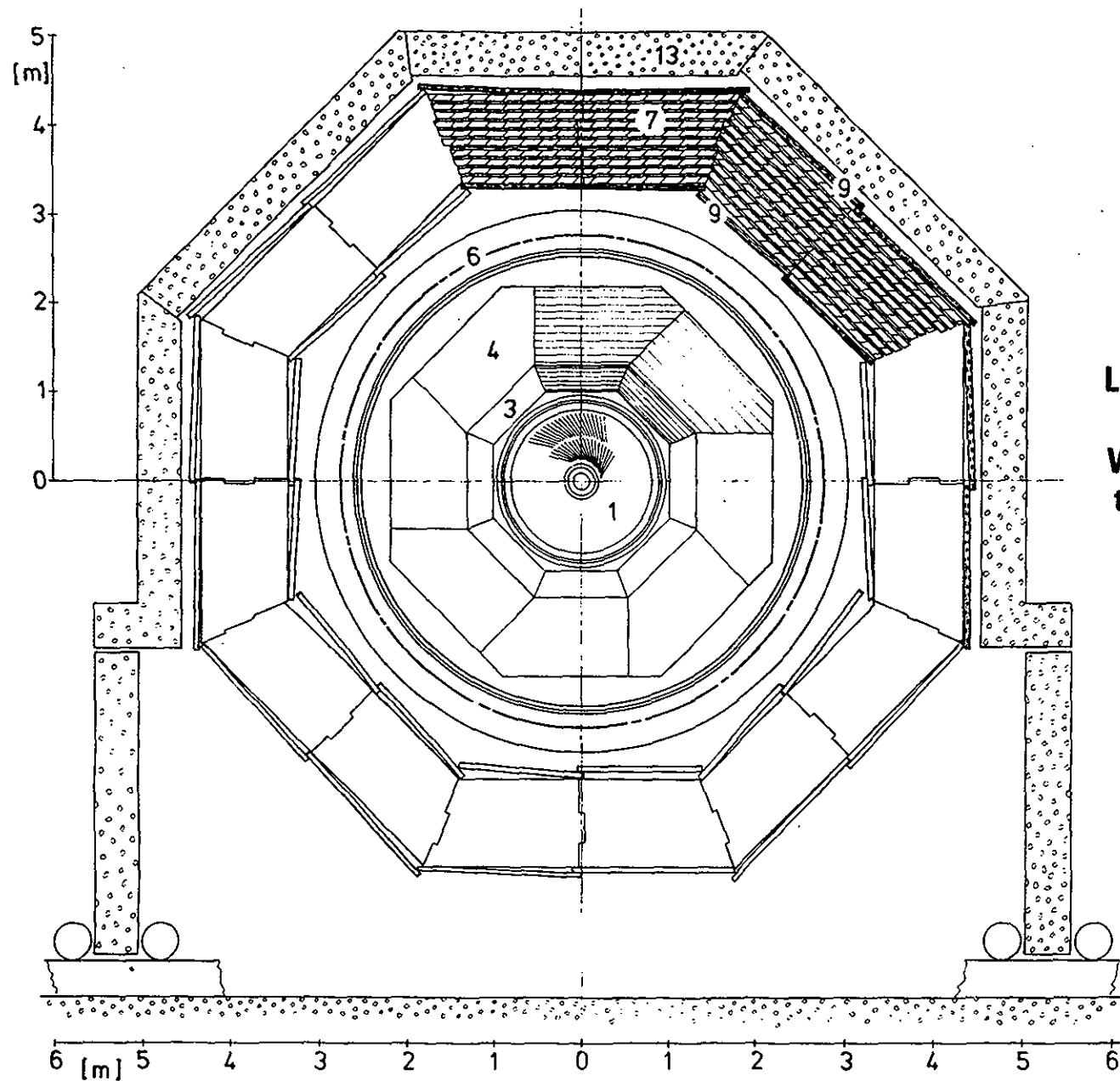
39613

Fig. 50 Section of the H1 detector perpendicular to the beam.

The hadron calorimeter uses stainless steel absorber plates with liquid argon readout. The EM and hadron calorimeters provide an energy resolution of $\sigma(E)/E \leq 10\ \%/\sqrt{E}$ for electrons and, using a weighting procedure, $\sigma(E)/E = 55\ \%/\sqrt{E} \oplus 2\ \%$ for hadrons.

A superconducting coil (inner, outer radii 260, 304 cm, length 575 cm) encloses the calorimeter and provides a longitudinal field of 1.2 T.

The solenoid and calorimeters are surrounded by a set of iron plates (7) to contain the return flux. The iron is instrumented with plastic streamer tubes and acts as a backing calorimeter and muon filter.

Muon detection is provided by three layers of muon chambers (9) in the barrel and forward region complemented by a forward muon spectrometer consisting of a magnetized iron toroid (8) and four layers of drift chambers (9).

A plug calorimeter (10) detects hadronic energy at small angles down to 0.7°. It consists of a copper silicon sandwich.

The field produced at the beam by the large coil is compensated by an additional solenoid (11).

We shall describe the calorimeter and the tracking system in more detail.

8.1.1 The liquid argon calorimeter

The arrangement of the absorber plates and the thickness in absorption length of the H1 LA calorimeter is indicated in Figs. 51, 52. The electromagnetic part (EMC) uses 2.4 mm lead plates and 3.0 (or 2 x 1.5) mm argon gaps. The hadronic part (HAC) is made of 12 mm stainless steel plates separated by 2 x 1.5 mm argon.* The number of layers and depths are summarized in Table 7.

---

* In the meantime the H1 collaboration has decided for 18 mm thick Fe plates and 2 * 2.5 mm LAr gaps.
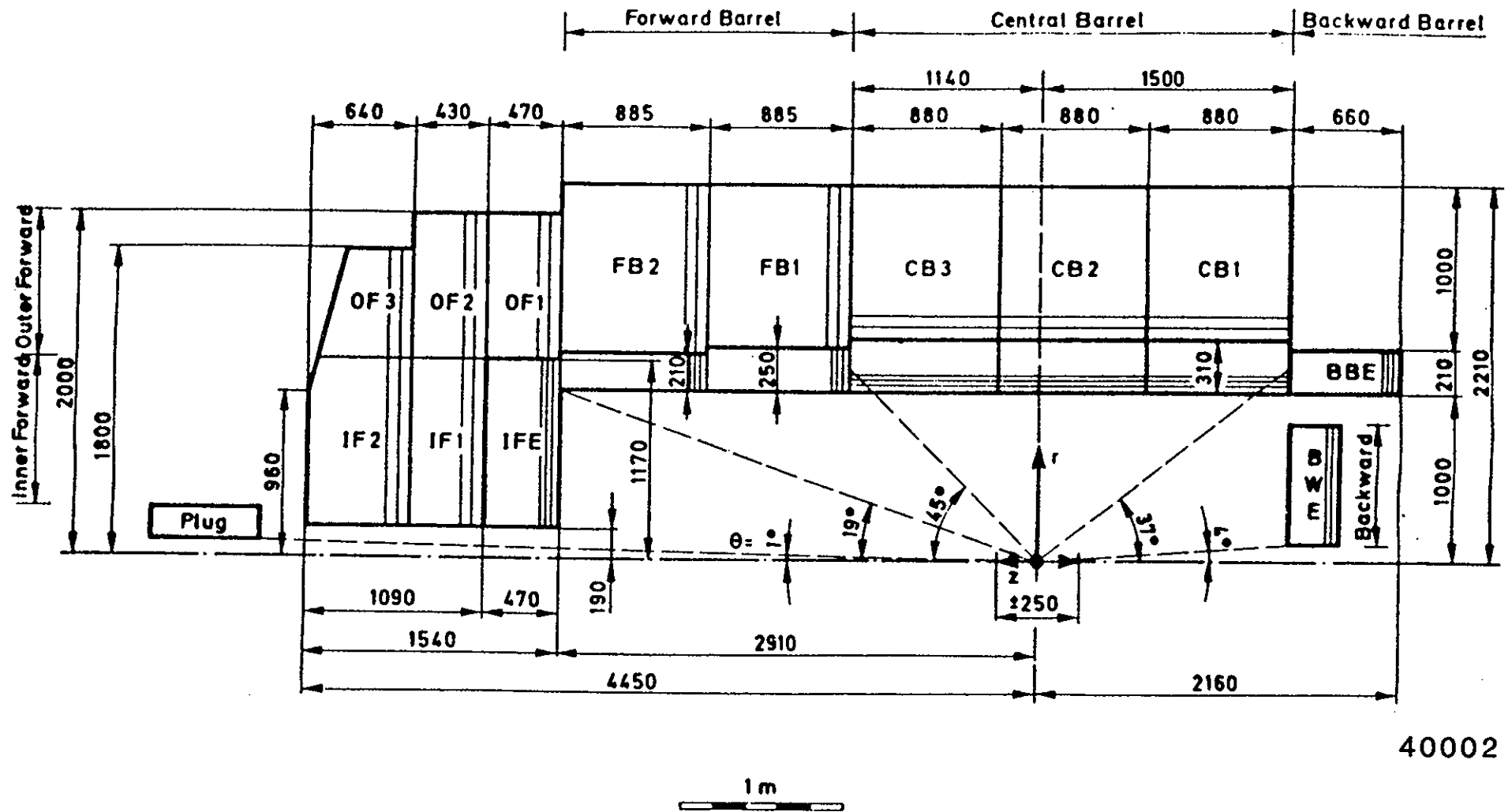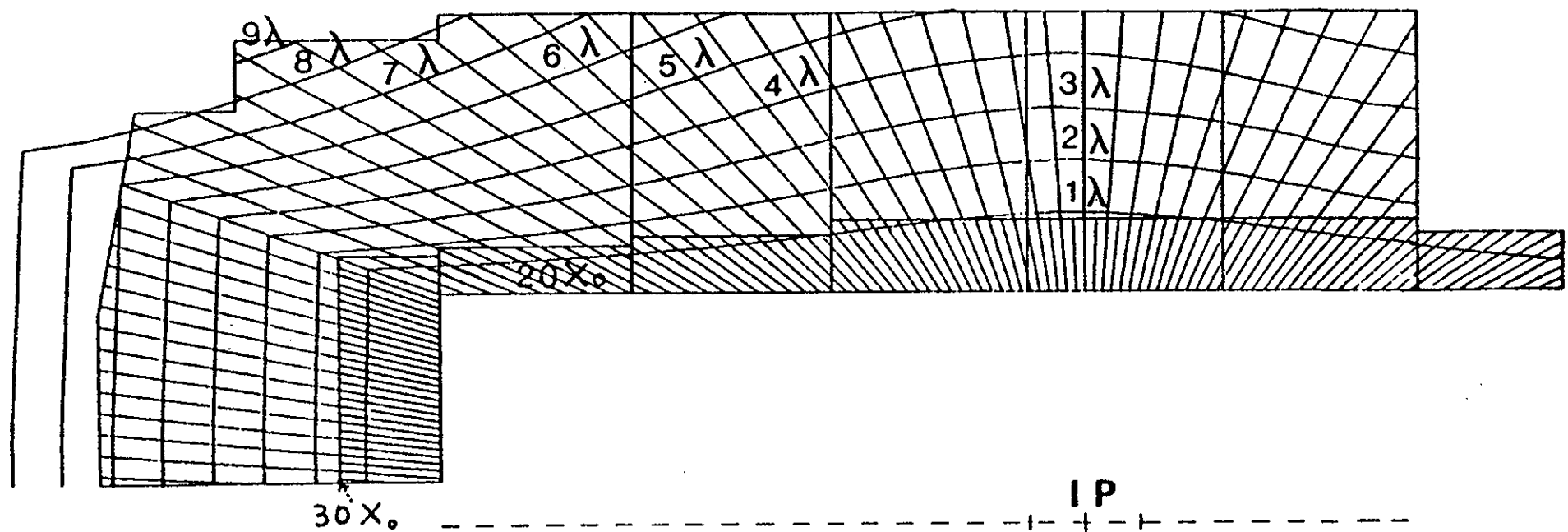
Fig. 51 Layout of the H1 liquid argon calorimeter.

40003

Fig. 52   Amount of absorber material in the EM sections of the H1 calorimeter.

Table 7: Properties of the LA calorimeter for H1

| Θ	section	n.of layers	depth (cm)	X_0	λ	tower size (cm^2)	number of longt.segm.
near 0°	EMC	65	47	30	1.5	3 x 3	4
	HAC	58	107	43	4.5	7x7→15x13	5 or 6
90°	EMC	43	31	20	1.0	8 x 9	3
	HAC	48	90	34	3.8	15 x 13	4

Liquid argon (LA) offers several advantages as a readout medium. The calibration can be kept constant over several years at the one-percent level provided the argon does not get contaminated. The response is uniform across the readout area. LA readout does not suffer from radiation damage. Furthermore it allows in an easy way fine transverse and longitudinal segmentation. Its major drawback is that up to now it has not been possible to design a compensating LA calorimeter. Another drawback is the long charge collection time.

The weight of the calorimeter is 57 t lead, 327 t Fe and 80 t LA.

The calorimeter is highly segmented. The transverse segmentation will be helpful for the recognition of electrons within jets. The longitudinal segmentation is chosen for the application of the weighting technique since the calorimeter will be noncompensating. In total there are 42 100 readout channels for the EMC and 18 238 for the HAC.

The readout gaps are sketched in Fig. 53: with two alternative solutions for the EMC (a,b) and one for the HAC (c). For the EMC the high voltage is applied between the Cu layer of the upper G10 board and a resistive paint layer (10 MΩ/square) on the lower board. The induced signal is collected by pads beneath the layer of resistive paint. The leads to bring the signal out are either in the same plane (a) or run on the lower side of the G10 board (b). The charge collection time will be either 600 ns (3 mm LA gap) or 300 ns (1.5 mm LA gap).

The design of the electronics is faced with the problem of noise pick-up. Two solutions are under study. In the warm solution the preamplifiers are located on the outside of the cryostat. In the cold solution preamplifier and multiplexor are next to the stack inside of the liquid argon tank. The latter solution should have less problems with noise but requires a certain optimism w.r.t. the lifetime of the electronic components.
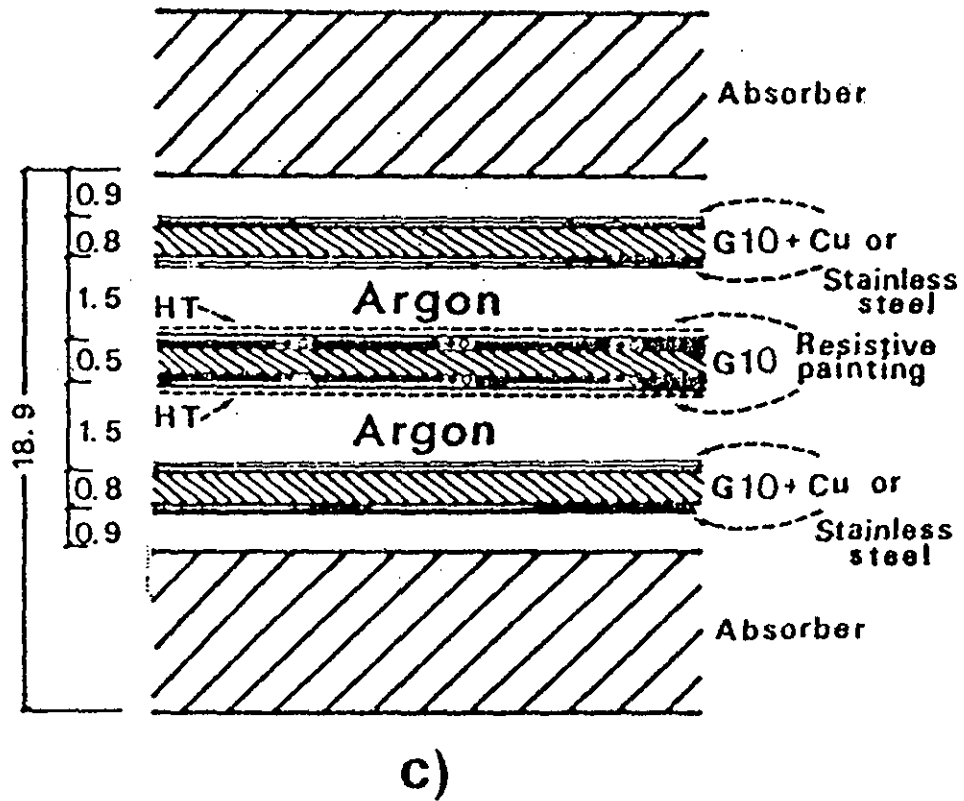
a)

b)

c)
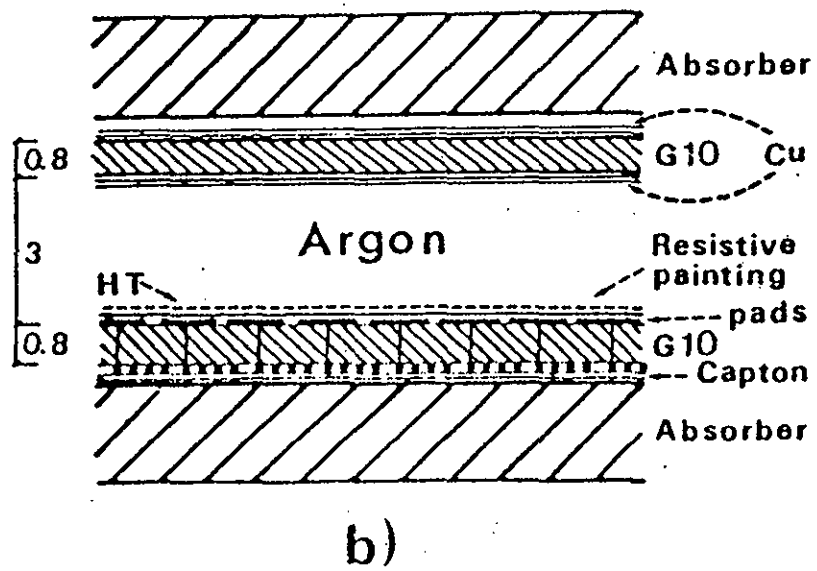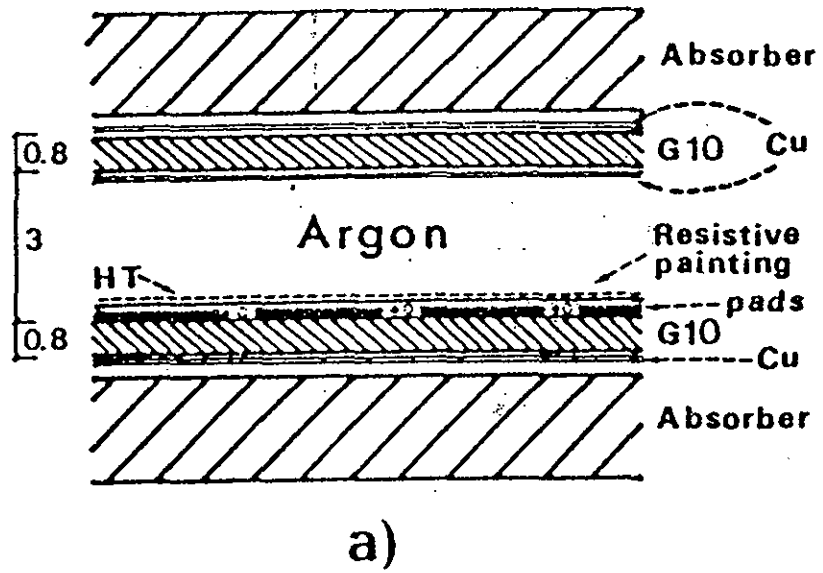
Fig. 53 Read out gaps for the H1 liquid
argon calorimeter. a) and b) show
two different solutions for the
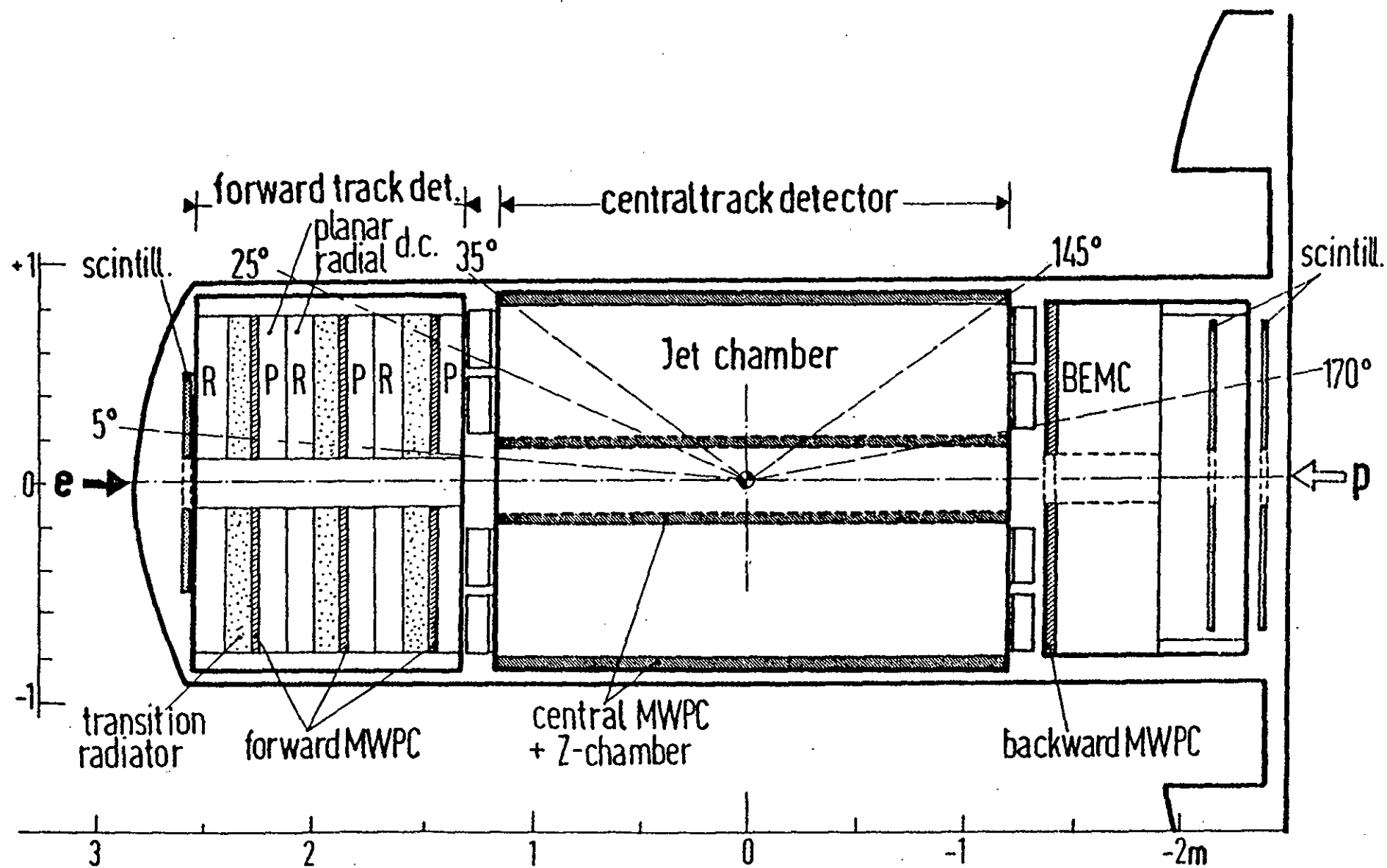EM gap, c) shows a gap in the
HAC section.

39994

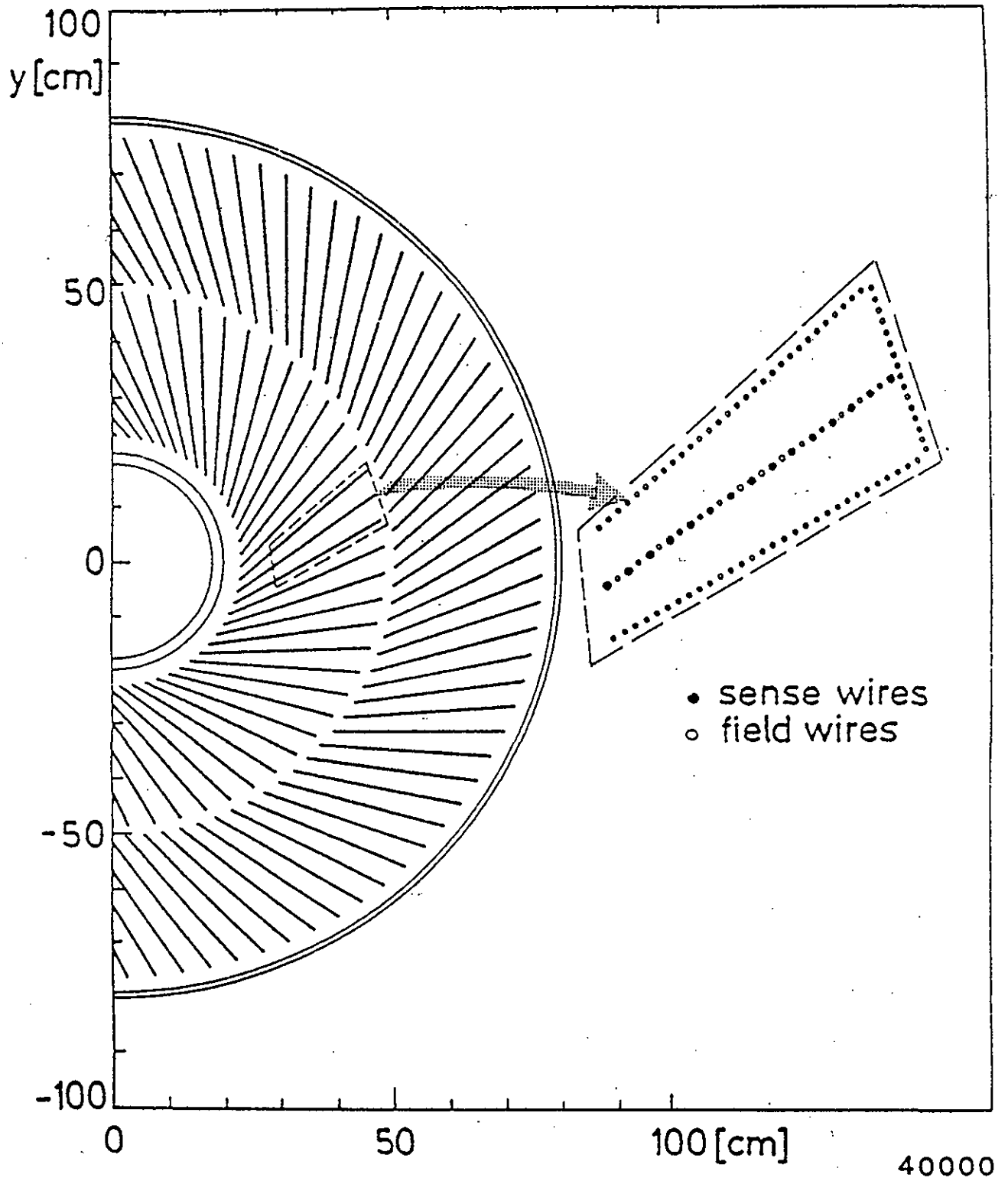Fig. 54 Layout of the tracking system for H1.

Fig. 55   Cross section of the H1 central tracking chamber.

8.1.2 The tracking system

An overview of the inner tracking detectors is shown in Fig. 54. The central region is surrounded by a jet type drift chamber. Plane drift chambers measure the paths of forward and backward going particles. Transition radiators followed by multiwire proportional chambers help to identify electrons.

Figure 55 indicates the wire arrangement in the jet chamber. The drift cells do not point to the interaction point but are tilted to account for the Lorentz angle. The maximum drift path is 5.1 cm corresponding to 1.5 µs drift time or 15 beam crossings. The chamber has an outer radius of 80 cm, a length of 264 cm and is operated at atmospheric pressure. There are 64 layers of sense wires leading to a total of 2560 sense wires and 10 000 field wires, all strung parallel to the beam axis. The expected $r\varphi$ resolution is 100 µm. Charge division on the sense wires yields some z-information. Precise z measurements are provided by separate drift chambers attached at the inner and outer radii of the jet chamber (see Fig.54).

8.2   The ZEUS Detector

The layout of the detector is shown in Figs. 56-58. The essential elements are a central track detector (CTD) plus transition radiation (TRD) and planar chambers (FTD, RTD) within a thin magnetic solenoid (SOLENOID), an electromagnetic (EMC) and a hadron calorimeter (HAC) surrounding the coil over the full solid angle, a backing calorimeter (BAC), barrel and rear muon detector (MU), and a forward muon spectrometer (FMU).

The calorimeter consists of depleted uranium plates with plastic scintillator in order to achieve compensation and the best possible energy resolution for hadrons. The scintillator plates form towers which are read out via wave length shifer bars, light guides and photomulti-

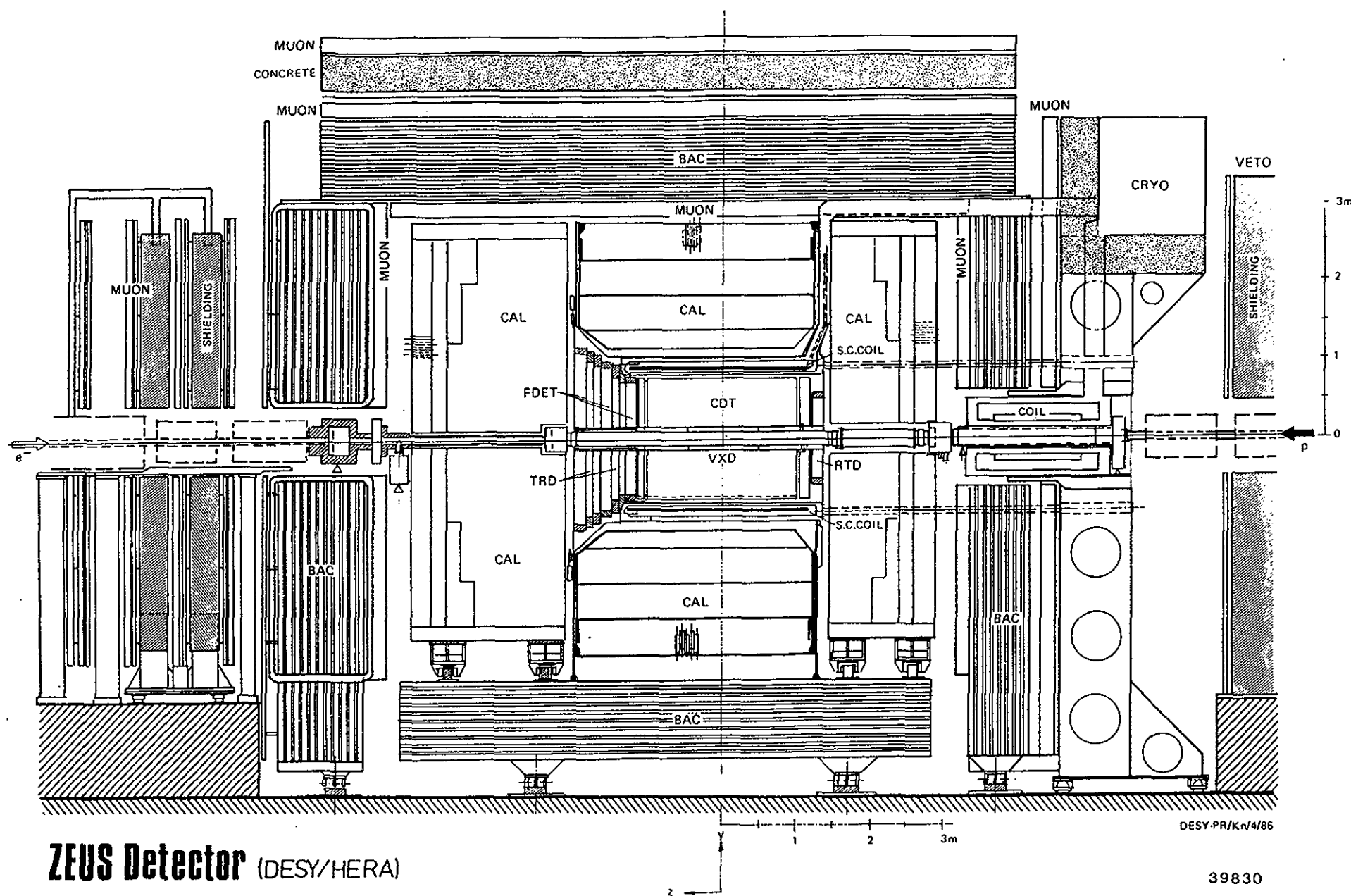**ZEUS Detector** (DESY/HERA)

Fig. 56 Section of the ZEUS detector along the beam.
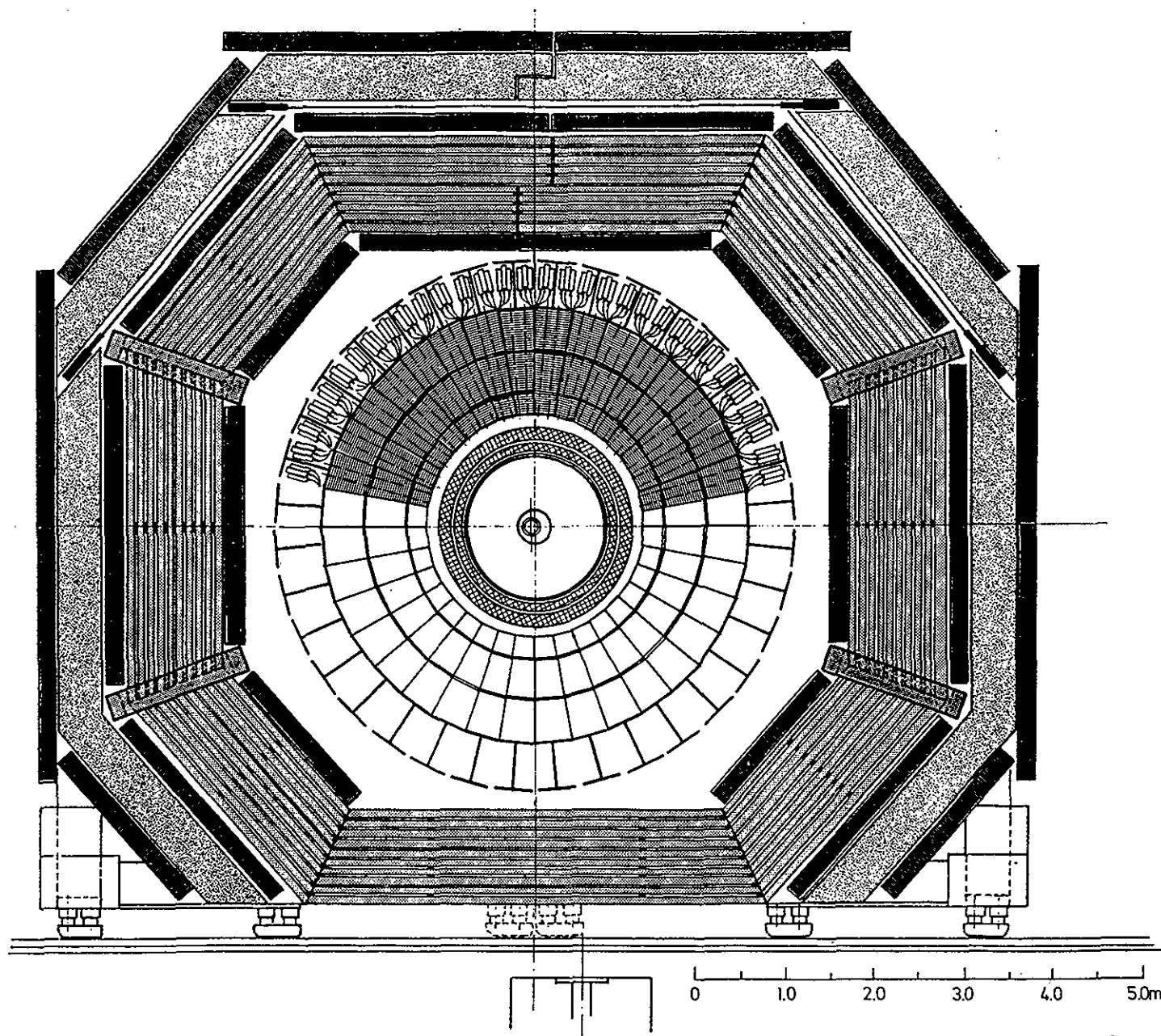
Fig. 57 Section of the ZEUS detector perpendicular to the beam.
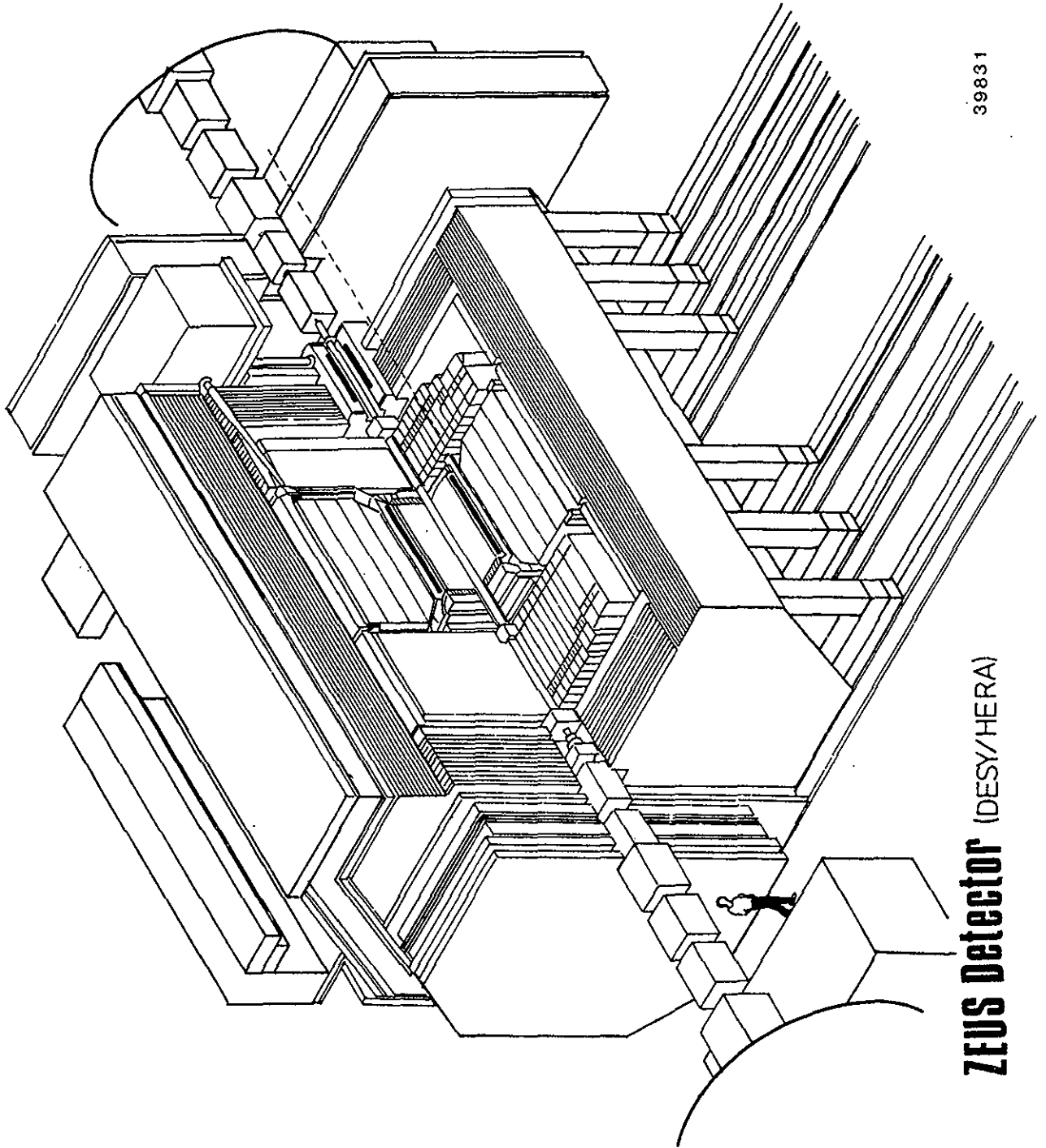
39829

39831

ZEUS Detector (DESY/HERA)

Fig. 58 Isometric view of the ZEUS detector.

pliers. The calorimeter is segmented longitudinally into an electro-
magnetic and one or two hadronic sections. Typical tower sizes are 5 cm
x 20 cm in the electromagnetic section and 20 cm x 20 cm in the hadronic
section. The calorimeter is divided into a forward, a barrel and a rear
part with 7, 5 and 4 absorption lengths, respectively. The active area
in the forward direction (proton beam direction) starts at about 60 mrad.
The solid angle coverage corresponds to 99.8 % in the forward hemisphere
and 98 % in the backward hemisphere. The expected energy resolutions are
for electrons $\sigma(E)/ = 0.15/\sqrt{E} \oplus 2$ % and for hadrons $\sigma(E)/E = 0.35/\sqrt{E} \oplus 2$ %.

In order to identify electrons within dense jets a silicon pad
detector is under study which could be inserted in the calorimeter at a
depth of 3-5 radiation lengths.

The high resolution calorimeter is surrounded by a backing calori-
meter of moderate energy resolution. Its purpose is to measure the energy
of late showering particles. The backing calorimeter uses as absorber the
iron plates which form the magnet yoke. Limited streamer tube chambers are
used for read out. The expected energy resolution for hadrons is
$\sigma(E)/E = 1.0/\sqrt{E}$.

The central track detector consists of a cylindrical jet type drift
chamber with an outer radius of 85 cm and an overall length of 240 cm.
Track position and dE/dx loss are measured in 9 superlayers each with
8 layers of sense wires. Four of the superlayers have stereo wires. A
resolution of 100 μm is expected, leading to a momentum resolution of
$\sigma(p)/p = 0.0018 \cdot p \oplus 0.0027$ (p in GeV/c) for a magnetic field of 1.8 T.
Particle tracking at small forward and backwards angles to the beam is
aided by four planar drift chambers providing a momentum measurement
with $\sigma(p)/p = 0.01 \cdot p$ at a foward angle of 120 mrad.

For the detection of the decays of short lived particles two pos-
sible designs for a vertex detector are under study.

Electron identification is performed with dE/dx information from
the tracking detectors and with the calorimeter. In the forward direction

a transition radiation detector, consisting of four modules, yields an additional hadron rejection factor of more than 100 for momenta below 30 GeV/c. The combined hadron rejection is well above 10^3.

Muons are detected in the forward direction in a spectrometer using drift and limited streamer tube chambers plus scintillator counters interspersed between the magnetized iron yoke and magnetized iron toroids. The momentum resolution for 100 GeV/c muons is $\sigma(p)/p$ = 30 %. In the barrel and rear detectors muons are detected by limited streamer tube chambers before, in between and behind the backing calorimeter and behind the concrete shield. The momentum resolution is 35 % at 20 GeV/c. The pion (kaon) rejection factors are 1000 (100) at 40 GeV/c in the forward direction, and 5000 (50) at 10 GeV/c in the barrel region.

A forward proton spectrometer detects very forward produced protons x_L > 0.3. The spectrometer uses proton beam line magnets and five miniature high resolution chambers installed in Roman pots very close to the beam at distances between 20 and 90 m from the interaction point. A momentum resolution of $\sigma(p)/p \sim 1$ % is expected.

Electron and photon detectors are installed some 30 to 100 m downstream in electron beam direction to measure the luminosity and tag small Q^2 processes.

The magnetic solenoid is superconducting and provides a field of 1.8 T. It has an inner radius of 86 cm, a length of 280 cm and is 0.8 radiation lengths thick. A compensating solenoid installed in the rear of the detector compensates the influence of the detector solenoid on the beam.

We shall take a closer look at some of the detector components.

8.2.1 The uranium calorimeter

The calorimeter consists of depleted uranium (DU) sheets interleaved with scintillator plates. Light generated in the scintillator is absorbed in the wave length shifter bar (WLS), reemitted at lower frequency and transported via light guide (LG) to the photomultiplier (PM) (Fig. 59).
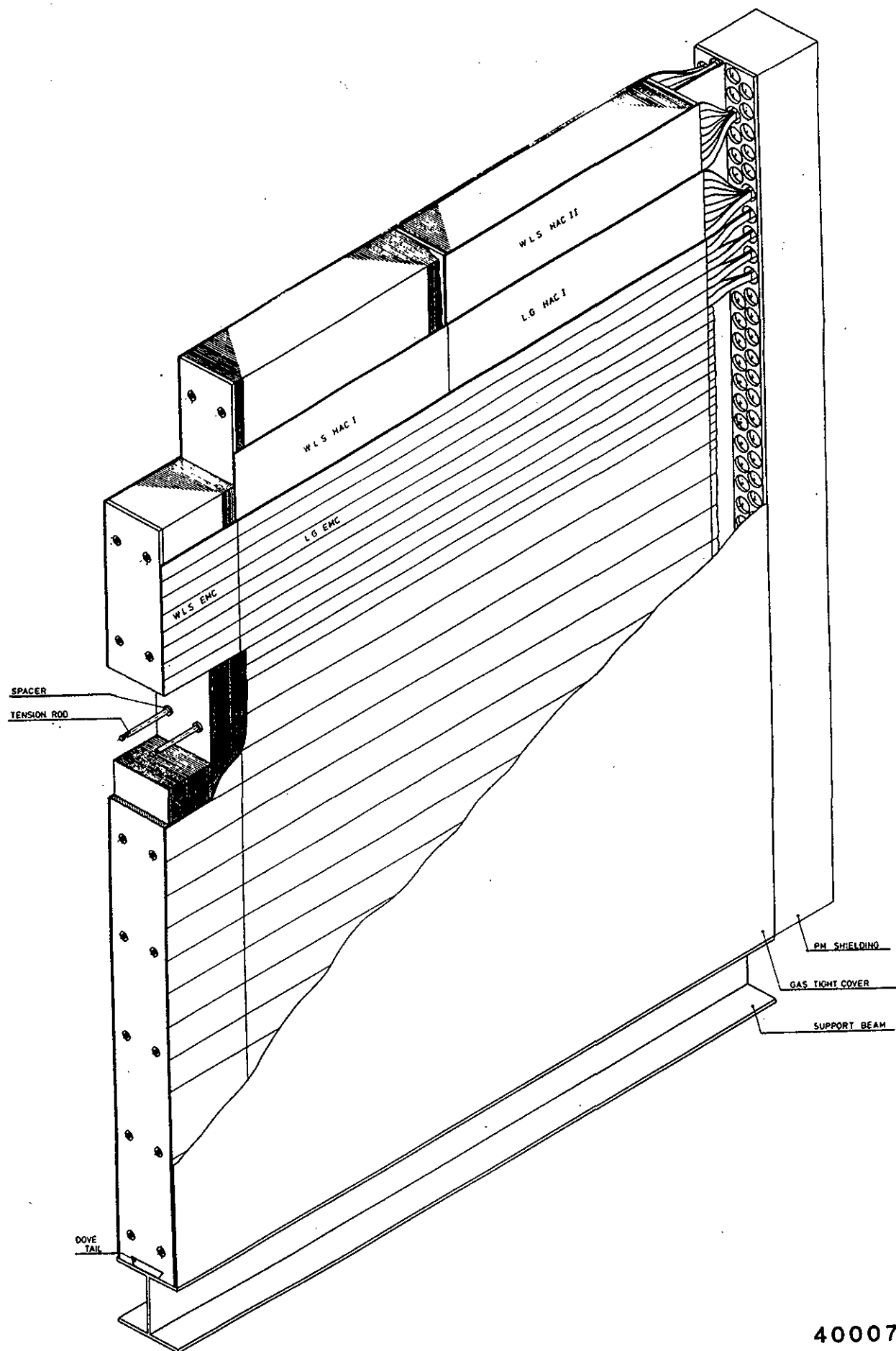
Fig. 59 View of an FCAL module; particles enter from the left.

40007

The calorimeter is subdivided into a forward (FCAL), a barrel (BCAL) and a rear part (RCAL) as indicated in Fig. 60. A cross sectional view of the FCAL along the beam is shown in Fig. 61a. The FCAL is made of 20 cm wide and up to 260 cm high modules. Figure 59 shows one of the FCAL modules. It is longitudinally separated into an electromagnetic (EMC) and two hadronic sections (HAC1, HAC2). The scintillator plates are cut to form towers of 5 x 20 cm^2 (EMC) and 20 x 20 cm^2 (HAC1, HAC2) which are readout on two sides by independent WLS bars.

The barrel calorimeter is subdivided into 36 identical modules, each subtending 10° in azimuth (Fig. 61b). The scintillator readout is arranged in towers which are typically 5 x 20 cm^2 (EMC) and 20 x 20 cm^2 (HAC) measured at the entrance face of the calorimeter.

Throughout the calorimeter the layer structure is kept the same, namely 3.2 mm DU sheets and about 3.0 mm scintillator plates in order to ensure full compensation and maintain optimum energy resolution for hadrons. Table 8 summarizes the number of layers and depths for the different calorimeter sections. The calorimeter has in total 7768 EMC and 5118 HAC readout channels.

The design of the calorimeter aims at keeping the constant term (c) in the energy resolution, $\sigma(E)/E = 35\ \%/\sqrt{E} \oplus c$, below c = 2 %. This puts a premium on uniform response. It can be achieved by taking special care in wrapping of the scintillator and inserting a filter between scintillator and WLS.

Table 8:   Properties of the DU calorimeter for ZEUS

calorimeter	Θ	section	n.of layers	depth (cm)	X_o	λ	tower size (cm^2)	n.of longt. segm.
FCAL	2.3^o - 39°	EMC	26	25.5	26	1.0	5x20	1
		HAC	154	141.6	162	6.0	20x20	2
BCAL	39° - 130°	EMC	25	23.8	25	1.1	5x20	1
		HAC	96	92.4	103	4.0	20x20	2
RCAL	130° - 172°	EMC	26	24.5	26	1.0	5x20	1
		HAC	77	70.8	81	3.0	20x20	1

39998

FCAL   BCAL   RCAL
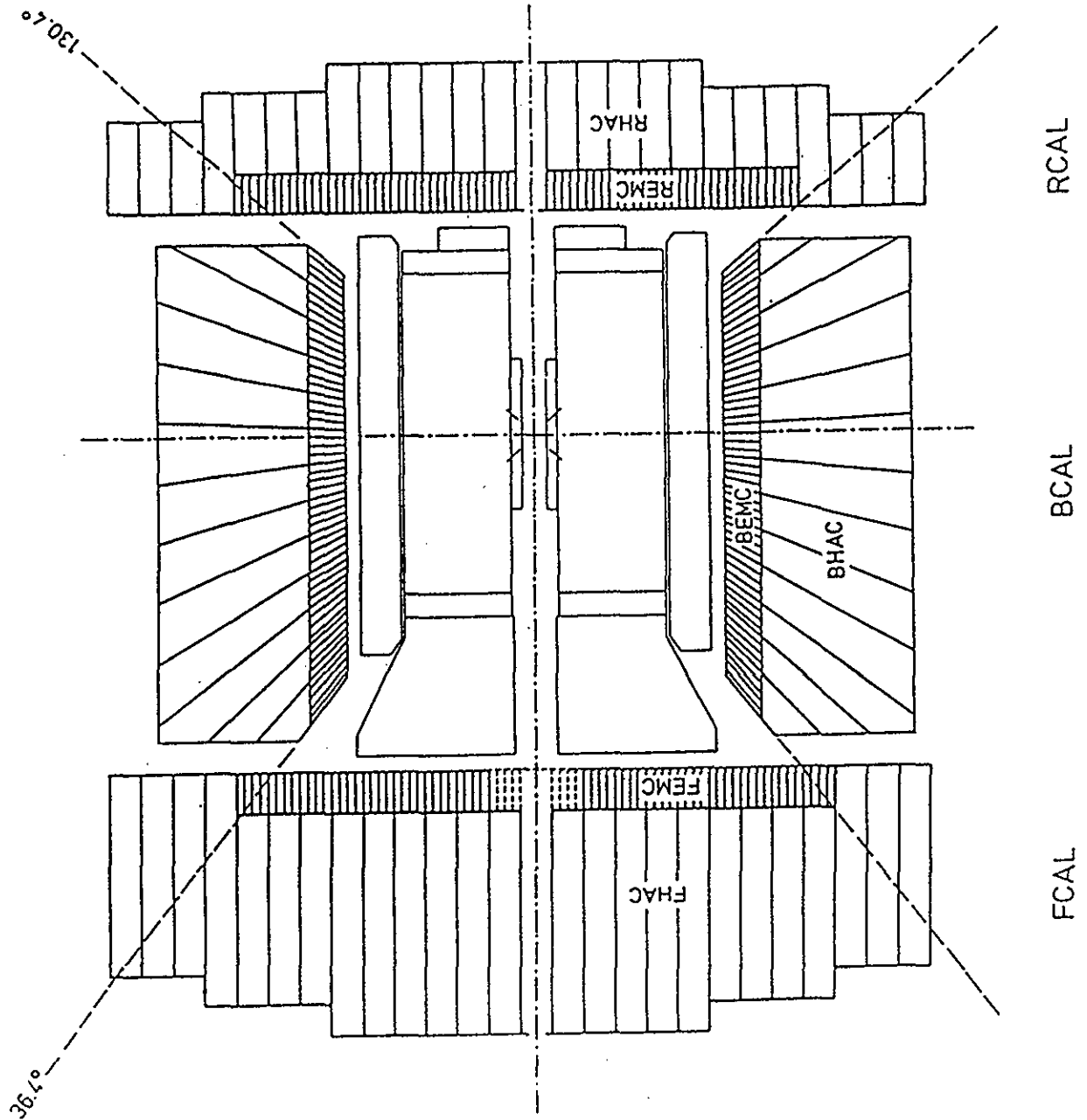
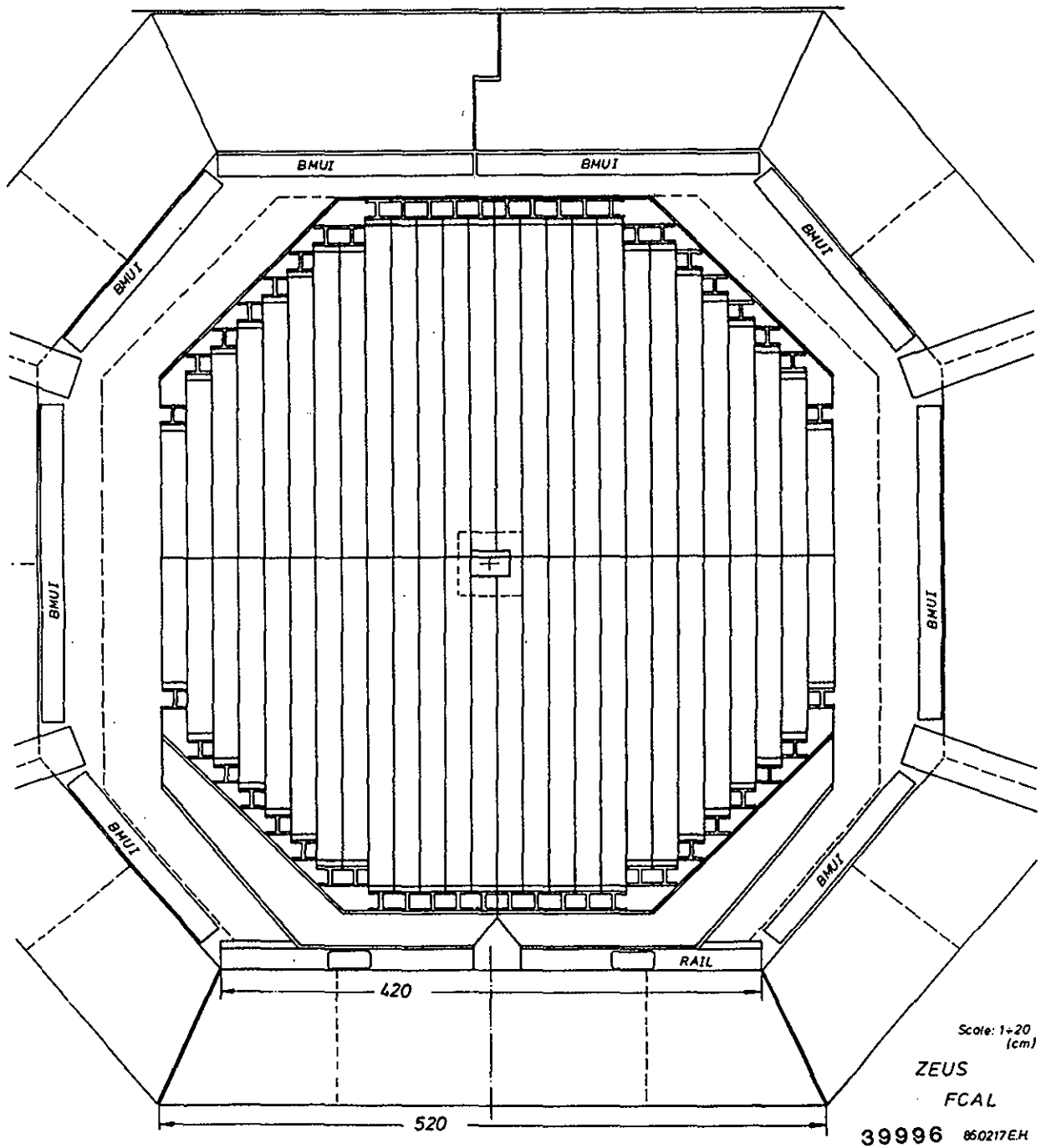Fig. 60 Layout of the DU-scintillator calorimeter of ZEUS.

Fig. 61a The ZEUS forward calorimeter FCAL as seen along the proton beam.
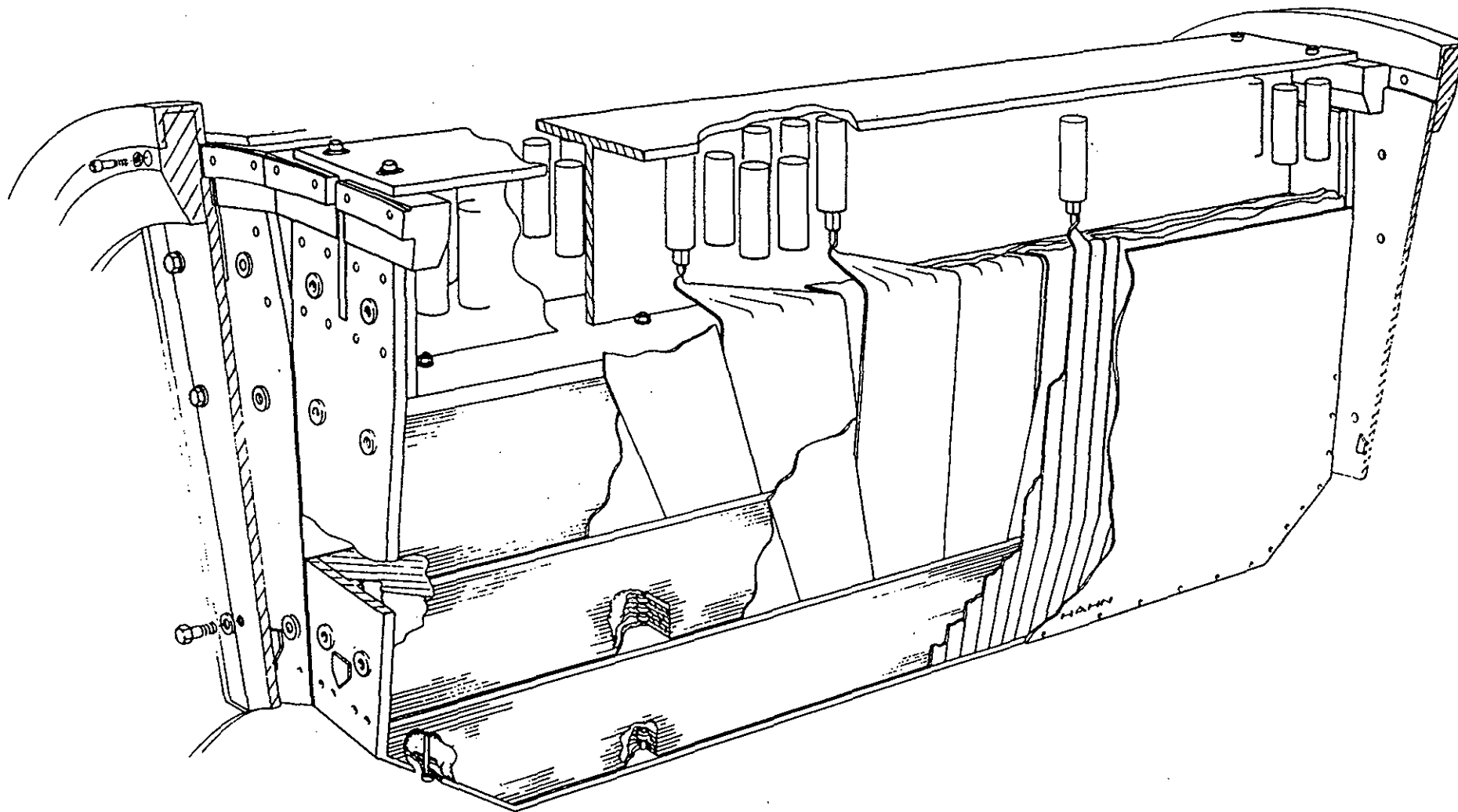
Fig. 61b Cut away isometric view of the ZEUS barrel calorimeter (BCAL).

The radiation level near the beam is rather high which is a potential problem for a scintillator readout. A first estimate based on experience at the $Sp\bar{p}S$ and Tevatron shows that most of the radiation is produced during injection of the beams and machine steering. For this reason FCAL and RCAL are divided vertically and each half will be retracted by 40 cm from the beam line during these beam operations. This is done without opening the iron yoke. With this measure the yearly dosage at the worst place is about $3 \cdot 10^4$ rad.

The dosage from the DU depends on the cladding of the DU plates. A yearly level of 10^2 rad is expected.

The radiation resistance of scintillator depends strongly on the base material. Most hadron calorimeters for collider experiments have employed acryllic based scintillator (AFS, UA1, UA2, CDF) whose performance deteriorates in a normal atmosphere above 10^5 rad. Aromatic scintillator such as NE110, SCSN38 to be used in ZEUS can sustain at least an order of magnitude more. Thus, the lifetime of the ZEUS calorimeter is expected to be well above 10 years.

For calibration the calorimeter modules have to be placed in a test beam. When installed in the detector calibration will be maintained using the radioactivity of the DU plates.

Test measurements have been performed with a DU calorimeter shown in Fig. 62a. Pulse height distributions for electrons and hadrons (mostly pions) are shown in Figs. 62b,c. An energy resolution of 33 - 34 $\%/\sqrt{E}$ has been obtained as shown in Table 9. The e/h ratio is between 1.09 and 1.06. It has to be corrected for nonuniform response of the WLS and for side and rear leakage estimated to be around 5 - 8 % for pions which will bring e/h close to unity.

Table 9: Performance of a preprototype calorimeter for ZEUS

	3 GeV	5 GeV	7 GeV
electrons, central tower	$\sigma/\sqrt{E}$ = 15.5 %	16.5 %	15.7 %
pions, all towers	$\sigma/\sqrt{E}$ = 33.3 %	34.1 %	33.0 %
e/h	1.09	1.07	1.06
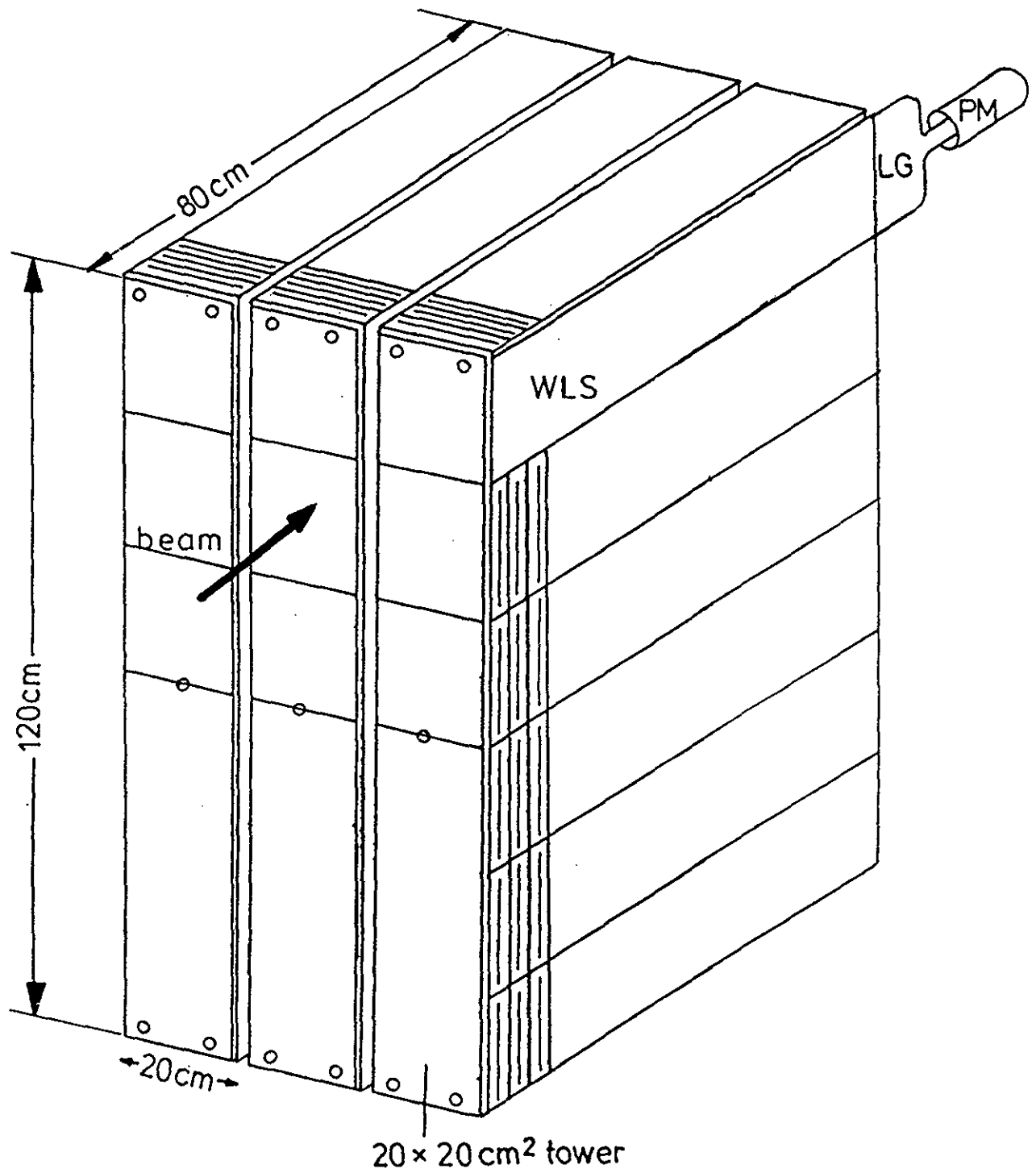
Fig. 62a   Setup of a DU-scintillator test calorimeter for ZEUS made of material from the AFS experiment at CERN.
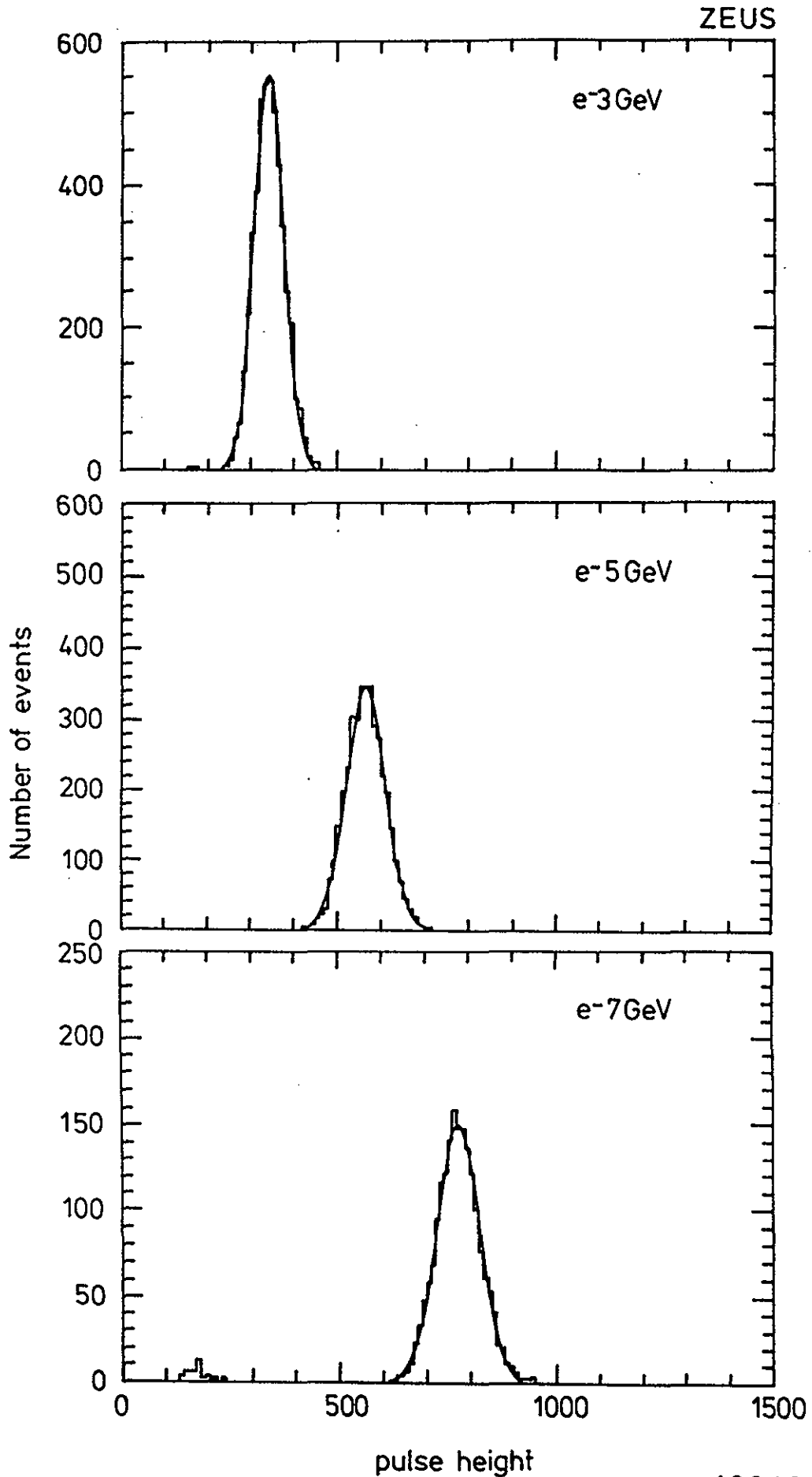
Fig. 62b Pulse height distributions measured with a DU - scintillator calorimeter (3 mm DU, 2.5 mm scint) for 3, 5 and 7 GeV electrons. (From ZEUS collaboration).

ZEUS

π⁻3GeV

π⁻5GeV

π⁻7GeV

Number of events

pulse height

40011

Fig. 62c Pulse height distributions measured with a DU - scintillator
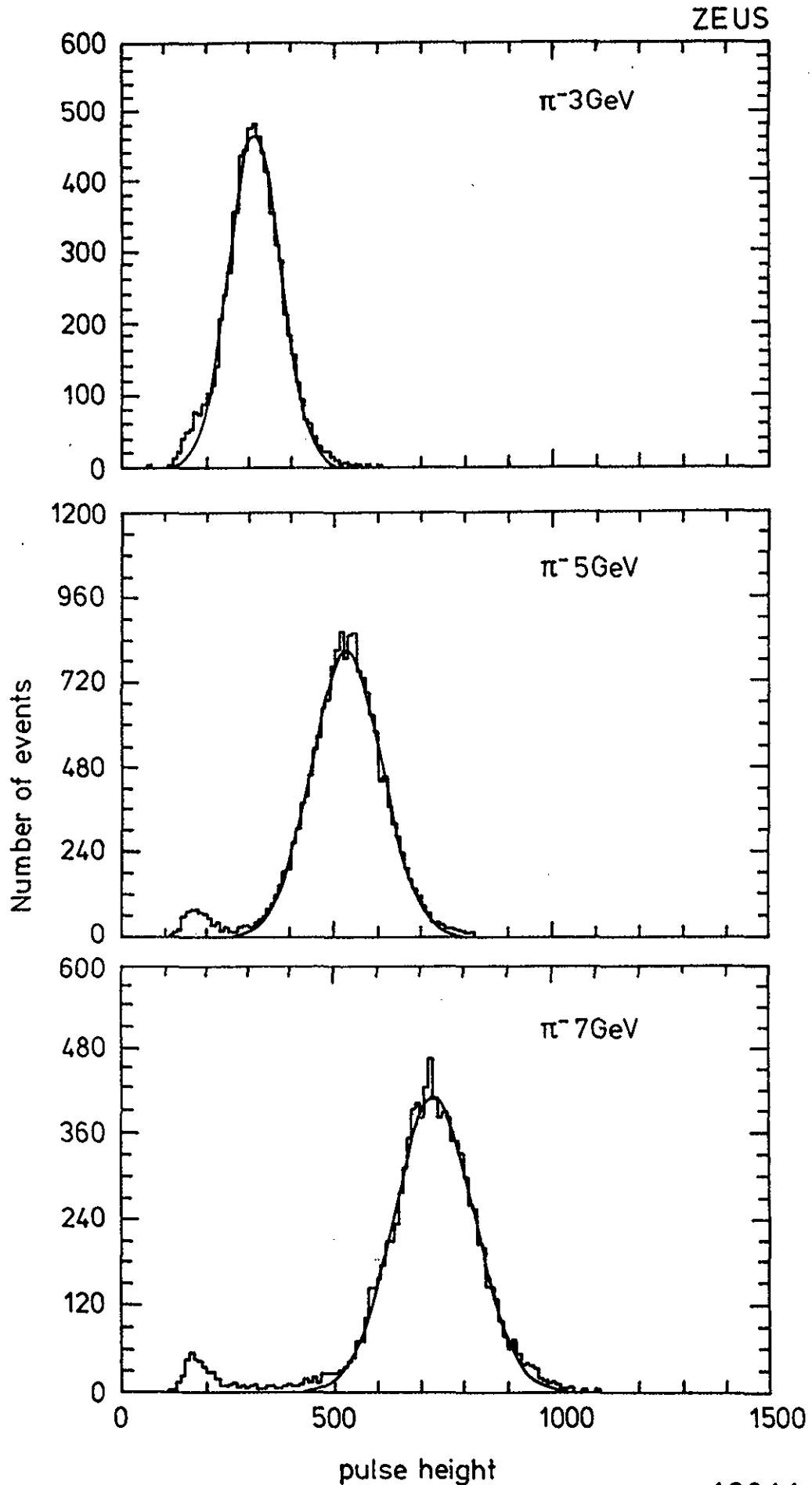calorimeter (3mm DU, 2.5 mm scint) for 3, 5 and 7 GeV pions.
(From ZEUS collaboration).

8.2.2 The tracking system

The arrangement of the inner tracking chambers is depicted in
Fig.63. In the central region charged particles are being tracked by a
drift chamber (CTD) which has an outer radius of 85 cm and a length of
240 cm. A sector of the CTD is shown in Fig. 64. There are 9 superlayers
each with 8 layers of sense wires. The drift cells are tilted to account
for the Lorentz angle. The maximum drift length is 3 mm corresponding to
500 ns drift time or 5 beam crossings. Five of the superlayers have wires
parallel to the beam axis; in four they are tilted by a small angle for
z measurement. The chamber has a total of 4608 sense and 19584 field wires.
The chamber is operated at atmospheric pressure yielding a precision of
< 100 µm.

The ZEUS collaboration is studying two alternative designs for a
vertex detector.The first is of the time expansion chamber type, the
second one uses a novel concept, the induction chamber (IC) (Ref. 44).
Figure 65 shows the wire configuration for one layer. Anode and field wires
are placed between two cathode planes. The distance between sense and field
wires is only 300 µm. From the anode signal alone a position accuracy of
600 µm/$\sqrt{12}$ = 176 µm is obtained. By comparing the signals produced in the
left and the right field wires a resolution of ~20 µm is expected.

The forward and backward regions are equipped with planar drift
chambers (see Fig. 63). Each chamber consists of three planes with
6 layers of signal wires each (Fig. 66a). For electron detection, in
between the drift chambers of the forward region four layers of tran-
sition radiation detectors (TRD) with polypropylen fibres as radiator and
drift chambers filled with X_e gas for TR detection are installed (Fig.66b).
A hadron rejection of > 100 is expected for momenta below 30 GeV/c.

8.2.3 Forward proton spectrometer

In most ep events the debris of the proton is emitted at very small
forward angles and escapes down the beam pipe. It is possible to gain
access to this region for a class of events which contains a leading proton.
In Lund simulation roughly 25 % of all NC and CC events are expected to
have a leading proton. Measuring the leading proton together with the
scattered electron and the current jet will give a class of fully contained
NC events. For CC scattering this will allow to measure the mass of the
undetected neutral particle (mostly the neutrino).

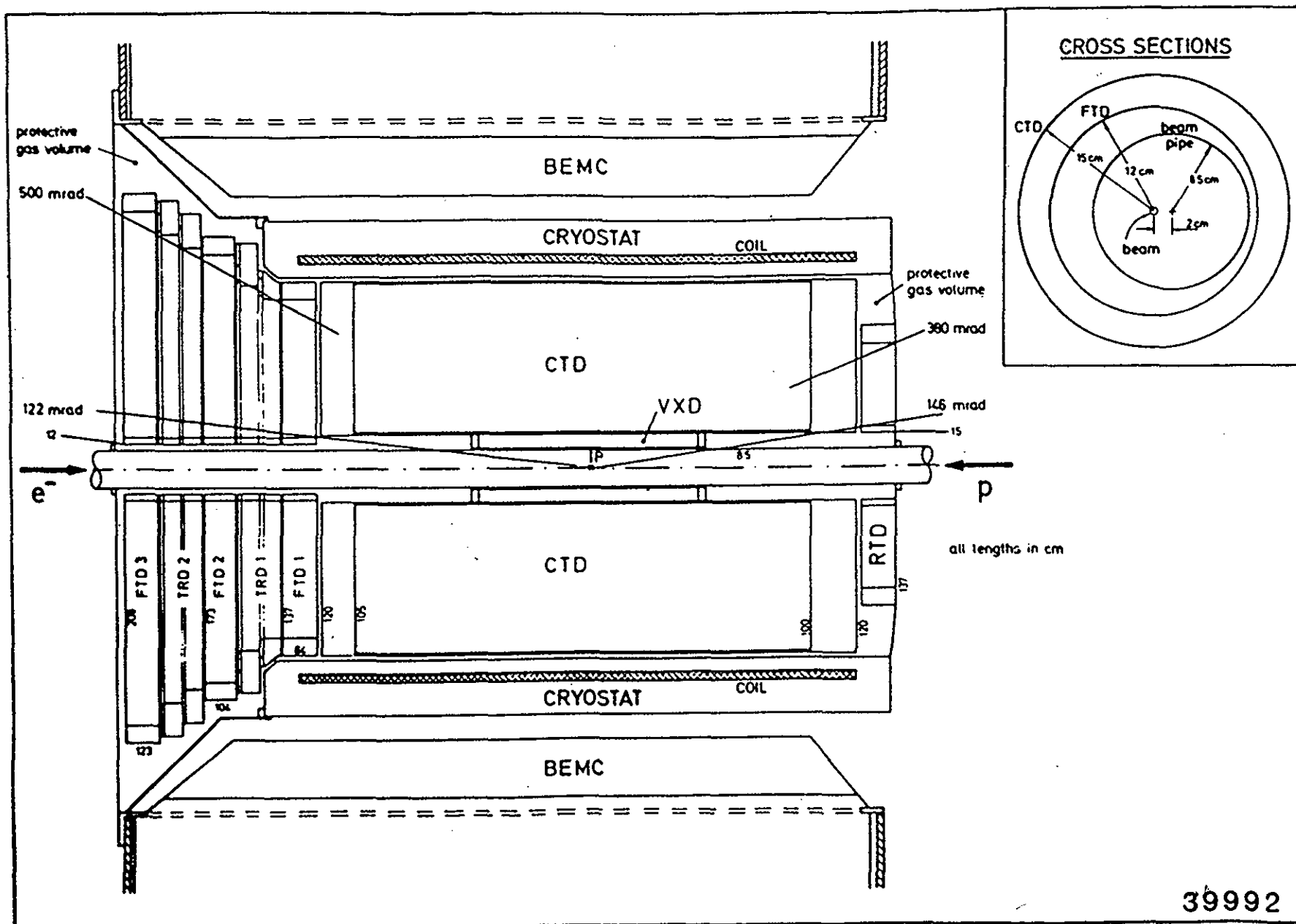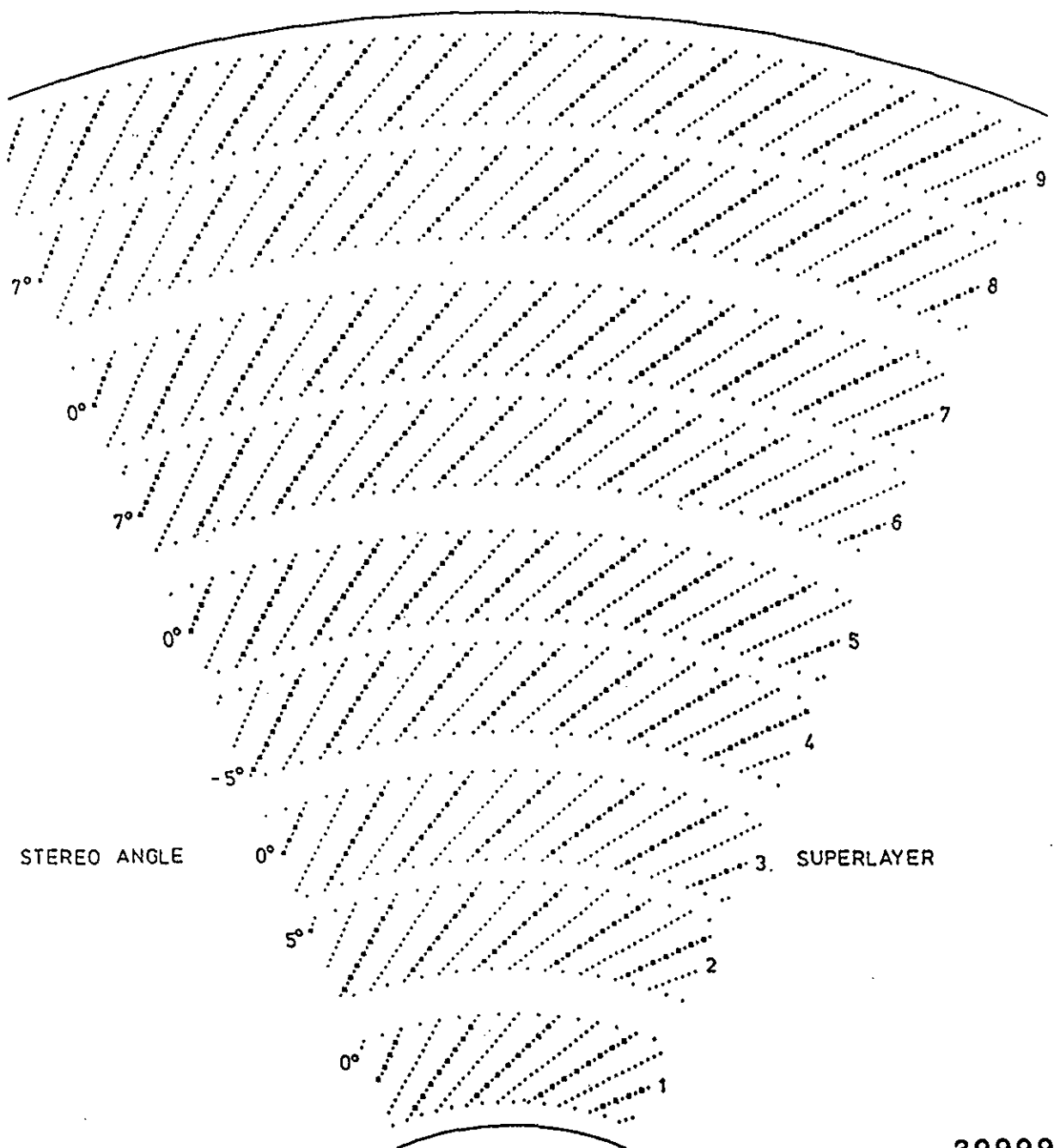Fig. 63 Layout of the inner tracking system for ZEUS.

Fig. 64 Cell arrangement in the ZEUS central tracking chamber.

39999
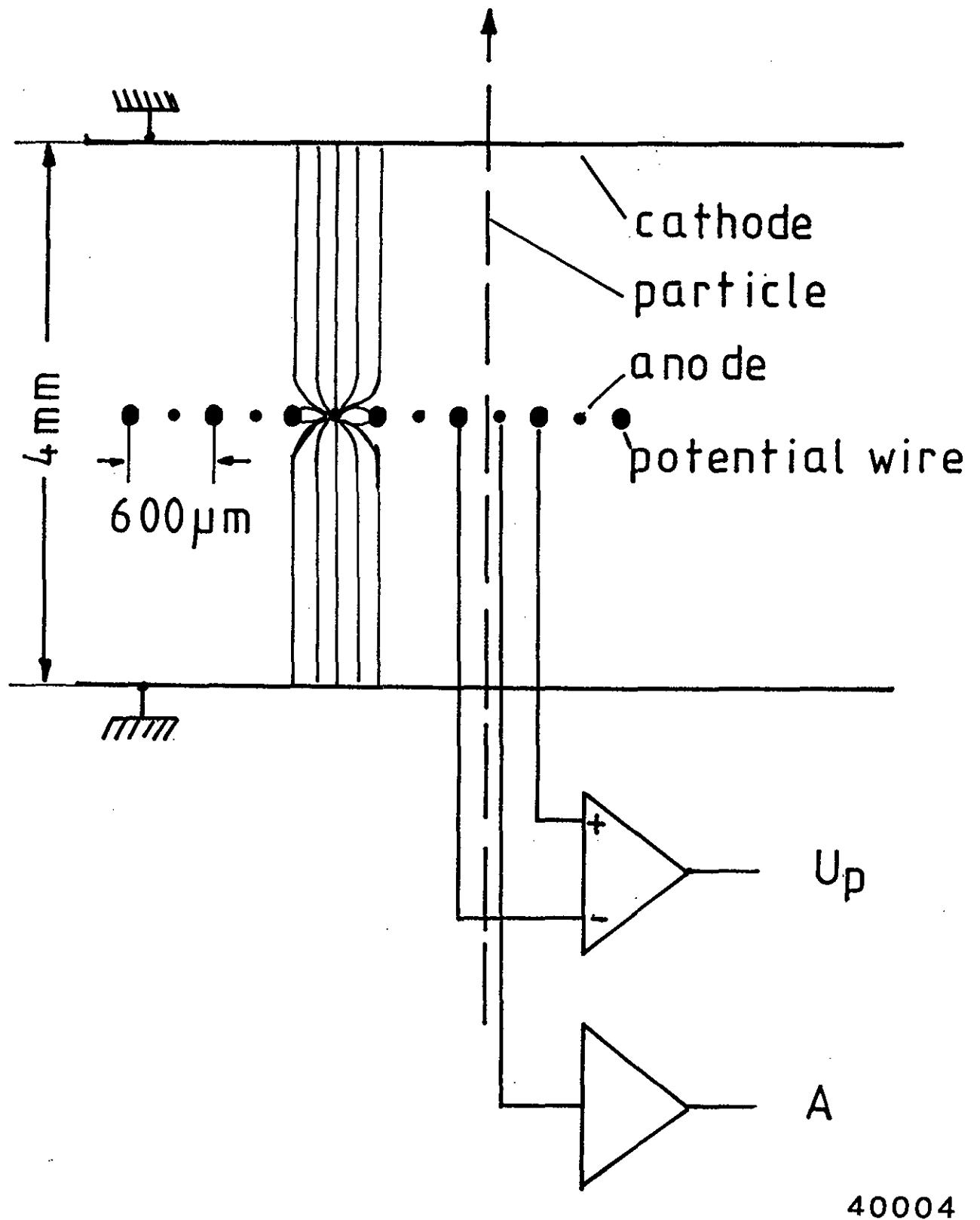
Fig. 65 Wire arrangement for the ZEUS vertex detector in the induction
chamber design.

40004

not to scale

3rd layer, wires - 60°

2nd layer, wires + 60°

1st layer, wires 0° w. r. t.
horiz. direction

39993
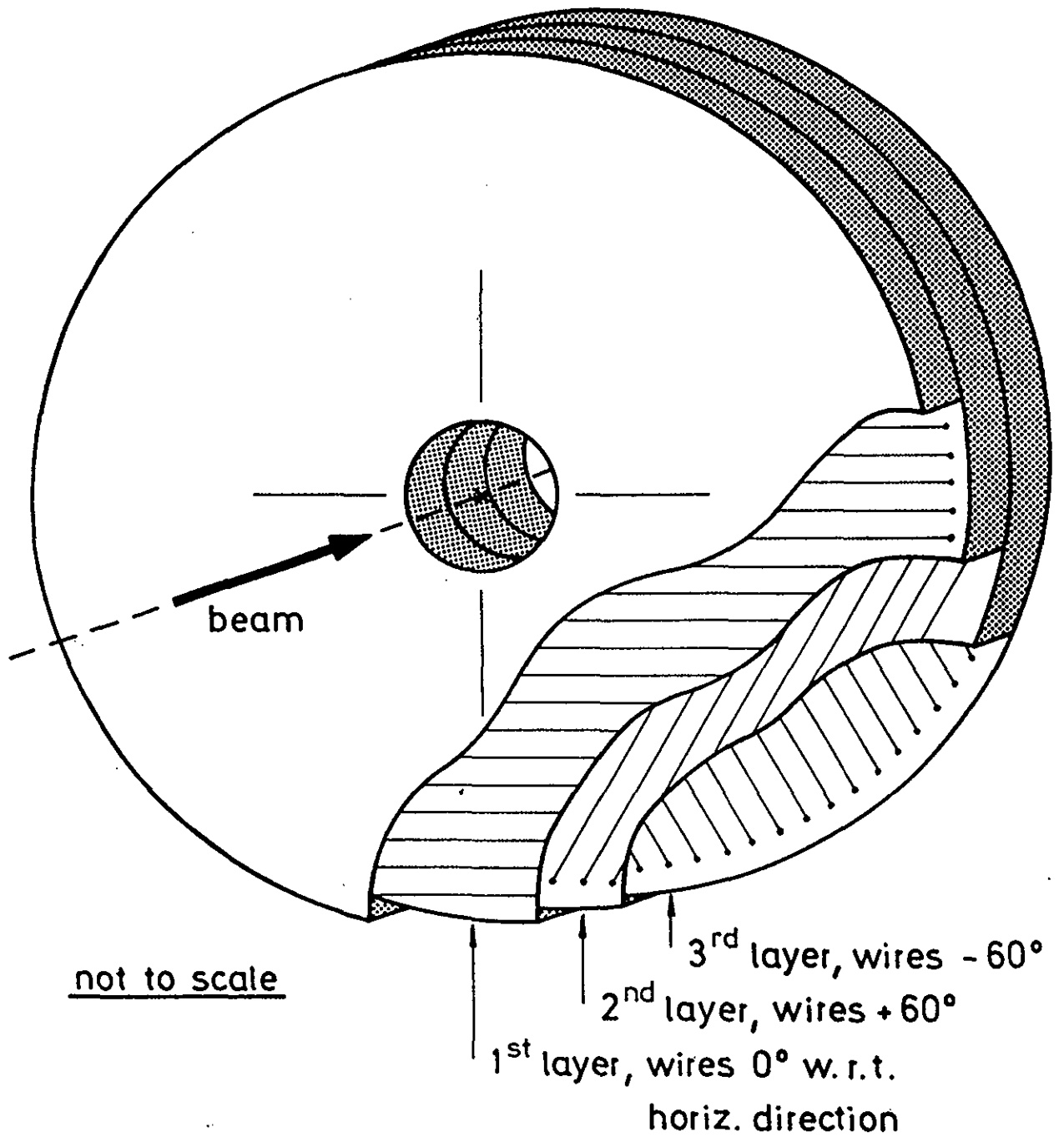
Fig. 66a Layout of a plane drift chamber for the ZEUS forward detector.

chamber frame

anode plane

cathode plane

aluminized foil
(to define the drift field)

space for electronics
and supplies

radiator
(foil stack)

scale 1: 100

100

space for
edge-connectors

PCB's

space for
amplifiers
and supply

wire combs

aluminized
Mylar-foils

anode-wire
plane
cathode
wire plane

drift region

amplification
region

radiator
PP-foil stack

C-fibre (Cu-coating)

- 106 -

Fig. 66b   The transition radiation detector for ZEUS. Longitudinal and transverse
view of a chamber module.

40008

40006

Fig. 67   Horizontal projection of the beam transport system and the detectors S1,S2,S3
of the ZEUS forward proton spectrometer.

Protons emitted in the forward direction can be detected downstream
of the interaction region using the proton ring magnets for momentum
measurement. Figure 67 indicates the position of detectors S1 - S3 installed
in Roman pots along the ring. The momentum resolution expected is ~1 %.

9. SUMMARY

HERA will give access to a new territory of physics. Structure functions and charged current reactions can be studied for Q^2 values up to 30 000 - 40 000 GeV^2. The Q^2-ν space will be extended by two orders of magnitude in either variable over what presently can be reached. Precise structure function values will provide a stringent test of QCD, will probe for substructure of quarks and leptons down to distances of $3 \cdot 10^{-18}$ cm, and could detect new neutral or charged pieces of the current. In the search for right handed weak currents longitudinally polarized electrons will be extremely useful.

HERA is potentially a rich source of new particles. Basically any state that has electric and/or weak charge can be produced up to masses of 200 - 250 GeV. The sensitivity in mass is shown in Table 10.

<p align="center">Table 10: Expected sensitivity in mass</p>

new W	800 GeV
new Z^0	800 GeV
right handed W	500 GeV
new quark (t like)	120 GeV
excited q*, e*	250 GeV
new quarks, leptons	220 GeV
leptoquarks	180 GeV
supersymmetric quark plus slepton	160 GeV

In many aspects HERA will be complementary to the e^+e^- colliders SLC and LEP which are also under contruction. It probes primarily the space like region and gives access to charged currents over a unique kinematic range. For a number of the newly proposed particles the mass range open to HERA experiments exceeds that of LEP II.

The design of an optimal detector for HERA poses a veritable challenge. The large momentum imbalance between incident electron and proton and the nature of space like processes throw most final state particles into a narrow cone around the proton direction. On the other

hand, the standard neutral curent reaction in HERA, ep → eX, offers an important advantage over p̄p/pp interactions. By tagging the scattered electron the kinematics of the relevant subsystem is determined. It is this handle which provides HERA experiments with a special sensitivity to new exotic particles.

ACKNOWLEDGEMENTS

References

1. Wiik, B.H., "Electron-Proton Colliding Beams, the Physics Programme and the machine, proc. 10th SLAC Summer Institute, ed.A.Mosher, 1982, p.233.

   Proc. 1984 ICFA Seminar on Future Perspectives in High Energy Physics, May 14-20, 1984, KEK, Japan, eds. S.Ozaki, S.Kurokawa, Y.Unno, p.23.

   Voss, G.-A., Status of the HERA Project, 12th Int.Conf.High Energy Acc., FNAL, 1983 and DESY-HERA Report 83-25 (1983).

2. Llewellyn-Smith, C.H. and Wiik, B.H., DESY Report 77/36 (1977).

3. Proc. Study of an ep facility for Europe, ed. U.Amaldi, DESY Report 79/48 (1979);

   HERA, proposal report DESY-HERA 81/10 (1981);

   Résumé Discussion Meeting "Physics with ep Colliders in view of HERA", Wuppertal, report DESY-HERA 81/18 (1981);

   Proc. Workshop "Experimentation at HERA", NIKHEF, Amsterdam, June 9-11, 1983, report DESY-HERA 83/20 (1983);

   Proc. Discussion Meeting on "HERA Experiments", Genova, Oct.1-3, 1984, report DESY-HERA 85/01 (1985);

   Altarelli, G., Mele, B. and Rückl, R., CERN Report TH3932 (1984);

   Bagger, J.A., Peskin, M.E., SLAC-PUB-3447 (1984);

   Cashmore, R.J. et al., "Exotic Phenomena in High Energy ep Collisions", Physics Reports (1985).

   Schmüser, P., "Tief Inelastische Lepton-Nukleon-Streuung", U.Hamburg, 1984, Lecture notes.

4. Bagger, J.A. and Peskin, M., Phys.Rev. D31, 2211 (1985);

   Altarelli, G., Mele, B. and Rückl, R., CERN Report TH3932 (1984);

   Proc. Large Hadron Collider in the LEP tunnel, Vol.2, 549 (1984);

   Rückl, R., Phys.Lett. 129B, 363 (1983); Nucl.Phys. B234, 91 (1984).

5. see Sciulli, F., Proc. 1985 Int.Symp.Lepton Photon Int. High Energies, ed. M.Konuma, K.Takahashi, p.8.

6. see e.g. Lohrmann, E., Mess, K.-H., DESY-HERA 83/08 (1983).

7. The ZEUS detector, Technical Proposal of the ZEUS Collaboration, March 1986.

8. Duke, D. and Owens, J.F., Phys.Rev. D30, 49 (1984)

9. Eichten, E.J., Lane, K.D., Peskin, M.E.,Phys.Rev.Lett. 50,811 (1983);

   Also see Rückl, R., Phys.Lett. 129B, 363 (1983).

10. MAC Collaboration, Fernandez, E. et al.,Phys.Rev.Lett. 50,123 (1983);

    TASSO Collaboration, Althoff, M. et al., Z.Phys. 22, 13 (1984);

Phys.Lett.138B, 441 (1984); MARK J Collaboration, Adeva, B. et al., Phys.Rep. 109, 131 (1984); HRS Collaboration, Bender, D. et al., ANL-HEP-PR-03; 71; PLUTO Collaboration, Berger, Ch. et al., Z.Phys. 27, 341 (1985).

11. Bars, I., Bowick, M.J., Freese, K., Phys.Lett. 138B, 159 (1984).

12. c.f. Pati, J.C., Salam, A., Phys.Rev. D10, 275 (1974); Mohapatra, R.N., Pati, J.C., ibid, 566, 2559 (1975); Mohapatra, R.N., Marshak, R.E., Phys.Rev.Lett. 44, 1316 (1980).

13. Mohapatra, R.N., Senjanovic, G., Phys.Rev.Lett. 44, 912 (1980).

14. Carr, J. et al., Phys.Rev.Lett. 51, 627, 1222(E) (1983).

15. Senjanovic, G., Proc. SSC Fixed Target Workshop, The Woodlands,Tx, (1984); Stoker, D.P. et al., LBL-18935 (1985) and Phys.Rev.Lett.

16. Beall, G., Bander, M. and Soni, A., Phys.Rev.Lett. 48, 848 (1982); Harari, H. and Leurer, M., Nucl.Phys. B233, 221 (1984); Ecker, G. and Grimus, W., Z.Phys. C30, 293 (1986).

17. Harari, H., private communication.

18. Leveille, J.P., Weiler, T., Nucl.Phys. B147, 147 (1979).

19. Brodsky, S.J., Gunion, J.F., SLAC-PUB-3527 (1984).

20. Altarelli, G., Martinelli, G., Mele, B., Rückl, R., CERN TH 4094 (1985).

21. Ellis, J., Gaillard, M.K., Nanopoulos, D.V., Nucl.Phys. B106, 292 (1976).

22. See e.g. Kühn, J.H., Tholl, H.D., Zerwas, P.M., CERN TH 4131 (1985).

23. Rudaz, S., Vermaseren, J.A.M., CERN TH 2961 (1981).

24. Jones, S.K., Llewellyn-Smith, C.H., Nucl.Phys. B217, 145 (1983).

25. Harrison, D.P., Nucl.Phys. B249, 704 (1985). Marlean, L., SLAC-PUB-3533 (1984).

26. For a recent review see e.g. Wiik, B.H., Progress with HERA, DESY-HERA 85-16 (1985).

27. Dwersteg, B. et al., DESY Report 85-08 (1985) and Proc. 1985 Part. Acc. Conf. Vancouver, IEEE Trans. Nucl. Sci. Vol. NS-32, 3596.

28. See e.g. Buon, J., Steffen, K., DESY report 85-128 (1985).

29. Piwinski, A., Proc. 1985 Part.Acc.Conf., Vancouver, 1985.

30. Ford, R.L. and Nelson, W.P., SLAC report <u>210</u> (1978).

31. Fabjan, C. and Willis, W., Phys.Rev.Lett. <u>60B</u>, 105 (1975);
    Fabjan, C. et al., Nucl.Inst.Meth. <u>141</u>, 61 (1977);
    Akesson, T. et al., Nucl.Inst.Meth. <u>A241</u>, 17 (1985).

32. See e.g. Gabriel, T.A. et al.,IEEE Trans.Nucl.Sci. <u>NS-32</u>, 697 (1985);
    Fesefeldt, H., The simulation of hadronic showers, <u>PITHA</u> 85-02 (1985).

33. Lankford, A.J., Thesis Geneva 1978, CERN Internal Report EP 78-3;
    Kondo, T. et al., 1984 Summer Study on the Design and Utilization of
    the Superconducting Super Collider, Snowmass, Colorado, June 1984;
    Brau, J., Proc. of Workshop on Compensated Calorimetry, Pasadena
    1985;
    Flauger, W., Nucl.Instr.Meth. <u>A241</u>, 72 (1985).

34. See e.g. Leroy, C., Sirois, Y. and Wigmans, R., CERN Report EP/86-66
    (1986), submitted to Nucl.Inst.Meth.

35. Brückmann, H. et al., private communication.

36. see e.g. Fabjan, C.W. and Ludlam, T., Ann.Rev.Nuc.Part.Sci. <u>32</u>,335
    (1982).

37. Wigmans, R., Proc. of Workshop on Compensated Calorimetry, Pasadena
    1985.

38. Abramowicz, H. et al., Nucl.Inst.Meth. <u>180</u>, 429 (1981).

39. WA-78 Collaboration, De Vincenzi, M. et al., CERN Report EP/86-12
    (1986), submitted to Nucl.Inst.Meth.

40. ZEUS: A Detector for HERA, Letter of Intent, June 1985.

41. Letter of Intent for an Experiment at HERA, H1 Collaboration, June
    28, 1985.

42. The ZEUS Detector, Technical Proposal, March 1986.
    Carleton, Manitoba, McGill, Toronto, York, Bonn, DESY, Freiburg,
    Hamburg I, Hamburg II, Siegen, Weizmann Institute, Bologna, Florence,
    Frascati, L'Aquila, Lecce, Milan, Padua, Rome, ENEA-Rome, Torin,
    NIKHEF Amsterdam, Cracow, Warsaw, Madrid, Bristol, London (IC),
    London (UC), Oxford, Rutherford, Argonne, Columbia, Illinois, Ohio,
    Pennsylvania State, Virginia, Wisconsin.

43. Technical Proposal for the H1 Detector, March 25, 1986,
    Aachen, Davis, DESY, Dortmund, Ecole Polytechnique, Glasgow, Hamburg,
    Houston, Lancaster, Liverpool, Manchester, Moscow, MPI München,
    Northeastern, Orsay, Paris, Rome, RAL, Saclay, Wuppertal, Zeuthen,
    Zürich.

44. Walenta, A., University of Siegen Report Si 86-5 (1986).